UNIVERSITÀ DEGLI STUDI DI PADOVA

UNIVERSITÀ DEGLI STUDI DI PADOVA

DIPARTIMENTO DI INGEGNERIA DELL'INFORMAZIONE

CORSO DI LAUREA MAGISTRALE IN
BIOINGEGNERIA

Integrative insights into brain function and metabolism: Investigating the resting-state [^{18}F]FDG-PET/fMRI coupling through partial least squares correlation analysis

Relatore:

Chiar.ma Prof.ssa Alessandra Bertoldo

Correlatore:

Ing. Giulia Vallini

Laureanda:

Claudia Tarricone

MATRICOLA 2060666

Anno Accademico 2023/2024

Abstract

The intricate interplay between brain function and metabolism has been a focal point in neuroscience, with a particular emphasis on the coupling of functional connectivity and metabolic processes. Brain function is characterized by a convolution of various biochemical and physiological processes, raising the interest whether resting-state functional connectivity derived from hemodynamic scales shows underlying metabolic synchronies. Increasing evidence suggests that metabolic connectivity based on glucose consumption associated with PET recordings may serve as a marker of cognitive functions and neuropathologies. However, to what extent fMRI-derived resting-state brain connectivity can also be characterized based on dynamic fluctuations of glucose metabolism and how metabolic connectivity is influenced by [^{18}F]FDG pharmacokinetics is still under debate.

Over the years, research has revealed significant associations between functional brain activity and metabolic processes, even if a limited spatial correspondence between functional and metabolic brain data (quantified as *SUVR*) at local level has been found, predominantly in the frontal regions. Thus, the spatial heterogeneity and interindividual variability in the functional-metabolic show there is an uncoupling between brain metabolism and rs-fMRI, arguing that [^{18}F]FDG PET adds significant information alone and beyond rs-fMRI. In fact, negative associations have been found between the temporal variability of FC and metabolism, showing a tendency for metabolic consumption to be higher if functional connectivity is stable over time.

Therefore, an investigation into the coupling between brain function and metabolism using a multivariate analysis approach into a connectivity framework, along with considering other parameters of metabolism at the local level, is missing in the literature. In this context, the present thesis project is proposed. Thus, the aim of this thesis is to assess the PLSC's ability to recognize covariation patterns between the two data modalities, functional obtained from rs-fMRI and metabolic from [^{18}F]FDG-PET scans, first in healthy subjects and then in patients with glioma.

For each subject, FC matrices were generated from resting-state fMRI signals filtered in two frequency bands (0.008-0.11 Hz, F_1; 0.008-0.21 Hz, F_2), while metabolic parameters (K_1, k_3, K_i, and *SUVR*) and MC matrices were obtained from PET scans.

PLSC was conducted to evaluate associations between functional and metabolic data, considering the combinations of K_1, k_3, K_i, and *SUVR* and FC strength (FC_{STR}) at local level and the overall FC-MC coupling at network-level analysis.

For each of the tested pairs, PLSC generated functional-metabolic salience maps and latent scores for each subject. Since PLS models are susceptible to overfitting, resulting in spurious associations that may not generalize well to new data, the generalizability of the multivariate correlation patterns was tested using a 7-fold cross-validation procedure, repeated for 100 iterations. The correlation between original and test latent scores was evaluated to assess generalizability, setting a threshold at 0.5.

The results demonstrated the PLSC's capability and robustness to capture covariation patterns between brain function and metabolism using both local and network-level approaches, revealing differences based on the frequency band in which the BOLD signal was filtered to obtain FC.

The first finding was the lack of a generalized coupling between FC strength and kinetic parameters k_3, and K_i, may be due to differences in these parameters, reflecting rapid biochemical processes, and FC measures, assessing neural activity correlations over longer periods. Moreover, they operate at different biological levels and may lack direct causal relationships, given the complexity of brain dynamics.

Overall, the results corroborate existing literature, showing limited spatial correspondence between functional and metabolic brain data at local level. This discrepancy was particularly notable for the *SUVR*-FC_{STR} pair, which showed a poor ability to describe the intricate relationships between brain function and metabolism. The nonlinear nature of the glucose uptake/consumption relationship in fMRI data, especially when described by measures derived from static functional connectivity such as the strength used in the present study, may be the main reason for the lack of agreement.

In the F_2 band, the coupling between K_1 and FC_{STR} was notably higher, likely due to both data modalities encapsulating hemodynamic components. This reveals a direct correlation between regional glucose influx rate and the strength of functional interactions, delineating two distinct groups: in the first group, high-order networks showing lower

strength values are characterized by higher K_1 values compared to the remaining areas, while in the second group, these networks have stronger functional importance with lower K_1 values. Thus, it can be concluded that regions within high-order networks showing lower FC strength but higher K_1 values are characterized by elevated metabolic activity. This suggests that despite their lower functional connectivity strength, these regions may play a more integrative role in coordinating neural activity or supporting cognitive processes.

Even more significant results were obtained from the network-level analysis between FC and MC matrices, which demonstrated consistent and robust behaviour in both frequency bands in which FC was obtained. This supports the notion that the link between brain function and metabolism operates at various temporal scales, capturing the contribution of the hemodynamic component. For this reason, deeper analysis of FC-MC coupling was conducted both at subject and group level. The first highlighted how, regardless of subject differences, the covariance pattern between FC and MC remains consistent, with more segregated FC in unimodal areas corresponding to globally more integrated MC, suggesting that stable FC consumes more energy.

Subsequently, group-level analysis focused on identifying significant saliences common to both FC and MC metabolic and further evaluating differences in significant salience patterns between brain hemispheres, highlighting concordant and discordant regions in topographic maps. This latter reported higher concordance in saliences in the left frontal and right occipital lobes, indicative of their involvement in fundamental cognitive and sensory functions requiring consistent neural activity and substantial metabolic energy. Conversely, greater discordance in saliences was found in posterior and subcortical regions, such as the left cerebellum and deep insular regions on the right, possibly due to their specialized functions and the need for frequent metabolic adjustments to support diverse connectivity patterns.

The research then shifted to include glioma patients for functional-metabolic pairs demonstrating strong generalizability. This part focused on identifying out-patients deviating from the healthy coupling range by projecting their functional and metabolic data onto a latent plane derived from healthy subjects. The study found that lower K_1 values associated with nearly “normal” FC strength in peri-tumoral areas could be potential biomarkers for frontal lobe tumour presence.

From the patient-level analysis of the FC-MC pair, it was interesting to note a modest but significant reversal of the positive linear trend observed in HCs, indicating that the presence of a glioma, particularly in the frontal lobe, leads to a decrease in FC values compared to the average values of HCs, which is associated with an increase in MC values. Lastly, it was intriguing to observe how the decoupling between FC and MC was even more precise in localizing a tumour in the frontal lobe compared to the K_1-FC_{STR} pair, further supporting the hypothesis that the strongest relationship between functional connectivity and metabolism, in terms of positive concordance, occurs in the frontal regions of the brain.

In summary, this thesis highlights the significance of adopting a multimodal approach to comprehend the intricate relationship between brain function and metabolism. It showcases the efficacy of PLSC in capturing covariation patterns between these modalities and underscores the importance of personalized analysis considering individual differences.

Contents

List of Figures

List of Tables

Chapter 1

Introduction

1.1 Neuroscientific fundamentals of brain function

The neuroscientific exploration of brain function delves into the intricate workings of the central nervous system, unravelling the complexities that underlie human intelligence, perception, and behaviour. This comprehensive examination involves an in-depth understanding of the fundamental units of the nervous system, the neurons, along with the mechanisms governing their communication. From the structural intricacies of neurons to the dynamic processes of synaptic transmission, the neuroscientific fundamentals of brain function provide a framework for grasping the remarkable capabilities of the human brain. This exploration encompasses the integration of signals, the classification of brain cells based on their functions, and the critical role played by various brain regions [1].

1.1.1 Function and metabolism of brain cells: neuroglial metabolic coupling

The human brain is a complex system of different interconnected cell types, each contributing uniquely to its structure and function. Among these cells are neurons, oligodendrocytes, astrocytes, ependymal cells, peripheral glia (including Schwann cells, satellite glia, and enteric glia), immune cells, and vascular cells [2].

Neurons, the fundamental units of function, exhibit a complex architecture finely tuned for their critical roles and are supported by glial cells, which also play a key role in signal transmission. Neurons consist of a cell body (soma), dendrites, an axon, and axon terminals. Dendrites receive signals from neighbouring neurons, while the axon transmits these signals away from the cell body to other neurons or target cells, with which the axon terminal allows communication, forming the basis for intercellular signalling. Grey matter, comprising neuron bodies, dendrites, and pyramidal cells, forms the outer layer (cerebral cortex) of the brain, while white matter, consisting primarily of myelinated axons and various glial cells, lies beneath and facilitates communication between brain

regions [3], [4]. This cellular diversity is observed across species and within distinct brain regions. For instance, the cerebellum, despite occupying a small volume, contains a high density of neurons compared to other brain regions. Brain's heterogeneity goes beyond cellular composition and includes patterns of wiring, connectivity, and intrinsic properties. Cortical networks, for instance, consist predominantly of glutamatergic excitatory projection neurons and local GABAergic inhibitory interneurons, each exhibiting a rich diversity of morphological and functional characteristics [2].

The functionality of neurons is critical to the overall operation of the nervous system. Neurons transmit information through rapid and precisely regulated electrochemical impulses, the action potentials, that enable the propagation of signals across vast neural networks. Moreover, neurons play a vital role in the integration of signals, combining inputs from multiple sources. This integration is crucial for the processing of information and forms the basis for complex cognitive functions, behaviour, and overall brain activity [1].

Astrocytes, long regarded as mere supportive cells in the central nervous system, are now recognized as active participants in regulating neural activity and energy metabolism [1], [5], [6], [7], [8]. These star-shaped glial cells, that outnumber neurons by approximately five times in vertebrates, play multifaceted roles in maintaining the metabolic homeostasis of the brain by tightly coupling their metabolic activities with those of neighbouring neurons [9].

Despite comprising only two percent of body mass, the brain is the most dynamic centre of activity that consumes a significant portion of the body's glucose and oxygen [5]. Recent studies have highlighted the heterogeneity of glial cells, particularly astrocytes, which, like neurons, display diverse metabolic profiles. A fundamental distinction between neurons and glial cells lies in their metabolic preferences. Neurons primarily rely on mitochondrial oxidative phosphorylation (OXPHOS) to meet their energy demands, while astrocytes predominantly utilize glycolysis. This metabolic dichotomy reflects the unique roles of each cell type in supporting neuronal function and overall brain homeostasis. Astrocytes emerge as key regulators of brain metabolism, orchestrating energy production, redox balance, and substrate availability in response to neuronal activity. They collaborate with neurons to modulate neurotransmitter-receptor interactions and maintain cellular integrity.

1.1.2 Mechanisms of synaptic transmission

At the junction between two neurons is a crucial connection known as a synapse. When an electrical impulse travels along the axon of the presynaptic neuron, it reaches the end and triggers the release of neurotransmitters into the synaptic cleft; then these molecules bind to receptors on the postsynaptic membrane, initiating a cascade of events that generate a new electrical signal in the receiving neuron. This process requires energy at multiple stages: the production and packaging of neurotransmitter molecules within the presynaptic neuron; the release of neurotransmitters; the propagation of action potentials and the modulation of membrane potentials by locally spreading postsynaptic potentials; the neurotransmitter molecule's reuptake and recycling by transport proteins and enzymatic degradation [1], [4].

Given the energy-intensive nature of synaptic transmission, there is a close metabolic coupling between neuronal activity and energy production. Since the primary energy currency of cells is the ATP (adenosine triphosphate) and oxygen and glucose are crucial substrates for ATP production via oxidative phosphorylation, regions of heightened neural activity require both changes in metabolic activity and oxygen supply, resulting in enhanced blood flow in the surrounding vessels. Such physiological response alters the levels of oxyhaemoglobin and deoxyhaemoglobin in the bloodstream. The intricate coordination between cerebral blood flow and neuronal activity, termed *neurovascular coupling* (NC) or *functional hyperaemia*, involves a sophisticated interplay of regulatory mechanisms engaging neurons, glial cells, particularly astrocytes during glutamatergic neurotransmission, and vascular components. In fact, astrocytes synthesize neurotransmitter precursors, such as glutamine and lactate, providing neurons with essential building blocks for neurotransmitter synthesis. Moreover, astrocytes serve as reservoirs of glycogen, which can be mobilized to supply lactate to neurons during periods of increased metabolic demand. Thus, the metabolic dialogue between astrocytes and neurons involves the uptake of neurotransmitters from the synaptic cleft, such as glutamate, by astrocytes, triggering glucose uptake and glycolytic activation. Astrocytes then release lactate, which serves as an energy substrate for neurons, complementing their reliance on oxidative metabolism. This astrocyte-neuron lactate shuttle facilitates energy transfer between the two cell types, supporting neuronal survival, synaptic function, and overall brain activity.

The extent of astrocytic involvement in neurovascular coupling varies across different segments of the cerebrovascular tree. While astrocytes exert a significant influence on capillary function, regulating blood flow, modulating vessel diameter, and influencing vascular tone, their role in arterioles appears to be comparatively less pronounced. This close interaction between astrocytes and capillaries ensures precise spatial and temporal coordination between neuronal activity and blood perfusion, enabling efficient neuronal transmission and communication and optimizing brain function [5], [7], [8].

Overall, this complex metabolic interplay between astrocytes and neurons underscores the collaborative nature of brain metabolism and its critical role in sustaining neuronal function, synaptic plasticity, and cognitive processes.

1.2 Neuroimaging methods: fMRI and [^{18}F]FDG-PET

Among all neuroscience imaging techniques, functional Magnetic Resonance Imaging (fMRI) and Positron Emission Tomography with [^{18}F] fluorodeoxyglucose ([^{18}F]FDG-PET), provide valuable information about neurovascular and metabolic processes in the brain, respectively. Indeed, fMRI detects changes in blood oxygen levels to infer neuronal activity, exploiting neurovascular coupling, in which increased neuronal activity triggers local changes in cerebral blood flow. In contrast, [^{18}F]FDG-PET provides a snapshot of glucose metabolism, reflecting the metabolic demands of active brain regions. When used together, these modalities provide complementary information, allowing for a more comprehensive assessment of the neurovascular-metabolic coupling. By simultaneously capturing changes in cerebral blood flow and glucose metabolism, fMRI and [^{18}F]FDG-PET could provide a nuanced understanding of how neural activity is energetically sustained and regulated [10], [11]. This integrated approach promises to elucidate the complex interplay between neuronal function, vascular responses, and metabolic demands in the brain, potentially advancing understanding of neurological disorders and diagnostic capabilities.

1.2.1 Principles of resting-state fMRI: acquisition and analysis

The fMRI has its roots in the development of Magnetic Resonance Imaging (MRI) technology, which emerged in the 1970s. MRI revolutionized medical diagnostics by providing detailed images of soft tissues with exceptional spatial resolution. However, it was not until the late 1980s and early 1990s that scientists realized the potential of MRI

for functional brain imaging. The discovery that changes in blood oxygenation levels were coupled with neural activity led to the development of non-invasive fMRI techniques for mapping brain function.

BOLD signal and the hemodynamic response

Haemoglobin, in fact, possesses different magnetic properties depending on whether it is bound to oxygen or not: oxygenated haemoglobin (Hb) exhibits diamagnetic characteristics, that is, it possesses no stray electrons and has zero magnetic moment, while deoxygenated haemoglobin (dHb) is paramagnetic and possesses, therefore, stray electrons and a non-zero magnetic moment. Fully deoxygenated blood is characterized by 20% greater magnetic susceptibility than that of fully oxygenated blood. The fMRI exploits this magnetic property of haemoglobin, which is, therefore, used as an endogenous contrast agent: the introduction of a material with magnetic susceptibility within a magnetic field causes the nuclear spins to phase shift, resulting in a decay of the transverse magnetization, which is related to the time constant T2*.

Deoxygenation of blood, by changing the magnetic susceptibility, causes the measured T2*-weighted MR signal to vary, increasing as deoxygenation decreases. The magnitude of this effect increases with the square root of the static magnetic field strength. In fact, the relative decrease in deoxyhaemoglobin concentration in regions where there is neuronal activity causes an increase in the T2* parameter, which in turn leads to increase in T2*-weighted image intensity (Figure 1.1).

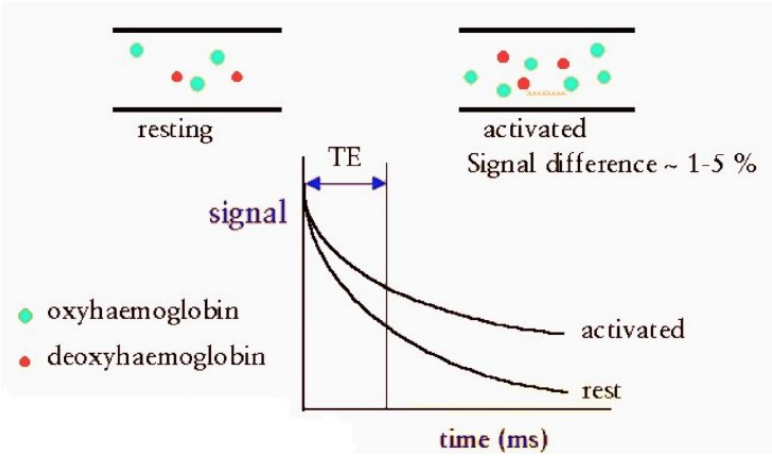

Figure 1.1: The *effect, on the MR signal pre-sampled in T2*, of the local decrease in deoxygenated haemoglobin in the activated areas compared to those in the resting state. This change in dHb concentration results in an increase in the signal measured in regions characterized by activity* [12].

In 1990, Ogawa et al. demonstrated, through experimental evidence in animals, that magnetic fields over 1.5T and T2*-weighted MR signal could measure the Blood Oxygenation Level Dependent (BOLD) signal, dependent on deoxygenated haemoglobin levels in various brain regions.

The underlying mechanism was then explained by the *balloon model* proposed by Buxton, Wong, Frank in 1998, which described changes in blood volume related to neural activity, leveraging the paramagnetic nature of deoxygenated haemoglobin.

In recent years, researchers have made significant strides in understanding the mechanisms underlying the neurovascular connection. The current model posits that various factors, including the generation of action potentials, synaptic activity, release of neuromodulators and neurotransmitters, and astrocyte activity, contribute to increasing cerebral blood volume (CBV) and flow (CBF). Additionally, these processes lead to heightened metabolic rates (Regional O_2 Consumption Rate, $CMRO_2$) within the involved nervous tissue [13], [14]. The Figure 1.2 summarize the entire neurovascular coupling model.

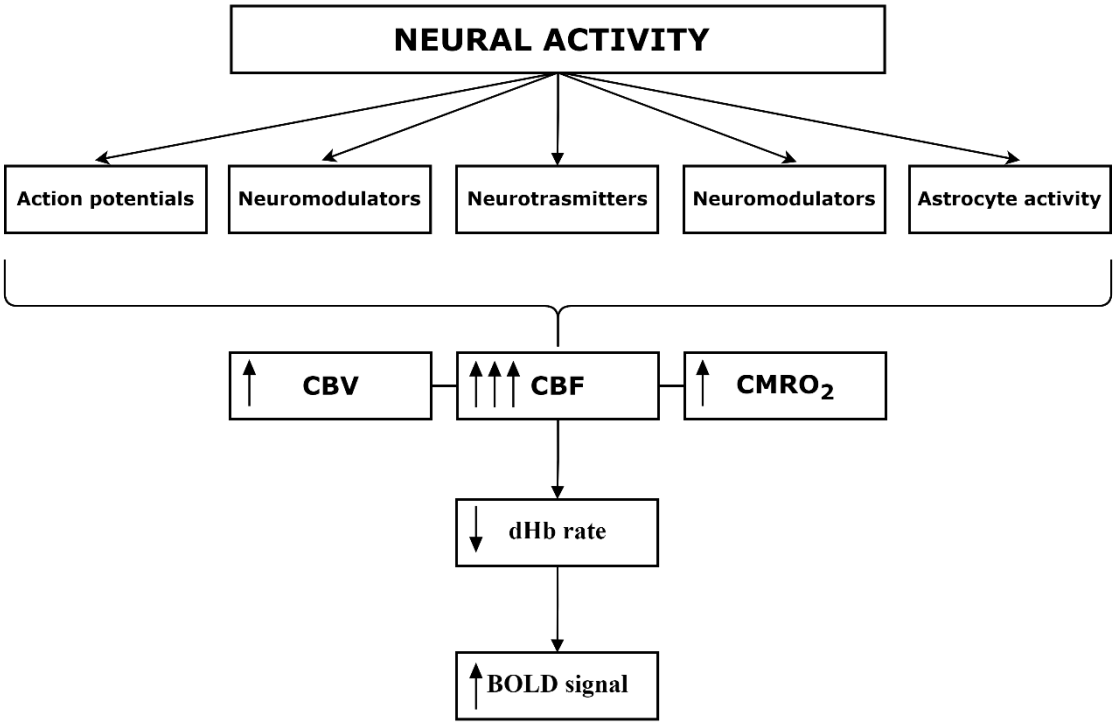

Figure 1.2: *Changes in the BOLD signal are linked to neural activities. When a specific brain region engages in certain tasks or processes information, it sets off a cascade of electrical, chemical, and cellular events. These events regulate blood flow and metabolic activity in the cortical regions, altering the ratio of oxyhaemoglobin to deoxyhaemoglobin and influencing the BOLD signal detected in fMRI scans (adapted from* [15]*).*

Initially, as a consequence of neural activity, there is a surge in blood flow that results in more blood entering the venous system than leaving, causing an increase in blood volume. In small veins, the initial volume increase is characterized by the presence of deoxygenated haemoglobin, which is cleared first from the capillaries, resulting in a temporary loss of MR signal, termed the *initial dip (*Figure 1.3). Following this initial dip, metabolic demands due to neuronal activity increase above baseline levels, leading to an increase in incoming oxygenated blood flow. If the amount of oxygenated blood transported to the area exceeds its extraction, there is a decrease in deoxygenated haemoglobin within the voxel. Consequently, the BOLD signal increases above baseline approximately 2 seconds after the onset of neural activity, reaching a peak value around 5 seconds for short-duration stimuli. If neural activity persists over time, then the peak value is maintained, resulting in what is called a *plateau* (Figure 1.3).

However, after the peak, there is an effect called *post-stimulus undershoot*, where the MR signal drops below baseline levels. This is attributed to an imbalance in the rates at which blood flow and blood volume return to their baseline levels after neural activity ceases and the actual metabolic requirements of the neurons. While CBF decreases rapidly, CBV takes longer to return to baseline, resulting in a relative increase in deoxygenated haemoglobin concentration, thus reducing the overall fMRI signal (Figure 1.4). As blood volume returns to normal levels, the signal reaches baseline value [16].

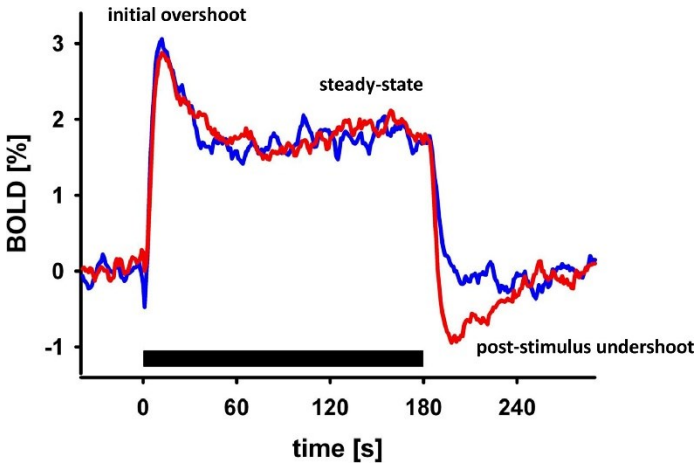

Figure 1.3: *Average BOLD time courses from early visual cortex; after an initial overshoot, a new steady-state level is reached, followed by a post-stimulus undershoot that varies in amplitude depending on the stimulus* [17].

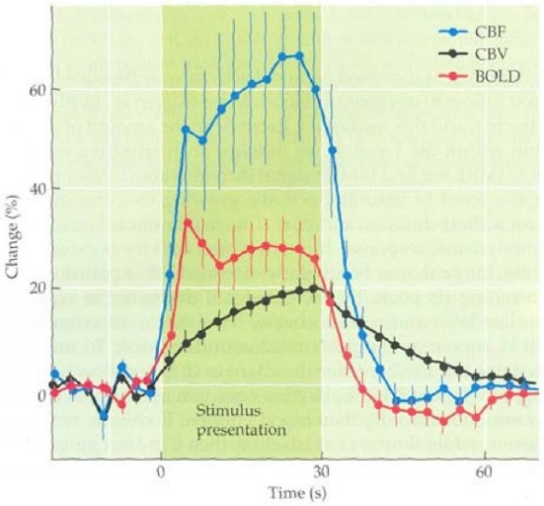

Figure 1.4: Cerebral *blood flow (CBF), blood volume (CBV), and BOLD signal trends over time* [18].

The hemodynamic response (HDR) is defined as the variation in the magnetic resonance signal. The HDR does not have a constant shape but varies depending on the stimulus generating it: an increase in stimulation frequency and thus neural activity increases the amplitude of the HDR, while a prolongation of its duration leads to an increase in the duration of the HDR itself (Figure 1.5). Determining the exact relationship between neural events and the shape of the HDR is complex because their dynamics are entirely different. Neural responses exhaust in a few tens of milliseconds, while the first variations in the hemodynamic response are observed after 1 or 2 seconds. This occurs because the measured signal originates from a sequence of physiological events that lead to the generation of the HDR [18].

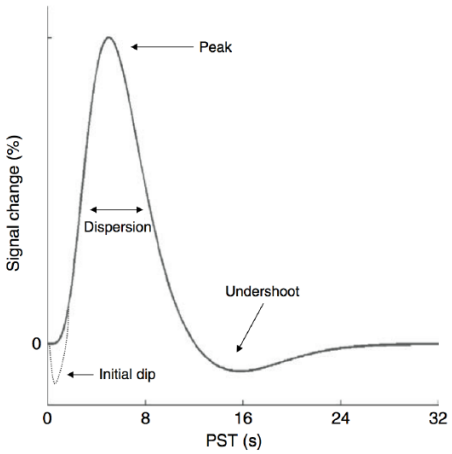

Figure 1.5: *Time course of the hemodynamic response* [19].

It is worth noting that the BOLD signal relative to a voxel reflects the total amount of deoxygenated haemoglobin present but is also influenced by noise from various sources, often reaching amplitudes of the same order of magnitude as the measured signal.

Origin of spontaneous resting-state fMRI signals

The modulation of the BOLD signal concerning the performance of a specific task or in response to a stimulus allows for linking brain topography to the stimulated function. Furthermore, spontaneous variations in the BOLD signal, unrelated to external stimuli, contribute to brain activity, often regarded as noise in fMRI studies involving task performance. The interest in exploring studies on such "noise" is motivated by two main considerations, one of an energetic nature and the other to experimental observations.

The first considers that the brain represents only 2% of the total body mass but consumes 20% of the energy. Studies confirm that the brain utilises 60–80% of the energy for communication between neurons and their supporting cells, which is the inherent activity, whereas for elicited activity the brain utilises only 0.5–1.0% of the total energy [20]. In fact, increases in neuronal metabolism in the presence of functional tasks are usually less than 5% of energy consumption in their absence, indicating that spontaneous fluctuations largely contribute to brain energy expenditure. These findings suggests that the major portion of energy consumption is utilised for the spontaneous neuronal activities, not attributable to a specific input or output, that represent neural activity intrinsically generated by the brain [21].

The second consideration pertains to experimental observations revealing that spontaneous activity during the resting state is not random noise but exhibits organized patterns [22]. In fact, among the rs-fMRI pioneering studies, those by Biswal and colleagues, was the first to demonstrate correlations between resting-state time-series from a voxel in the motor network with different brain regions, suggesting ongoing information processing even in the absence of external stimuli [22], [23]. The group of Fox et al. described the interactions at rest among certain cortical regions and they found that by using the posterior cingulate cortex as the purpose of the analysis, it was possible to find regions whose signal was positively correlated, such as the medial prefrontal cortex. While, the brain activity of other regions, such as the intraparietal sulcus, the frontal eye fields, and the medial temporal lobe had a strong negative correlation [24]. Then, several studies mark that during rest the brain network is not idle, but rather shows

a vast amount of spontaneous activity that is highly correlated between multiple brain regions [25], [26], [27]. All these studies agreed that resting state signals are consistent spontaneous low frequency fluctuations in the BOLD signal, particularly in the range ~0.01–0.1 Hz.

To study this activity using fMRI, it is necessary to minimizing sensory inputs and avoiding cognitive tasks. In a typical resting-state fMRI experimental setup, subjects are instructed to lie with their eyes closed and to refrain from falling asleep, so that the brain is awake and conscious but relaxed and free from stimuli. This technique allows for studying the temporal correlation of the BOLD signal in distinct brain regions, in the absence of task [28].

Over the years, there has been considerable discussion regarding whether the resting-state BOLD signal is influenced solely by physiological processes unrelated to neuronal activity. Specifically, cardiac and respiratory movements, along with their low-frequency modulations, have been identified as potential sources of distortion in the signal, leading to false correlations across anatomically distinct brain regions.

However, support for a possible neuronal basis of resting-state fMRI signals comes from the observation that most of the resting-state patters manifest between brain regions sharing functional and neuroanatomical overlaps, such as those within the motor, visual, and auditory networks [22], [29], [30] , [31], [32], [33]. This observation suggests that brain regions that often work together form a functional network during rest, characterized by synchronized spontaneous neuronal activity across anatomically separated regions that form the network. Further support for a neuronal basis of resting-state fMRI signals comes from studies which report that the observed spontaneous BOLD signals are mainly dominated by lower frequencies (b 0.1 Hz) so, frequencies higher than 0.3 Hz, such as those of cardiac and respiratory oscillations, contribute minimally to the signal [34], [35] . Fluctuations with oscillations at frequencies lower than 0.1 Hz have been observed for arterial carbon dioxide concentration, brain blood vessel diameter, cerebral blood volume and flow, tissue oxygenation, and cortical oxidative metabolism. Among these, variations in arterial diameter deserve particular attention due to their immediate effect on the BOLD signal [21]. Additionally, support for the neuronal origin hypothesis stems from studies demonstrating associations between resting-state fMRI

correlations and electrophysiological recordings of neuronal firing [36] and spontaneous BOLD fluctuations with concurrent fluctuations in neuronal spiking [37], [38].

Despite these findings, non-neuronal influences can still contaminate resting-state signals. Consequently, efforts to mitigate these influences are becoming standard practice in the preprocessing of resting-state fMRI data [39], [40], [41]. Methods include removing physiological signals during scanning and regressing non-grey matter signals from the fMRI data [42], as well as employing high sampling rates to prevent aliasing of high frequencies into the lower resting-state frequencies of interest [33], [34], [35].

Apart from contributions of the aforementioned physiological processes, low-frequency BOLD fluctuations in the resting state can be considered as a sum of two terms. The first term is related to the subject's conscious mental activity during acquisition, similar in concept to the modulation of the signal induced by an external stimulus and may vary depending on the subject's activity. The second term, representing the main component, is instead related to intrinsic activity and persists in different states and conditions such as sleep or anaesthesia [21].

Resting-state fMRI data processing methods

Temporal correlations among signal fluctuations in different resting-state brain regions have been interpreted in terms of functional connectivity (FC), indicating the level of functional communication between them. These connectivity patterns have been represented as networks among active brain regions, termed *resting-state networks* (RSNs) [21] .

The approaches used to analyse these networks can be categorized in two groups: model-dependent and model free methods.

The model-dependent, often referred to as *seed-based analysis*, was the first method adopted by Biswal et al. to identify the RSNs and involves correlating the resting-state time-series of a selected brain region (referred to as the seed) with the time-series of all other brain regions. This generates a functional connectivity map (fcMap) illustrating the functional connections of the chosen seed region [23], [34], [43]. While fcMaps provide insight into the functional connections of the seed region, they offer limited information on whole-brain connectivity patterns.

On the other hand, model-free methods allow for the exploration of connectivity patterns across the entire brain without the need for defining a priori seed regions. These methods

aim to identify general patterns of connectivity across brain regions. Examples of model-free methods applied to resting-state fMRI data include *principal component analysis* (PCA) [44], *independent component analysis* (ICA) [45], [46], [30], [47], *hierarchical* [48], [32], *Laplacian* [49], and *normalized cut clustering* [33].

ICA-based methods, for instance, seek to identify spatial sources of resting-state signals that are maximally independent from each other. While ICA methods offer the advantage of analysing whole-brain voxel-wise data and facilitating comparisons between subject groups, they may present a challenge in interpreting results due to the complexity of the data representation [21].

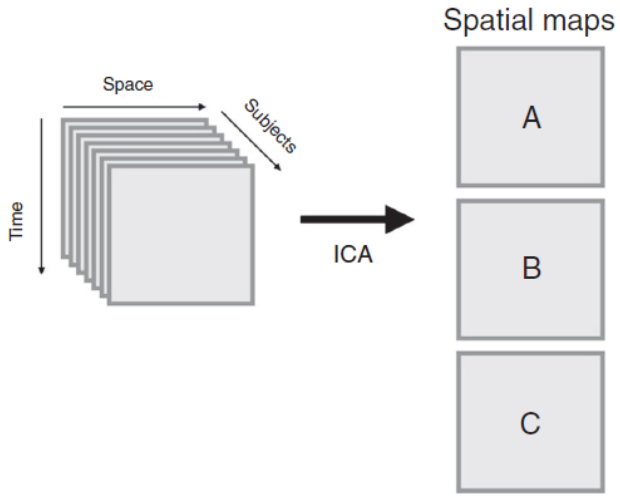

Figure 1.6: *Independent Component Analysis (ICA) is a method used to analyse data from fMRI scans of multiple individuals. It identifies clusters of brain regions whose activity patterns change in a similar way over time and treats them as independent components of the neural network. These components, represented by maps labelled A, B, and C, each involve different brain areas and contribute differently to the overall variability observed in the brain signal* [15].

Instead, clustering methods group data points into subsets based on their similarity, aiming to maximize similarity within subgroups while minimizing it between them. Clustering results may be more directly comparable to traditional fcMap results, as they reflect functional connections between brain regions [32], [33].

Despite their differences, model-dependent, model-free, and clustering methods often yield overlapping results. For example, studies using these approaches have consistently identified networks such as the default mode network and the primary motor network, demonstrating the robustness of these findings across different analytical methods [45], [29], [27], [50], [51]. Similarly, intrinsic functional connectivity between primary visual

and auditory regions has been observed consistently across all three methods [22], [35], [45], [29], [32], [33].

Up until now, neuroimaging studies have identified several networks in the resting-state brain. The most significant evidence of their existence lies in the reproducibility of networks within individuals, consistency of networks across different subjects, and correspondence of cortical areas identified with different study methods. Furthermore, when the correlation of resting-state fMRI time-series between anatomically separated brain regions accurately mirrors ongoing interregional functional communication, there should be a structural core of white matter connections facilitating this neuronal communication. Recent studies have indeed suggested a direct association between functional and structural connectivity in the human brain by combining resting-state fMRI with structural diffusion tensor imaging measurements. Specifically, regions with higher structural connectivity tend to exhibit higher functional connectivity, both locally and on a global whole-brain scale [51].

The main networks identified are the default mode network (DMN), the sensorimotor network (SMN), the visual (V-RSN), the dorsal attention network (DAN), the frontoparietal network (FPN), the salience network (SN), the taxonomy of which is shown in Figure 1.7.

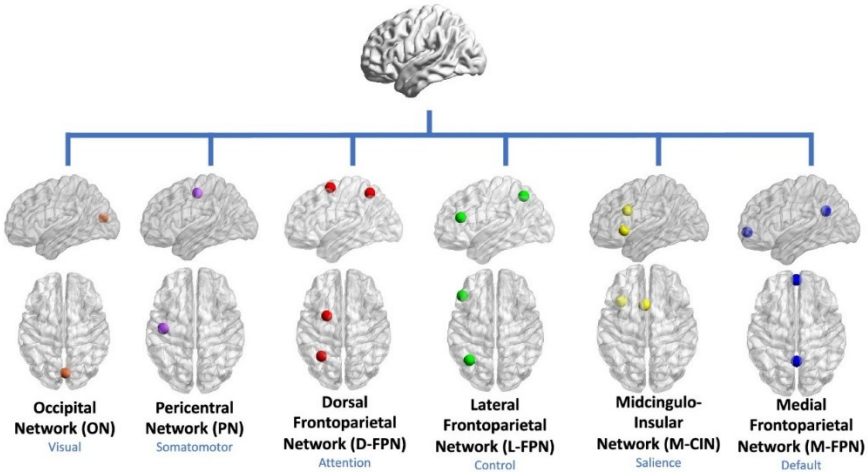

Figure 1.7: *The proposed taxonomy organizes functional brain networks into six broad, anatomically named systems. Each system is associated with specific cognitive domains, shown in blue. While only 1-2 core nodes are shown for each network, it is recognized that numerous other cortical, subcortical, and cerebellar nodes contribute to its functionality* [52].

Default mode network

The default mode network encompasses brain regions such as the posterior cingulate cortex, medial prefrontal cortex, and lateral parietal cortex. This network exhibits heightened activity during periods of rest and is often referred to as the task-negative network because it deactivates during task engagement. Additionally, it plays a role in social cognition, including introspection, mind wandering, and understanding other mental states.

The precuneus, a key component of the default mode network, is characterized by its high metabolic rates during rest and is involved in various cognitive functions. Studies indicate its importance in tasks such as autobiographical memory retrieval, emotional processing, and reward monitoring, highlighting its central role within the default mode network [53].

Sensorimotor network

The sensorimotor network involves a strong functional correlation between the motor cortices of the left and right hemispheres. Within the somatosensory motor cortex, specific areas correspond to different motor functions, such as those related to the legs, hands, and face [53].

Visual network

In the realm of visual processing, distinct medial and lateral cortical areas play crucial roles. Beckmann and colleagues have documented simultaneous activations within the bilateral and medial calcarine sulcus, as well as in extrastriate regions like the lingual gyrus, the inferior portion of the precuneus, and the lateral geniculate nucleus of the thalamus. These activations collectively constitute the visual network, with the lateral geniculate nucleus serving as a functional link between visual input and the primary visual cortex. Their study also identifies specific visual areas within the extrastriate regions, such as the lingual gyrus, the inferior section of the precuneus, and the lateral geniculate nucleus of the thalamus, as components of the medial visual areas. Meanwhile, the occipitotemporal junction, extending from the occipital pole to the superior parietal region, represents the lateral visual areas [45], [29], [54]. Concurrent activations in the posterior parietal cortex, the midline of the precuneus, the posterior cingulate cortex, and the frontal pole collectively constitute the visuospatial network. Numerous studies have highlighted the impact of lesions in the lateral posterior parietal regions on spatial

attention, underscoring the involvement of the posterior parietal cortex in directing attention towards significant visuospatial cues [53].

Dorsal attention network

The dorsal attention network (DAN), also known anatomically as the *dorsal frontoparietal network* (D-FPN), is primarily characterized by the involvement of the intraparietal sulcus (IPS) and frontal eye fields (FEF) of each hemisphere. Additionally, other regions such as the middle temporal region (MT+), superior parietal lobule (SPL), supplementary eye field (SEF), and ventral premotor cortex may also contribute to this network [55],[56]. Its principal function lies in the goal-directed and voluntary orienting of visuospatial attention. This network dynamically interacts with the ventral attention network, based on task demands. The inferior frontal junction plays a crucial role in configuring this interaction between the two networks, particularly during task switches or shifts in attention [57].

F*rontoparietal network*

Generally, also known as the *central executive network* (CEN) or, more specifically, the *lateral frontoparietal network* (L-FPN), it is mainly composed of the dorsolateral prefrontal cortex and the inferior parietal cortex, around the intraparietal sulcus [58]. This network is essential for executive function and goal-oriented tasks, including rule-based problem-solving, working memory manipulation, and decision-making. It dynamically adjusts to cognitive demands, dividing into subsystems interacting with the DMN for introspection and the DAN for perceptual attention [59].

Salience network

Anatomically known as the *midcingulo-insular network* (M-CIN) or *ventral attention network*, this network encompasses the dorsal anterior cingulate cortex, bilateral insula, and presupplementary motor area. Its primary function lies in orchestrating the dynamic changes across various networks, primarily between the FPN and DMN, and is crucial during swift behavioural adaptations. Essentially, decisions regarding subsequent actions or inactions hinge upon the effective operation of this network. Consequently, the proper functioning of the salience network is imperative for initiating the regulation of cognitive processes [53].

Graph theory

Besides the formation of multiple resting-state networks, the human brain forms a unified complex network that interconnects all brain regions and sub-networks into a cohesive system. Graph theory offers a framework to analyse the topology of complex networks, providing insights into both local and global organization of functional brain networks. Functional brain networks are defined as graphs (G=(V, E)), where V represents brain regions (nodes) and E denotes functional connections between these regions. Nodes in the brain network can be cortical regions based on predefined templates or fMRI voxels while functional connectivity between regions is assessed by correlating their time-series data. Graph theory offers a range of parameters to analyse brain functional connectivity (Figure 1.8):

- Clustering-coefficient measures local connectedness by comparing actual connections between neighbours to the maximum possible connections;
- Characteristic path length indicates global communication efficiency, providing information about how close a node is connected to all other nodes in the network;
- Centrality assesses the importance of nodes in interconnecting the network, indicating how many of the shortest paths between the nodes of the network pass through a certain node.
- Node degree measures the total number of connections of a node, indicating its significance in information flow within the network;
- Modularity describes the formation of communities within the network, explaining how strong groups of nodes form relative isolated sub-networks within the full network.

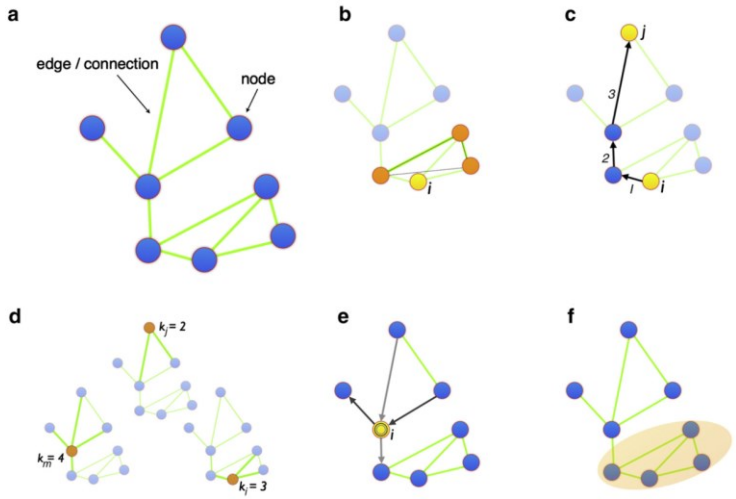

Figure 1.8: *This figure illustrates key properties of graphs representing complex dynamical systems. (a) Shows a graph G = (V, E), where nodes (V) and edges (E) represent interactions. (b) Shows the clustering coefficient, which indicates local connectedness. (c) Shows characteristic path length, indicating global communication efficiency. (d) Shows centrality, highlighting nodes that are central to network connectivity. (e) Shows node degree, indicating overall connectivity. (f) Shows modularity, suggesting the formation of isolated subnetworks* [51].

Advanced graph analysis of resting-state fMRI data has revealed an efficient organization of functional connectivity in the brain network, resembling a small-world organization [60], [61], [32], [62], [63]. As shown in Figure 1.9, small-world networks exhibit high local connectedness and short average travel distance between nodes, combining local and global efficiency [51].

In this context, the concepts of integration and segregation come into play, illustrating, respectively, how regions cooperate or function independently from each other. There has long been debate about the true functional organization of the brain, but it has been understood that these two concepts coexist within the brain's topology and simply describe different yet perfectly complementary aspects of it. Graph theory metrics such as global efficiency and average path length indicate integration, while local efficiency and clustering coefficient reveal segregation. A small-world network, characterized by high local and global efficiency and a short characteristic path length, facilitates prompt communication between nodes. Large-scale networks exhibit slight short-range connectivity and greater influence from long-range functional connectivity. The clustering coefficient and characteristic path length offer insights into the organization of brain networks on a large scale [53].

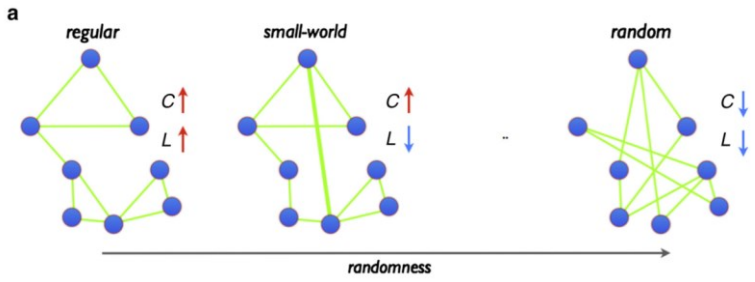

Figure 1.9: *The figure illustrates various organizational characteristics of networks, including regular, random, small-world. (a) A regular network (left) exhibits a high clustering-coefficient (C) and path length (L), indicating local connectivity. In contrast, a random network (right) has lower C and shorter L, showing a more global organization. (b) Small-world networks emerge with low probability (p) of randomly reconnecting connections in a regular network, combining high C with low L, balancing local clustering and global efficiency* [51].

Overall, analysis of resting-state time-series using graph theory has revealed an efficient organization of functional communication within the brain network. This suggests that the human brain is not merely a randomly connected network, but rather one that is finely tuned for optimal efficiency both locally and globally [51].

Building Connectivity Matrices: From Data to Networks

The vast number of potential connections within brain networks, due to its quadratic increase with the number of nodes, necessitates a method for meaningful representation of this data. The common way to represent the connectivity between each pair of nodes in a network is to use a two-dimensional matrix called a connectivity matrix. In this matrix, each row and column corresponds to a different node, and the matrix element positioned at the intersection between the i-th row and j-th column encodes information about the connection between region *i* and *j*, quantified with the correlation values; this representation is fundamental for network analysis [64]. The construction of the network from rs-fMRI images follows four fundamental stages. As shown in Figure 1.10, first, functional images are extracted from the resting state fMRI examination. Subsequently, for proceeding with region of interest (ROI)-based analysis, anatomical parcellation of the brain is necessary. For each region, time series of brain dynamics are extracted, and the connectivity matrix is calculated. Such matrices can be binary connectivity or adjacency matrices indicating only the presence or absence of connections between ROIs; connectivity matrices for weighted graphs represent the pattern of cross-correlation between the BOLD signals estimated from temporal dynamics [65]. At this construction

level, the choice of a threshold is pivotal, impacting graph density and the subsequent analysis metrics quantification.

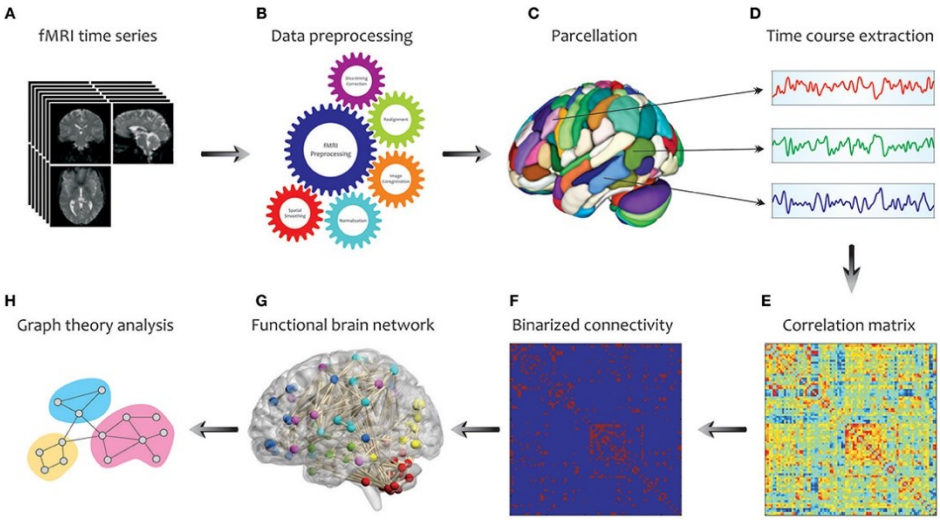

Figure 1.10: *Schematic of brain network construction and graph theoretical analysis using fMRI data: A. acquisition of rs-fMRI images, B. preprocessing steps of raw data, C. anatomical parcellation for ROI-based analysis, D. multiple time series extraction from each region, E. generation of correlation matrix, F. binarization of correlation matrix, G. construction of the corresponding functional brain network, H. graph analysis using descriptive metrics* [66].

Thus, the choice of a specific combination of mapping methods, parcellation, and connectivity measures must be carefully motivated as it determines the final neurobiological network's topology interpretation.

The diagonal elements in a connectivity matrix represent a node's self-connections or intrinsic properties. In macroscopic brain networks, they can signify properties or functional roles of each brain region. However, in functional connectivity networks, the diagonal may reflect variations in local dynamics. Typically, the diagonal is assigned a common value for all nodes, and its individual differences are often disregarded. Off-diagonal elements denote connectivity between distinct neural elements, with values representing connectivity strength. These elements can be categorized into a lower triangle (below the diagonal) and an upper triangle (above the diagonal) for organizational purposes. Different values in the upper and lower triangles of a connectivity matrix indicate an asymmetric matrix, known as *effective connectivity matrix*, representing a directed graph or network. These asymmetries encode the directions of connections, allowing for the mapping of influence between network nodes. In graphical representations, arrowheads signify the direction of connectivity, pointing towards the target of each connection. This kind of connectivity can be studied using advanced

techniques such as *Dynamic Causal Modelling* (DCM) or non-invasive brain stimulation. If the upper and lower triangles are identical, the matrix represents an undirected graph or network, which identifies connections between specific pairs of nodes but does not specify their directions. This is the case of the *functional connectivity matrix*, quantified with the correlation coefficient in the time domain or the coherence in the frequency domain [64]. Not all connections between neural elements are equal because there could be some pairs of neural elements with more synapses or more myelinated fibers that speed up signal transmission. These variations can be described by differences in connectivity weights, denoted as w_{ij}, for each pair of nodes i and j, resulting in a weighted graph or network. So, the methodology used to estimate connectivity influences weight interpretation, with sensitivity and resolution affecting weight accuracy. For instance, methods like correlation-based estimates yield w_{ij} values ranging from -1 to 1, representing perfect negative to perfect positive correlation. Brain networks can also be binary networks that indicate where connections exist in the network but do not provide information about variations in connectivity weight between different network nodes [67].

This passage highlights that the brain is not entirely connected, as only a small fraction of potential connections among neurons are realized. Most methods for assessing brain connectivity encounter measurement noise, making it challenging to distinguish real connections from spurious ones. To mitigate this, a cutoff value is often applied to connectivity matrices to filter out noise and retain significant connections. Negative correlation values in connectivity matrices pose a challenge, with differing opinions on their significance and treatment. The group of Sporns et al. advocate for their removal before addressing the analysis of brain networks or redefine some graph metrics to include negative weights in network analyses [67]. Determining an appropriate thresholding strategy is complex, with various approaches proposed in the literature, including fixed thresholds, density-based thresholds, and thresholds based on correlation sparsity [68]. However, these thresholds represent uniformly applied thresholds to the entire network, meaning all brain links are cut in the same manner. Another research group, particularly Wang et al. (2009a), has added, in addition to the absolute threshold, a threshold relative to the sparsity of correlation values in the matrix, meaning a percentage of connections,

chosen by the user, is eliminated with the assurance of maintaining the coexistence of both positive and negative weights [69].

After applying a threshold to the connectivity matrix, the next step could be the binarization to identify existing connections and their locations, providing an overview of the connectome's basic architecture. Binarization helps mitigate variations in weighted network properties and biases in connectivity estimation methods [70], [71], [72]. However, binarization may overlook valuable information about signal flow between neural elements, that instead are identified in high resolution brain networks [73], [74]. Therefore, analysing both binary and weighted matrices is crucial for understanding the relationship between connectivity weights and network topology.

Clinical relevance of rs-fMRI

Resting-state studies offer a promising avenue for comparing resting-state networks between different groups without the need for task engagement, making them applicable to individuals unable to participate in specific experimental paradigms, like ones with brain tumours and epilepsy. These studies are less sensitive to experimental variations and execution, allowing for robust comparisons between healthy individuals and those affected by neurological or psychiatric conditions. Resting-state fMRI has been instrumental in identifying alterations in RSNs associated with various conditions such as Alzheimer's disease, multiple sclerosis, schizophrenia, autism, epilepsy, and attention deficit hyperactivity disorder (ADHD) [75], [76]. This approach has not only advanced diagnostic tools but also identified markers of complications, such as the onset of psychosis in depressed patients. The extent of variation in RSNs correlates with disease severity or functional recovery, suggesting its potential for diagnostic and prognostic purposes in neurological and psychiatric disorders [77]. Moreover, resting-state fMRI enables the assessment of brain activity during sleep, anaesthesia, or vegetative states, providing valuable data for multiple analyses from a single dataset [21].

Overall, there is potential clinical utility of rs-fMRI in identifying functional disruptions of the brain network that occur in the context of gliomas [78], [79], [80], [81], [82], [83]. Gliomas, which encompass various types of brain tumours originating from glial cells, are classified into four grades by the World Health Organization (WHO) based on microscopic appearance and clinical severity. Approximately 30% of brain tumours are gliomas, with most fast-growing tumours falling into this category. The most aggressive

form, glioblastoma, represents a primary lethal brain tumour, with less than 5% of patients surviving 5 years despite optimal treatment [84]. Multiple studies highlight rs-fMRI's ability to delineate network variations in glioma patients. For instance, Otten et al. were the first to report a correlation between motor deficits and reduced connectivity within motor functional networks. Changes in functional connectivity within the default mode network (DMN) are also observed, particularly in higher-grade gliomas [80], [85]. However, the relationship between tumour grade and functional connectivity changes remains debated, with some studies finding significant correlations while others do not [86]. While, when analysing subgroups of patients based on the glioma's location, Zhang et al. find a significant correlation between left intra-hemispheric functional connectivity and tumour grade [86]. Several studies attempt to localize the extent of tumour influence using rs-fMRI through seed-based analysis. For instance, Chow et al. employed this approach to assess disruptions in vascular regulation induced by glioblastoma. The findings indicate that the spatial distribution of these disruptions is localized in the immediate vicinity of the tumour and peri-tumoral oedema [87]. Additionally, Agarwal and colleagues demonstrate the existence of *neurovascular uncoupling* (NVU) occurring in regions ipsilateral to gliomas involving the primary motor and somatosensory cortex [83]. In summary, the discussed studies provide compelling evidence of localized alterations occurring within the context of glioma. Various studies attempt to correlate rs-fMRI findings with prognostic factors, suggesting potential implications for treatment planning and monitoring. Tuovinen et al. (2016) evaluate connectivity changes occurring during adjuvant radiotherapy in glioma patients, concluding that tumour localization relative to network hubs is influential, as evidenced by the transient overall improvement in post-radiotherapy connectivity when the lesion is near a hub [88]. Similarly, other studies assess long-distance connectivity and network topology, finding a reduced long-distance interhemispheric connectivity in patients alongside increased local efficiency, while other parameters such as clustering coefficient, global efficiency, and small-world property remain preserved [89], [90]. After, in asymptomatic patients, Niu and colleagues describe a significant reduction in interhemispheric functional connectivity, confirming the vulnerability of long-distance connections, especially interhemispheric networks [91]. Therefore, even being only some initial findings, graph analysis approaches depict

various local and non-hub network changes potentially correlating with some neurocognitive symptoms observed in glioma patients.

Additionally, Harris and colleagues demonstrate that tumours in the parietal lobe exhibit a more compromised DMN compared to tumours located in the frontal lobe, while tumours within and outside network nodes are not significantly different. The authors did not find a statistical association between DMN connectivity and tumour size on T2-weighted images, suggesting that large lesions may not necessarily disrupt the DMN unless they have histopathological features of malignancy, but they may instead shift neural connections between functional regions [80]. Ghumman et al. argued that tumours in the left hemisphere have a greater effect on DMN connectivity regardless of their size and type, suggesting that DMN connectivity in the left side of the brain may be more vulnerable to lesions [79].

Furthermore, investigations into the reorganization of brain networks in response to gliomas shed light on the brain's compensatory mechanisms and functional plasticity. As outlined in previous studies regarding network plasticity observed in low-grade gliomas, there can be an intrinsic reorganization of brain networks to allow for functional compensation [81]. Consequently, the altered interhemispheric functional connectivity depicted in various studies might reflect tumour infiltration or the "recruitment of compensatory areas from brain regions surrounding slow-growing gliomas"[91]. However, discrepancies in findings across studies underscore the need for standardized methodologies and further research to optimize the application of rs-fMRI in glioma's studies.

In the outlined context, this thesis also aims to integrate functional information obtained from rs-fMRI scans of glioma patients with glucose metabolism data obtained from PET scans of the same patients. The objective is to identify patterns of co-variation for both data modalities compared to control subjects, thereby providing a combined functional and metabolic basis for the observed differences in patients.

1.2.2 Principles of [^{18}F]FDG-PET: acquisition and analysis

Positron Emission Tomography (PET) is a powerful imaging that utilizes chemical analysis and involves the use of a small amount of radioactive material, known as a radiopharmaceutical, to examine metabolic activity within the body.

The origins of PET trace back to the discovery of positrons in 1932 by Carl D. Anderson. In the 1950s and 1960s, scientists like David Kuhl and Roy Edwards began exploring the potential use of positrons to create three-dimensional images of the human body. Theoretical foundations were laid by Enrico Fermi in 1942 with equations describing neutron transport, which provided a basis for PET image reconstruction algorithms.

The first functional PET scanner was developed in the 1950s by Brownell and colleagues at the University of Washington, using a single camera to detect positrons emitted by radiopharmaceuticals. Technological advancements, such as the introduction of multi-ring detectors in 1976 by Ter-Pogossian and Phelps, significantly enhanced PET's efficiency and speed. From the 1980s onwards, PET gained widespread clinical use in tumour diagnosis, cardiac and neurological disease assessment, and oncological therapy guidance. Concurrently, it became a vital tool for scientific research, particularly in neuroscience and pharmacokinetics. PET also aids in identifying biochemical changes within organs or tissues, allowing for the detection of deviations from normal metabolic processes and the assessment of disease-related mechanisms [92].

Currently, the most used radiopharmaceutical in PET imaging is [^{18}F]fluoro-D-glucose (FDG), that serves as a biomarker for glucose metabolism within the brain, functioning as an analogue of glucose. As already mentioned, glucose is the primary energy source in the brain, particularly in regions like the cortex and deep structures of the grey matter. Thus, understanding regional metabolic ratios in the brains of healthy individuals is crucial for comprehending changes in brain function associated with disease states.

The PET acquisition process typically begins with the intravenous injection of the [^{18}F]FDG radiotracer in the patient, that once in the bloodstream, behaves similarly to glucose, being taken up by metabolically active tissues. Following injection, there is a period during which the radiotracer accumulates in the tissues of interest. This uptake period allows sufficient time for [^{18}F]FDG to be transported from the bloodstream into cells, primarily via the glucose transporter GLUT1. Once inside the cells, it undergoes phosphorylation by hexokinases (HXKs) to form FDG-6-phosphate, which is then stored within the cells. The patient then undergoes a PET scanner. The PET scanner consists of a ring of detectors that measure the gamma rays, with energies of 511 keV each, emitted by the positron-electron annihilation events that occur when the positrons emitted by [^{18}F]FDG collide with electrons in the tissue. When the photons reach the detector, named

scintillator, they produce a bright signal that can be detected by photomultiplier tubes. The goal is to reconstruct the point of emission of the photons within the body, thereby creating an image map of the organ or tissue being examined. The intensity of the signal in the image correlates with the amount of radionuclide collected in the tissue, providing quantitative metabolic information, typically expressed in units such as counts/sec or Bq/ml, in contrast to MRI scans [93]. Then, PET data are typically stored in a large matrix, with each voxel assigned a value representing the concentration of radioactivity.

The resulting PET images could be static or dynamic (Figure 1.11), based on how radiation have been captured and analysed. In static imaging, also known as single-frame acquisition, the scanner captures the volumetric concentration of radioactivity within a short timeframe after injection, typically ranging from 5 minutes to 2 hours. These data generate a voxel-by-voxel map, with regions of high radiation indicating areas of elevated glucose usage. This method, favoured for its cost-effectiveness and ease of patient management, is commonly utilized in clinical settings, particularly in oncology and cardiac examinations.

In contrast, dynamic PET (multi-frame acquisition) continuously measures volumetric radioactivity. The subject undergoes scanning before tracer injection, and the tracer is introduced during active scanning. This approach generates a series of snapshots capturing changing concentrations of radiotracer per scanning interval, providing a volumetric concentration-time profile for glucose metabolism. Typically, the time frames have increasing durations to optimize the scanner's count statistics. Kinetic models assess the rate and distribution of radioactivity uptake, decay, or tracer release on a voxel-by-voxel basis. Dynamic PET finds significant application in neuroscience research, especially for studying tissue metabolism and receptor density [94].

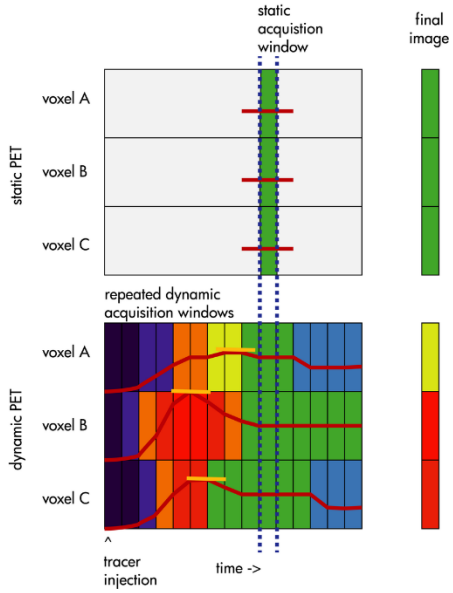

Figure 1.11: *Differences between static and dynamic PET. In static PET, radiation amounts are mapped voxel-by-voxel over a fixed acquisition window starting after tracer injection, resulting in voxels (i.e. A, B, and C) with similar absolute radiation counts. Conversely, dynamic PET captures tracer uptake in time windows, enabling kinetic analysis to distinguish among voxels* [94].

One of the key advantages of FDG is its slow release from tissues once trapped as [^{18}F]FDG-6-P, preventing further metabolism. In contrast, glucose-6-phosphate, a product of glucose metabolism, continues along the glycolytic and glycogen synthesis pathways. However, it's important to note that since [^{18}F]FDG is a glucose analogue, adjustments need to be made to account for differences in transport and phosphorylation compared to glucose itself. This adjustment is achieved through a numerical factor called the *Lumped Constant* (*LC*), which represents the ratio of FDG (E^{FDG}) to glucose (E^{GLU}) phosphorylation rates, essentially correcting for differences in intracellular metabolic pathways between FDG and glucose. *LC* is defined as:

$$LC = \frac{E^{FDG}}{E^{GLU}}$$

The lumped constant is typically assumed to be constant across different brain regions and experimental conditions, but variations can occur particularly under certain physiological or pathological conditions, including insulin levels or oxygen availability, which may necessitate its adjustment for accurate interpretation of PET data [95].

[^{18}F]FDG-PET data analysis methods

PET images can be analysed qualitatively or quantitatively depending on the research goals. Visual interpretation can provide valuable qualitative information about the

distribution of the radiotracer within the body, since areas of increased [^{18}F]FDG uptake may indicate regions of heightened metabolic activity, which can be indicative of pathology. However, quantitative analysis is often necessary to establish relationships between PET tracer concentration and underlying physiological or biochemical processes. This requires applying mathematical models to describe tracer kinetics in specific regions of interest.

All PET quantification methods aim to relate scanner-detected radioactivity measurements to the metabolic processes involving the injected tracer, with the fundamental assumption that the tracer does not interfere with the system's functioning in vivo.

For static PET acquisitions, quantification typically involves calculating the semi-quantitative Standardized Uptake Value (*SUV*) index or the tissue-to-plasma ratio. *SUV* is calculated based on the radiotracer concentration measured by PET over a specified time interval, typically 45-60 minutes post-tracer injection, normalized by the injected dose and subject's body weight (or body surface area), as shown by the formula:

$$SUV = \frac{[^{18}F]FDGconcentration}{injected\ dose / NF}$$

The injected dose, measured in milliCuries or MBq, is the total amount of radioactive tracer administered to the patient. NF (normalization factor) adjusts for anthropometric characteristics such as body weight, body surface area, or lean body mass, so that *SUV* provides a standardized metric.

In practice, the most used quantitative method for intra- and inter-subject regional comparisons is the Standardized Uptake Value Ratio (*SUVR*). It is calculated by dividing the uptake value of the tracer in a ROI by the uptake value in a reference region, usually a region of the brain considered to be unaffected by the pathology under study or less affected by the biological process under investigation:

$$SUVR = \frac{ROI\ [^{18}F]FDG\ uptake}{Reference\ Region\ [^{18}F]FDG\ uptake}$$

This ratio is then normalized to a reference value, often the peak tracer uptake in the brain at the time of image acquisition. Common reference regions in *SUVR* analyses include the cerebellum, region of the brain considered to be unaffected by the pathology under

study or less affected by the biological process under investigation, the occipital cortex, and basal brain regions such as the brainstem. The choice of reference region depends on the specific research question, the characteristics of the investigated pathology, and the individual's conditions undergoing PET examination.

The use of *SUVR* is common in both research and clinical practice to study the distribution of radiolabelled tracers in the brain and in neurodegenerative diseases such as Alzheimer's [96] and Parkinson's disease [97]. It provides a relative measure of tracer accumulation, allowing convenient and straightforward comparison between patients and assessment of disease progression over time [98].

Although these advantages, its accuracy can be influenced by various physiological and technical factors. Therefore, it is essential to conduct prior validation, ensuring the reproducibility of *SUV* (or *SUVR*) measurements, confirming their alignment with the physiology and kinetics of the tracer, and verifying their capability to differentiate between healthy and pathological tissues within a specific tracer and imaging system setup.

Dynamic PET acquisitions offer more informative data that can be analysed with three main classes of models: spectral analysis modelling, graphical methods, and compartmental models. The main difference among them is that the first two are based on linearity assumptions, so they can be used in a steady-state physiological system, limiting the exploration of the real radiotracer kinetic. Compartmental models, first introduced by Sokoloff and colleagues in 1977, provide a detailed description of physiological processes by postulating linear or non-linear structures of interconnected compartments. These models require dynamic PET images to capture temporal changes and involve a system of first-order differential equations to describe material flow between compartments, representing transport or chemical transformations. Compartmental modelling, though more complex, offers a comprehensive understanding of physiological processes or disease pathogenesis by revealing underlying mechanisms. The first model proposed by Sokoloff and colleagues, recognized as two-tissue compartmental model, has been initially applied to quantify cerebral glucose consumption using the tracer 2-[^{14}C]deoxyglucose [99]. In these models, researchers first hypothesize a linear or nonlinear structure comprising interconnected compartments, each representing distinct physiological or biochemical processes such as diffusion, transport,

metabolism, and receptor-ligand binding. Each compartment, symbolized by a circle, represents a well-mixed and kinematically homogeneous quantity of material. Mathematical equations describing the time-dependent dynamics of these compartments are typically based on first-order differential equations. Consequently, dynamic PET imaging is required to capture these temporal changes. Arrows between compartments signify the flow of material due to transport or chemical transformations.

Sokoloff's two-tissue compartmental model was later adapted for [^{18}F]FDG PET studies in various tissues and organs. In this model, illustrated in Figure 1.12, C_p represents the arterial plasma concentration of [^{18}F]FDG, C_1 denotes the tissue concentration of [^{18}F]FDG, and C_2 represents the concentration of [^{18}F]FDG-6-P in the tissue.

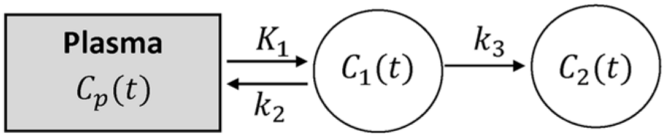

Figure 1.12: *Two compartment, three rate constant model for quantification of the [^{18}F]FDG proposed by Sokoloff and colleagues* [100].

Microparameters such as K_1 and k_2 describe the kinetics of forward and reverse [^{18}F]FDG transport across the cell membrane, while k_3 represents the rate constant of [^{18}F]FDG phosphorylation. Estimation of these model microparameters is facilitated by arterial plasma sampling and dynamic PET imaging. It's important to specify that K_1 is denoted with a capital letter because it has a distinct unit of measurement (ml/cm^3/min or ml_{plasma}/ml_{tissue}/min) compared to other parameters that have unit per minute (min^{-1}).

The kinetics of the tracer within the tissue can be described by the following first-order differential equations:

$$\begin{cases} \dfrac{dC_1(t)}{dt} = K_1 C_p(t) - (k_2 + k_3) C_1(t) & C_1(0) = 0 \\ \dfrac{dC_2(t)}{dt} = k_3 C_1(t) & C_2(0) = 0 \end{cases}$$

Following the injection of [^{18}F]FDG into the bloodstream, the total concentration of radioactivity in the tissue, denoted as C_i, comprises both [^{18}F]FDG and [^{18}F]FDG-6-P concentrations at any given time. Thus, it can be written as the sum of these two contributions (ignoring the contribution from blood in tissue vasculature):

$$C_i(t) = C_1(t) + C_2(t)$$

However, since PET scanners have a limited spatial resolution, measurements of tracer concentration in a ROI encompass not only tissue but also the concentration of ^{18}F in the blood volume within it. Therefore, the blood volume fraction V_b (for brain and skeletal muscle) of the tracer concentration (C_b (t)) in whole blood, must be factored into the calculation as:

$$C_i(t) = (1 - V_b)\big(C_1(t) + C_2(t)\big) + V_b C_b(t)$$

Then, microparameters are quantified with the weighted non-linear least squares estimator. Usually, V_b is fixed at a physiologic value of 3-5% to reduce the number of fitted parameters. In this method, weights are determined as the inverse of the variance of PET measurement errors. One widely used formula for estimating variance is:

$$var(t_k) = \frac{C(t_k)}{\Delta t_k}$$

Where $C(t_k)$ represents the mean measured tracer activity over the k_{th} relative scan time interval Δt_k. However, in cases of highly noisy data, such as at the voxel level, this estimator may encounter challenges related to convergence, lengthy computation times, and sensitivity to initial estimates, necessitating alternative estimation approaches.

From microparameters, the macroparameter of interest, that is the fractional uptake of [^{18}F]FDG, K_i, can be derived as follows:

$$K_i = \frac{k_1 k_3}{k_2 + k_3}$$

Once K_i is known, the regional metabolic rate of glucose can be calculated using the formula:

$$CMR_{Glu}kinetic = \frac{C_{p-g}}{LC} \times K_i$$

where $C_{p\text{-}g}$ denotes the arterial plasma glucose concentration, and LC is the Lumped Constant [101].

ROI and voxel-level analysis

In quantitative analysis of PET data, physiological information can be computed either by focusing on specific regions or by examining individual voxels. Analysing ROI generally yields more reliable results because it averages voxel data within the ROI, effectively reducing noise, especially in dynamic PET studies. On the other hand, voxel-level analysis produces parametric maps with high spatial resolution, which can reveal details not easily visible in ROI analysis, such as small lesions.

However, in this case, the weighted non-linear least-squares estimator would have three problems that make their use challenging: lack of convergence due to the low signal-to-noise ratio, inacceptable precision of parameter estimates and non-physiological estimates (e.g.., < 0 or > 1). Thus, more efficient algorithms are required. Various methods, such as the GLLS method (Feng et al.,1993), basis function methods (Gunn et al.,1997) (Hong et al., 2010) (Rizzo et al.,2013), and Bayesian approaches (Tomasi et al.,2009) (Rizzo et al.,2012), have been proposed and validated for voxel-level quantification. Among these, the Bayesian methods offer a promising alternative by incorporating prior information on tissue kinetics. The critical point is that the computation of the posterior distribution, involving numerical integrations, is, most of the times, computationally intensive. The Variational Bayesian (VB) approach presents a solution by approximating the posterior distribution to make it numerically tractable. This method, already implemented in PET studies for reconstruction [102], [103] and segmentation, has been adapted for kinetic PET modelling, tailored to the noise distribution characteristics [104]. In the VB approach, prior information assists in estimating the parameter vector ϑ, given a model $y(y=C(\vartheta,t))$ and a set of measurements z. Data-driven prior distributions, established at the ROI level using weighted non-linear least squares estimates, are propagated to the voxel level as prior information. The goal is to refine the prior information $P(\vartheta|y)$ with the data z to derive the posterior distribution $P(\vartheta|z,y)$ of the parameter vector ϑ. Bayes' rule links the posterior and prior distributions (neglecting the dependence on y) as:

$$P(\vartheta|z) = \frac{P(z|\vartheta)P(\vartheta)}{P(z)}$$

where the probability density function $P(z|\vartheta)$, known as likelihood, describes the data z given ϑ and y. In VB approach:

$$\hat{\vartheta} = \arg\min_{\vartheta} P(\vartheta|z)$$

thus, in practise, the numerical integrations involved in the calculus of $P(\vartheta|z)$ make the problem intractable. In fact, in real applications, the VB methods make integrals tractable by approximating the posterior with a simpler function $Q(\vartheta)$ [105]. The goal is to minimize the difference between the real and approximate posterior, quantified by the Kullback-Leibler divergence [106]:

$$KL[Q(\vartheta)||P(\vartheta|z)] = logP(z) - F$$

Where the free energy term *F* is defined as:

$$F = \int Q(\vartheta) log \frac{P(z|\vartheta)P(\vartheta)}{Q(\vartheta)} \, d\vartheta$$

Since the logarithmic term in the Kullback-Leiber divergence does not depend on ϑ and it can be ignored, and assured that *K L* divergence is non-negative, it can be minimized by maximising *F*. To simplify integrals, VB employs a mean-field approximation for the approximate distribution $Q(\vartheta)$, dividing parameters into model parameters (ϑ) and noise-related parameters (φ). Each group has its own approximate distribution $Q_\vartheta(\vartheta|z)$ and $Q\varphi(\varphi|z)$, which are assumed independent, so that:

$$Q(\vartheta) = Q_\vartheta(\vartheta|z)Q_\varphi(\varphi|z)$$

$Q(\vartheta)$ and the likelihood have the same structure, facilitating the integration that became an updating process of posterior hyper-parameters [105].

Integration of kinetic parameter estimation with 4D image reconstruction aims to reduce noise-induced bias and variance compared to traditional post-reconstruction analysis. Despite the chosen level of analysis, PET imaging is susceptible to confounding effects, such as motion artifacts, which blur images and degrade spatial resolution, especially problematic in thoracic studies. Motion correction methods typically involve image registration algorithms or hardware motion tracking, but standardization is lacking outside brain studies.

The second main problem is the so-called partial volume effect: referring to tissue heterogeneity within voxels or ROIs, it presents challenges in both ROI-based and voxel-based analysis, complicating mathematical modelling and potentially confounding quantification. Spillover activity, that means surrounding tissues contribute to radioactivity measurements with their very specific and high tracer activity, is the third main problem that can lead to overestimation. Correction strategies are available but are computationally intensive and rely on detailed anatomical MRI data and prior knowledge of tracer distribution [100].

Metabolic connectivity analysis

Recent advancements in PET imaging have led to the use of FDG to quantify metabolic connectivity (MC), reflecting the interplay between metabolic rates across different brain regions. Horwitz et al. (1984) pioneered the concept of inferring functional associations between different brain regions based on metabolic activity, predating the introduction of

fMRI. Using [^{18}F]FDG-PET on forty healthy adult men under conditions of reduced auditory and visual input, they conducted a correlational analysis calculating the partial correlation coefficients for regional cerebral metabolic rates for glucose (*rCMRGlu*), while controlling for whole brain glucose metabolism (*CMRGlu*). This study demonstrated that homologous brain regions exhibited the highest partial correlation coefficients, indicating significant inter-regional correlations ($p < 0.01$), with the strength of association proportional to the correlation coefficient magnitude. Additionally, there were no significant differences between hemispheres, suggesting similar functional connectivity patterns. Significant correlations were observed between primary somatosensory and frontal lobe regions, but not between primary visual and auditory areas. Notably, numerous correlations were found between frontal-parietal and temporal-occipital lobe regions, with fewer significant correlations between these two domains.

Overall, the study demonstrated that metabolic connectivity obtained with FDG-PET offers valuable insights into brain activity and cognitive function. This is particularly valuable in diagnosing degenerative diseases, as alterations in large-scale brain networks often accompany such conditions [107].

Numerous studies in the literature have predominantly relied on conventional static measures instead of leveraging the temporal information available from dynamic PET scans. These static measures are typically used to derive *group-level metabolic connectivity*, referred to as *across-individual* MC (ai-MC) [108]. These approaches include seed correlation or IRCA (Lee et al.,2008), principal component analysis and independent component analysis (Di and Biswal, 2012), sparse inverse covariance estimation (SICE) (Huang et al.,2010), also known as graphical lasso, and graph theory (Yao et al.,2010). Seed correlation involves selecting a reference site and quantifying the correlation with FDG uptake for every other voxel in the brain. PCA and ICA are multivariate decomposition techniques imposing orthogonality and statistical independence constraints on derived components. SICE estimates the connectivity map by imposing a sparsity constraint on the precision matrix. Graph theory utilizes a similarity matrix where sparsity is achieved by applying a threshold to correlation values, resulting in binary adjacency matrices. Metabolic connectivity from static [^{18}F]FDG PET data is commonly quantified using the semiquantitative values of [^{18}F]FDG uptake (*SUVR*) calculated at a fixed sampling time for each region of interest or voxel.

However, this approach contrast with those used in fMRI studies, where functional connectivity matrices are often derived at the individual-subject level through temporal correlations between signal time series, utilizing dynamic data [109].

One of the first study that attempted to infer MC from dynamic PET data was the preclinical study conducted by Wehrl et al. (2013) in 8 rats, that compared functional connectivity information derived from BOLD-fMRI and dynamic PET using [^{18}F]FDG tracer through independent component analysis. Their innovative approach unveiled seven brain networks within dynamic PET data, mirroring those described in fMRI literature but on a smaller scale and demonstrating that fundamental information about brain networks is encoded in dynamic PET data, although it is not fully exploited by conventional analysis methods [110].

Only few studies have attempted to derive *individual-level* MC from PET time-activity curves (TACs), also termed *within-individual* MC (wi-MC), because it presents challenges due to strong collinearity among TACs, making simple correlation analysis ineffective. Standardization or detrending of TACs is often employed but may remove biologically relevant variability, particularly in bolus injection studies.

Addressing these challenges, the study of Volpi et al. (2022) utilized a large dataset of healthy adults undergoing bolus dynamic PET studies to establish a comprehensive framework for [^{18}F]FDG PET connectivity. Different TAC standardization strategies and similarity metrics were compared to derive wi-MC matrices, characterizing networks related to delivery and metabolism. Additionally, [^{18}F]FDG kinetic modelling was employed to obtain ai-MC matrices, utilizing parameters describing glucose kinetics (i.e. K_1, k_3 and K_i). The study derived five different wi-MC matrices from various segments of TACs: full (0-60 min), early (0-10 min) and late (40-60 min) TAC segments and the time-varying intracellular concentrations of [^{18}F]FDG ($C_1(t)$) and [^{18}F]FDG-6P ($C_2(t)$) to characterize networks related to inflow, delivery and metabolic exchanges of [^{18}F]FDG separately. The entire pipeline is shown in Figure 1.13.

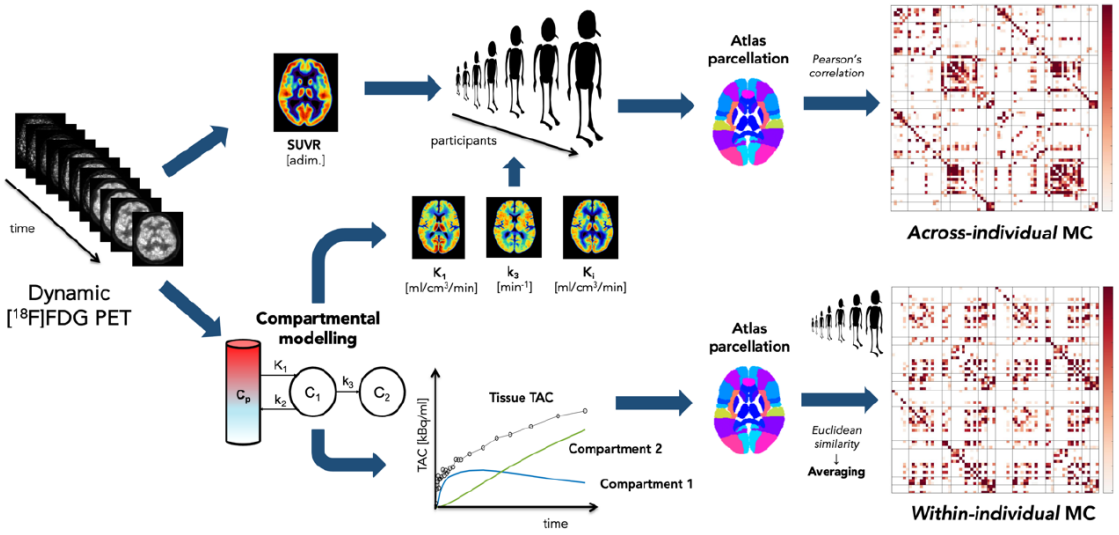

Figure 1.13: *Pipeline for inferring metabolic connectivity matrices both at individual and group levels. From the dynamic data, a static SUVR image is extracted, and compartmental modelling estimates [^{18}F]FDG kinetic parameters. For across-individual connectivity, Pearson's correlation is applied to SUVR and kinetic parameters. For within-individual connectivity, tissue time-activity curves and compartment time courses are processed via Euclidean similarity, averaged across participants* [108].

Notably, the late TAC and metabolized intracellular tracer concentration matrices exhibited good overlap, suggesting non-redundant information provided by kinetic modelling for individual-level MC calculation. In this way, the approach addressed limitations of using raw tissue TAC alone. Studie's results demonstrated the feasibility of obtaining individual-level MC matrices using PET TACs and the *Euclidean similarity* metric (ES), showing both within-network and homotopic connections, with low between-individual variability. These findings verified the robustness of the approach, confirming the hallmarks of brain connectivity studies: small-world, strongly homotopic network structure [108].

Clinical relevance of [^{18}F]FDG-PET

FDG-PET neuroimaging offers valuable metabolic information, shedding light on the mechanisms underlying neurological diseases and guiding therapeutic interventions. In fact, decreases in glucose metabolism are associated with various neurodegenerative conditions. Studies involving patients with Alzheimer's disease and Parkinson's disease have revealed alterations in regional metabolic ratios compared to healthy individuals. PET enables non-invasive examination of physiological processes and has been instrumental in cancer detection, leveraging molecular and biochemical processes within tumour tissues. The first attempt to visualize brain tumour with PET was published in

1953 by Brownell and Sweet. Increased glycolysis is one of the most distinctive biochemical features of malignant cells because of the inefficient metabolism of glucose in malignant tumours. It results from the amplification of the glucose transporter proteins at the tumour cell surface as well as from increased activity of various key enzymes, including hexokinase. Like glucose, [^{18}F]FDG is transported into cells by a glucose transporter protein and rapidly converted into [^{18}F]FDG -6-phosphate. As the latter is not a substrate for glucose-6-phosphate isomerase, it is biochemically trapped in metabolizing tissues. Thus, [^{18}F]FDG PET has been used for cancer screening, differential diagnosis, staging, and treatment evaluation [111].

Over the years, these capabilities have been widely applied to the study of cerebral gliomas, to evaluate metabolic and hemodynamic parameters in these lesions. A landmark study by Di Chiro et al. in 1982 was the first to employ [^{18}F]FDG PET in gliomas, aiming to evaluate the accumulation of [^{18}F]FDG in brain tumour tissues and investigate its correlation with tumour malignancy. This seminal research demonstrated the potential utility of [^{18}F]FDG-PET in analysing brain tumours, setting the stage for further investigations in the field [112]. In 1987, Tyler et al. conducted a pivotal study using PET imaging on 16 patients with untreated cerebral gliomas ranging from grade II to IV. Their research focused on measuring cerebral glucose and oxygen metabolism, oxygen extraction, blood flow, and blood volume within tumour tissues. Results revealed increased blood volume but decreased oxygen extraction and metabolism in tumour tissue compared to homologous grey matter regions. Interestingly, higher-grade tumours exhibited higher blood volumes but lower relative oxygen extraction and utilization. Glucose utilization rates within tumours varied and did not correlate with tumour size or grade. Moreover, parietal tumours tended to exhibit higher relative glucose utilization and blood flow, along with lower relative oxygen extraction, compared to frontal tumours [113].

Kimura et al. (2009) conducted a study to differentiate between high-grade glioma and CNS lymphoma using PET imaging of glucose metabolism. They employed a three-compartment model and found that CNS lymphoma exhibited significantly higher values of k_3 and cerebral metabolic rate of glucose compared to gliomas of grades III and IV. These findings suggest that kinetic analysis of glucose metabolism could be useful for distinguishing CNS lymphoma from high-grade glioma [114].

Further investigations have aimed to differentiate among common brain tumours using FDG-PET, highlighting the metabolic differences between low-grade and high-grade gliomas, as well as the role of glucose uptake in tumour proliferation and necrosis. Das et al. (2011) observed that visual grading of FDG uptake on PET images could statistically distinguish hypometabolic low-grade gliomas (LGGs) from hypermetabolic high-grade gliomas (HGGs). This difference in FDG uptake is generally attributed to the increased glycolytic rate in rapidly growing brain tumour cells. The study also highlighted an inverse statistical correlation between deoxyglucose trapping by the tumour and the length of survival. Additionally, it was found that glucose uptake is higher in glioblastoma compared to anaplastic astrocytoma, which could be explained by the presence of necrosis. Pre-necrotic cells were shown to be hypermetabolic, likely due to the activation of anaerobic glycolytic pathways with increased glucose uptake. The findings suggest a potential relationship between the proliferation index and metabolic grade in glioblastoma, which contributes to the predictive value of FDG-PET in these tumours. However, extremely necrotic tumours may exhibit paradoxically low FDG uptake, which could slightly reduce this predictive value [111].

Pourdehnad and colleagues (2011) conducted a study revealing a correlation between hypometabolism observed in cortical and subcortical grey matter on [^{18}F]FDG-PET imaging in brain tumours and associated oedema demonstrated by magnetic resonance imaging. They found that oedema was linked to significant hypometabolism in adjacent structures, suggesting its role in assessing disease activity and loss of cerebral function. The extent of oedema correlated strongly with the severity of hypometabolism, indicating its significant contribution to cortical and subcortical grey matter hypometabolism in brain tumour patients [115]. In 2019, Li et al. conducted a study leveraging [^{18}F]FD-PET to investigate alterations in tumour microenvironment glucose metabolism, known as the oncological Warburg effect. Their findings validated the use of radiomic analysis of PET images to detect metabolic variances among gliomas with different IDH (Isocitrate Dehydrogenase) genotypes, a crucial biomarker for glioma prognosis and prediction according to the WHO diagnostic criteria. This suggested the potential for non-invasive identification of IDH genotypes in glioma patients using [^{18}F]FDG -PET imaging [116]. Recent research by Pronin and colleagues (2021) found that high-grade gliomas exhibit increased glucose consumption, ATP release, and accelerated cell membrane synthesis.

These metabolic activities suggest heightened energy metabolism and enhanced proliferation of tumour cells, indicative of aggressive tumour behaviour [117].
Overall, FDG-PET imaging plays a crucial role in understanding the metabolic aspects of cerebral gliomas, offering valuable information for diagnosis, prognosis, and treatment planning. Thus, integrating PET connectivity analysis into connectomics studies could offer a comprehensive understanding of brain function by incorporating metabolic data alongside structural and functional connectivity information.

1.3 Coupling between brain metabolism and function

1.3.1 State of art

The coupling between brain metabolism and function represents a critical aspect of neural activity regulation, with implications for cognitive processes and overall brain health. However, the mechanism underlying this linkage is still under investigation due to its complex and multidisciplinary nature. Over the years, several studies have attempted to show that neuronal brain metabolism is correlated with resting state function, increasing interest in exploring this relationship by combining [^{18}F]FDG-PET and rs-fMRI data. Tomasi et al. (2013) proposed a model to assess the energy demands associated with brain connectivity and tested it using PET and MRI in 54 healthy volunteers at rest. The study found significant correlations between *CMRGlu* and functional connectivity measures such as resting-state functional MRI amplitude, as well as local and global degree across subjects. They observed that the correlation between whole-brain *CMRGlu* and local degree explained 18% of the variability in global *CMRGlu*, suggesting that differences in *CMRGlu* between subjects partially reflect differences in their degree of local functional connectivity. Their results indicated a linear association between baseline measures of absolute glucose metabolism and the amplitude of low-frequency MRI signal fluctuations, with regions characterized by higher metabolism showing larger signal fluctuations. Moreover, increases in local and global connectivity degree were associated with power law increases in *CMRGlu* across voxels, supporting the hypothesis of an association between increased *CMRGlu* and synaptic density across brain regions. The study also highlighted differences in metabolic demands between brain regions, with the cerebral cortex exhibiting greater demands compared to the cerebellum. These findings were consistent with varying levels of aerobic glycolysis between these regions, higher in the cortex than in the cerebellum. Additionally, they estimated that basal metabolism,

in the absence of connectivity, accounted for 30% of whole-brain *CMRGlu*, suggesting that spontaneous brain activity contributes significantly to the brain's energy consumption. The study concluded that energy-efficient networks support fast communication at low energy costs, with certain brain regions demonstrating higher glucose metabolism to support their higher communication rates. However, these functional hubs may be particularly vulnerable to conditions that disrupt their energy supply, such as aging or neurodegenerative diseases like Alzheimer's [118]. The study conducted by Aiello et al. (2015) is considered one of the first to directly correlate resting-state regional glucose uptake measured by FDG-PET with brain activity measured by rs-fMRI in healthy subjects, taking advantage of simultaneous PET/MR imaging. They compared the glucose uptake distribution (*rGU*) provided by FDG-PET to three metrics extracted from fMRI data, such as regional homogeneity (*ReHo*), fractional amplitude of low frequency fluctuations (*fALFF*), and degree of centrality (DC) maps, examining their similarity in terms of spatial distribution across the brain and the entire group, as well as voxel-wise across subjects. Additionally, the researchers considered partial volume effects by adjusting for grey matter volume. The researchers found a significant correlation between the spatial distribution of glucose uptake and the fMRI-derived metrics, although only a limited percentage of grey matter voxels correlated with PET across subjects. The strength of correlation varied across functional networks and anatomical regions, with the default-mode network exhibiting the strongest correlation. *ReHo* and *fALFF* showed significantly higher correlation coefficients with PET compared to DC, suggesting that they may provide partly independent and potentially complementary information. Furthermore, the study revealed a heterogeneous pattern of correlations between PET and fMRI-derived metrics across functional networks and anatomical regions. Partial volume effects were considered and found to introduce a limited overestimation of correlation coefficients [119]. One of the main limitations of both citated studies is that they rely on a direct correlation index, which may not fully capture the intricate and potentially nonlinear interactions involved in the relationship between brain function and metabolism.

In their 2017 study, Tomasi and colleagues investigated *CMRGlu*, temporal metabolic connectivity (t-MC), and rs-fMRI patterns in 53 healthy participants. For the first time, they observed that the strength of t-MC increased linearly with the metabolic rate of

glucose, indicating a strong association between t-MC measures and the brain's energy demand. They found that while 22 independent networks emerged from rs-fMRI time series, only two anti-correlated networks emerged from time-varying relative metabolic activity. These findings suggested that t-MC networks were driven by regional differences in FDG pharmacokinetics rather than functional interactions between remote brain regions. The study also highlighted differences in tissue composition and metabolic rates between the cerebellum and cerebral cortex, potentially influencing the observed anti-correlated t-MC patterns. Additionally, the temporal resolution of t-MC and t-FC differed due to variations in FDG pharmacokinetics and neurovascular coupling. Overall, the study identified distinct patterns for t-MC compared to traditional functional connectivity measures, likely reflecting different temporal dynamics and metabolic costs associated with neuronal activity [120].

One of the first studies that utilized high-temporal resolution simultaneous BOLD-fMRI and [FDG]-PET acquisition to measure subject-level metabolic connectivity alongside fMRI connectivity is that of Jamadar et al. (2021). Their findings revealed distinct patterns of metabolic connectivity characterized by frontoparietal connectivity both within and between hemispheres. Interestingly, they observed that fPET metabolic connectivity exhibited moderate similarity with fMRI connectivity, particularly in regions of the superior cortex and frontoparietal areas. This suggested a partial overlap between the two modalities in capturing functional connectivity patterns, highlighting the complementary nature of fPET and fMRI in understanding brain connectivity [121]. Palombit et al. (2022) used a hybrid PET/MR system to simultaneously measure glucose metabolism with [^{18}F]FDG-PET and resting-state functional connectivity organization with fMRI. One of the key findings of the study was the strong correlation between the strength of fMRI functional connections and glucose metabolism in the central regions of the brain, also known as hubs. While the correlation between glucose metabolism (measured as *SUVR*) and FC strength at the whole-brain parcel level was moderate, it increased linearly in the top connected regions. Connector hubs, which primarily connect with regions of different networks, were found to be metabolically more expensive than provincial hubs, which primarily connect within the same network, suggesting that integration between different networks has a clearer and more linear impact on energy metabolism. The authors discussed various factors that might contribute to the observed

relationship between glucose metabolism and FC strength, including synaptic activity, blood flow, structural connectivity, local activity, and inter-regional synchronization. Furthermore, the study emphasized that between-network connections are more strongly related to glucose metabolism than within-network connections. This may reflect weaker homeostatic plasticity or stronger levels of activity for infrequent between-network interactions, which are more commonly observed during tasks or novel situations [122]. Voigt et al. (2022), in their simultaneous resting-state FDG-PET/fMRI study, correlated the connectivity patterns of both modalities with various cognitive functions. Although both fPET metabolic and BOLD-fMRI hemodynamic connectivity were strongest in frontoparietal cortices, they were associated with different cognitive functions. Resting-state hemodynamic connectivity was associated with inhibition, depression, and memory retention, whereas resting-state metabolic connectivity was associated with executive function and inhibition, and negatively correlated with executive functioning and verbal fluency. The study revealed that cognition is supported by domain-general hemodynamic and metabolic processing, with metabolic processes more spatially defined by frontoparietal areas, while hemodynamic processes across multiple brain regions collectively support cognition. The results suggest that flexible, domain-general interactions allow for rapid integration and exchange of diverse information across cognitive states [123].

In another recent study, Hansen and colleagues (2022) integrated seven different forms of brain connectivity, including gene expression, receptor density, cellular composition, metabolic consumption, haemodynamic activity, electrophysiology, and timeseries features, across diverse spatial scales and imaging modalities. The study confirmed that brain regions which are homologous, spatially close, and structurally connected tend to display similarity, underscoring the significance of geometry and structure in inter-regional relationships. However, these modes are not redundant and exhibit poor correlation among each other, principally differing in gradients and modular structures and impacting the identification of brain hubs. The identified cross-modal hubs in association regions are mainly involved in high-level cognition, suggesting integration across multiple biological scales. In particular, the study revealed that metabolic connectivity is increased in rich club regions, indicating synchronized energy consumption among densely interconnected brain areas, and thus demonstrating that both

hemodynamic and metabolic connectivity play crucial roles in shaping brain function and organization [124].

1.3.2 Methodological approaches for multimodal imaging

All the mentioned studies used different imaging modalities on the same individuals to facilitate an understanding of the nature of structure, behaviour, and cerebral activity in a more comprehensive way. However, despite these benefits, multimodal imaging is quite challenging, and this is possibly due to the lack of gold-standard multimodal image analysis methodologies. In fact, even though the majority of researchers have had access to multimodal data sets, they have analysed each modality separately. Still, few researchers have used multimodal imaging to tackle cognitive questions that are not addressable using unimodal imaging. One simple data integration approach involves calculating the correlation between specific regions of interest in two different modalities (Hasnain et al.,2001) or overlaying statistical maps generated from different modalities, known as conjunction analysis, to identify areas of shared activation and make group-level inferences (Friston et al.,1999). However, this method doesn't involve voxel-wise regression analysis between the modalities. An alternative to integration or conjunction analysis is data fusion, where both modalities are analysed together in a single joint analysis. This is the field of multivariate approaches, such as Fusion ICA, that offer a more comprehensive examination by transforming data matrices into components and analysing across all brain regions (McIntosh et al., 1996; McKeown et al., 1998).

Here's an overview of the most common used integration methods and fusion techniques for analysing multimodal data sets:

- ROI analysis has been used to identify correlations between metabolic and functional measures in localized brain regions (Madden et al., 2007; Persson et al., 2006). However, this analysis lacks a standardized method for selecting regions, and variations in ROI size and definition can affect correlation results, potentially missing global patterns and interactions between brain regions (Barrick et al., 2010; Stevens et al., 2009).
- Voxel-wise fusion, alternatively, analyses statistical maps from different modalities without predefined regions, allowing for voxel-wise regression or correlation between modalities. But in can be still challenging due to individual differences in brain anatomy.

- Univariate approaches like Bivariate Probabilistic Mapping (BPM) are suitable for voxel-wise integration but are limited in capturing the full extent of brain connectivity changes across modalities (Casanova et al., 2007).
- Joint-ICA (jICA) is a multivariate technique that simultaneously decomposes multiple data type into spatially independent components, with the assumption of a common linear mixture between modalities, allowing for the identification of shared patterns among all voxels in both modalities (Calhoun et al., 2009). However, interpretation of these components can be challenging, and the method may not capture subtle interactions between modalities. In fact, a suggested strategy is to combine jICA with a general linear model framework to facilitate interpretation.
- Canonical Correlation Analysis (CCA) is a method used to identify a transformed coordinate system that maximizes the covariation between two datasets, allowing for different mixing matrices for each modality. Unlike jICA, this multivariate method offers flexibility by allowing both common and distinct levels of connection between features. However, CCA may result in less spatially sparse source maps, particularly when canonical correlation coefficients (CCCs) are not distinct enough and it may not fully capture nonlinear relationships (Correa et al.,2008).
- Partial Least Squares (PLS) is another multivariate approach that decomposes covariance matrices, incorporating task or behavioural information to determine brain activation patterns. PLS assesses activation changes across all brain regions simultaneously, without the need for multiple comparisons correction (Lin et al.,2003). However, the interpretation of PLS results can be complex, and the method may be sensitive to noise and data preprocessing choices (McIntosh et al.,2004).

Multivariate approaches for combining brain imaging data can be categorized into two main classes: hypotheses-driven and data-driven methods. Hypotheses-driven approaches, such as multiple linear regression and confirmatory structural equation modelling, offer the advantage of allowing researchers to test specific hypotheses regarding brain networks implicated in the experimental paradigm. Additionally, they enable simultaneous assessment of multiple connectivity links, which might be

compromised by individually assessing covariance. However, these approaches may overlook important connectivity links not included in the initial hypotheses and do not provide insights into inter-voxel relationships. On the other hand, data-driven approaches, including PCA, ICA, and canonical correlation analysis (CCA), do not require predefined hypotheses about connections of interest. Thus, they are well-suited for exploring the entire dataset comprehensively. However, some of these methods may be computationally demanding.

Among all the aforementioned methods, partial least squares stand out as a hybrid approach that combines elements of both hypotheses-driven and data-driven analysis. PLS incorporates both predefined hypotheses and data exploration, offering a flexible framework for analysing multimodal data [125].

The following sections of this chapter focus on the detailed description of the PLS method, since it was chosen as the research approach in this thesis due to its great potential in the field of multivariate analysis.

1.3.3 Partial Least Squares (PLS) analysis

PLS analysis, by integrating task or behavioural information early on, reveals the brain's time-varying distributed patterns in relation to tasks or behaviours. Unlike voxel-by-voxel approaches, PLS evaluates activation changes across all brain regions simultaneously, eliminating the need for multiple comparisons correction. Moreover, PLS considers both differences and similarities, offering a broader examination of neural activation patterns across various cognitive processes, contrasting with traditional univariate analyses focused solely on task differences.

In the analysis of neuroimaging data, two main types of PLS methods have been employed: PLS correlation (PLSC) and PLS regression (PLSR). PLSC, introduced by McIntosh et al. (2004), is a technique that examines the association between two sets of data, such as brain activity and experimental design or behaviour [126]. On the other hand, PLSR as proposed by Abdi (2010), is a method used to predict dependent variables, like behaviour, based on independent variables, such as brain activity [127]. Although PLS regression is relevant to the PLS family, it was not utilized in this thesis and will not be further discussed here. The following description of PLSC is based on that given in Krishnan et al. (2011) [128].

PLS correlation can be further categorized into four variations: task PLS, behavioural PLS, seed PLS, and multi-block PLS. The key distinction among these variations lies in the definition of the matrix (Y) that is cross correlated with brain activity (X). In task and behavioural PLS, Y represents experimental and behavioural variables, respectively. In seed PLS, Y corresponds to voxel activity from specific ROIs. In multi-block PLS, the Y matrix comprises a multi-table format, encompassing behavioural variables, experimental variables, and/or voxel activity from ROIs.

Data organization

In PLSC analysis, the association between brain activity and various factors like experimental design, behaviour, or voxel activity from ROIs is examined. Brain activity is represented in an I-by-J matrix labelled X, where rows represent observations (e.g., subjects within conditions within groups) and columns represent variables (e.g., voxel intensity for all time points). Behavioural data, experimental design, or voxel activity from ROIs are organized in an I-by-K matrix denoted Y, where rows indicate observations and columns represent different behavioural measures, voxel activity from ROIs, or contrasts reflecting different aspects of the experimental design. Both X and Y matrices undergo z-scoring to standardize the variables, ensuring that the mean of each column is zero and the standard deviation is one. This standardization enables comparability between variables in the two matrices. The relationship between the two matrices is quantified by calculating the dot product of the columns of X and Y, given by:

$$R = Y^T X$$

where the matrix Y is transposed (^{T}). R is a K-by-J cross-product matrix that represents the correlation between the normalized (e.g., z-scored) columns of the X and Y matrices, indicating the correlation between brain activity and experimental design. If the columns of the matrices are only centred but not normalized, the R matrix reflects covariance.

Derivation of Latent Variables

The cross-product matrix, R, undergoes singular value decomposition (SVD) [129], [130], which is the fundamental tool in PLS analysis. This process decomposes the J-by-K cross-product matrix R^T into three matrices as follows:

$$[USV] = SVD[R^T]$$

Where:

$$U * S * V^T = R$$

The singular value decomposition yields a set of mutually orthogonal latent variables (LVs), with U (K-by-L) and V (J-by-L) being orthogonal matrices containing left and right singular vectors, respectively, and S (L-by-L) being a diagonal matrix of singular values. The number L of latent variables equals the rank of the covariance matrix R, which is the smaller of its dimensions. Each latent variable is associated with:

1. a singular value (found on the diagonal of S) indicating how much of the cross-block covariance (R) is explained by that latent variable;
2. a vector of singular values V, representing the imaging saliences;
3. a vector of singular values U, representing the behavioural saliences.

The first and subsequent LVs account for the greatest and progressively decreasing amounts of the cross-covariance matrix (indicated by the square of the singular value), respectively. The imaging saliences indicate how strongly each connection contributes to the imaging-design correlation explained by a given latent variable. Similarly, the behavioural saliences signify the strength of each cognitive variable's contribution to the imaging-design correlation explained by a specific latent variable.

Projecting (using the dot product) each subject's original imaging data (in X) onto the multivariate imaging salience pattern (in V) yields imaging scores:

$$L_X = X * V$$

L_x is a I-by-L matrix measuring the similarity of an individual's imaging data with the salient imaging pattern. Likewise, design (or behavioural) scores can be computed as follows:

$$L_Y = Y * U$$

Where L_y is a I-by-L matrix representing the projection of each subject's design variable onto the respective design saliences. Finally, imaging and behavioural structure coefficients (or "loadings", [131]) can also be obtained by computing Pearson's correlations between the original data (X and Y) and subject-specific scores (L_x, L_y). Loadings indicate the extent of contribution of each variable to the latent variable derived from the PLS analysis.

In summary, PLS utilizes latent variables to capture the most significant shared information between imaging data and experimental design (or behavioural variables) by maximizing covariance.

A diagram outlining the various steps of PLS analysis is reported in Figure 1.14. This flowchart is taken from the documentation of the MATLAB toolbox (myPLS) that implements the PLSC, created by Zoller and colleagues (all the documentation available on GitHub), which was used in this thesis project [132].

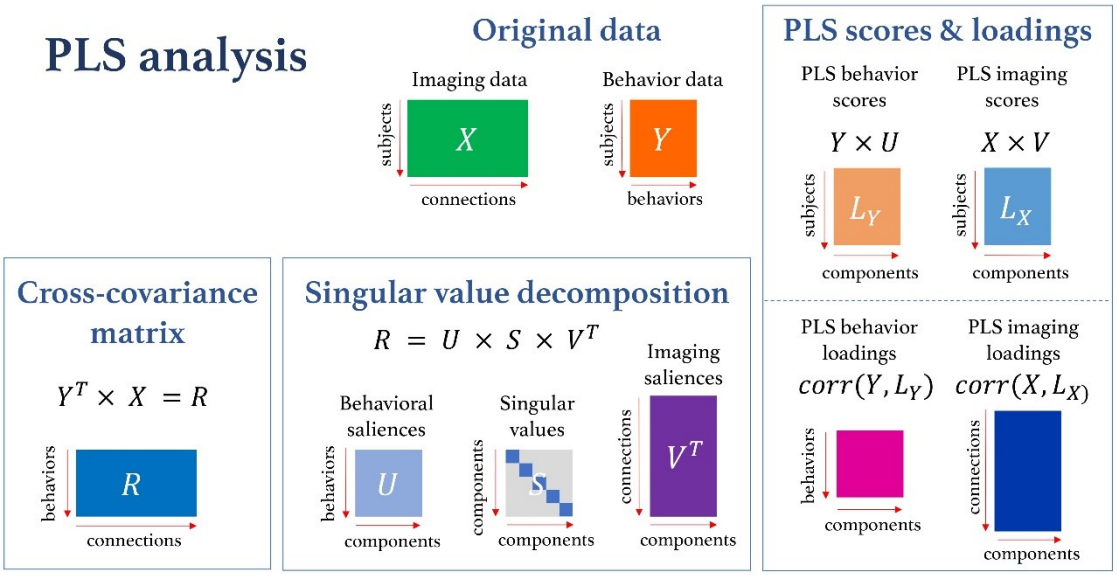

Figure 1.14: *A schema illustrating the procedure of PLSC analysis. From the original data in X and Y matrices, the cross-covariance matrix is obtained and SVD-decomposed into singular vectors (U and V) and singular values (S). The right panel indicates the procedure of creating imaging and behaviour scores (up) and then imaging and behaviour loadings, i.e. weights of each variable in the current LV (down)* [132].

Assessment of significance

PLS addresses the significance of an image (or voxel) by splitting it into two distinct questions. Firstly, it assesses the significance of the overall pattern reflected in each LV, which indicates cooperative interactions among brain regions. This allows determining whether the pattern in each LV significantly deviates from randomness or noise. From another perspective, an inferential analytic approach is required to generalize the fixed effect model, yielded by SVD, to the population (i.e. the random effect model). Secondly, PLS evaluates the stability of any potential localization contributing to the overall pattern, indicating the reliability of the regions involved. To address these questions, permutation

and bootstrap tests have been proposed to assess the significance of the overall pattern and the stability of the contributive saliences, respectively [126], [133].

The determination of the number of latent variables to retain in PLS analysis has been addressed by employing nonparametric permutation tests. These tests evaluate whether the overall pattern within each LV is statistically robust enough to distinguish it from randomness or noise. This is achieved by randomly permuting the order of conditions within the data matrix (X) while keeping the experimental design (behavioural or ROI signal changes) matrix Y unchanged. Subsequently, the LVs are computed for the permuted samples using the same SVD algorithm, typically repeated a certain number of times (e.g., 500 or 1000 permutations). The probability of significance for the original LVs is then determined based on how often the permuted singular value exceeds the original one. Since the null hypothesis is tested for each LV as a whole (i.e., whether the entire LV was generated by randomness), there is no need for multiple comparison correction.

To assess the stability of voxel saliences contributing to each latent variable, the standard error of saliences is estimated using bootstrap sampling [134]. This involves resampling with replacement of observations in both the X and Y matrices while keeping the assignment of experimental conditions fixed. The Bootstrap Ratio (BSR), which represents the ratio of voxel saliences to estimated error, is then computed for each voxel. Analogous to a z-score, a voxel with a BSR exceeding a certain threshold (e.g., BSR > 3.2, corresponding to $p < 0.001$) is deemed significantly stable and reliably contributes to the pattern. Notably, the aim of computing the bootstrap ratio is to identify voxels whose responses consistently reflect the effect in each LV, eliminating the need for multiple comparisons since no statistical test is conducted. Furthermore, the bootstrap estimate is utilized to establish confidence intervals for imaging scores in task PLS and for correlations in behavioural PLS, enhancing the reliability of interpretation.

Caveats in PLS

Despite the unique and distinctive features of partial least squares in combining the strengths of data-driven and hypothesis-driven analyses, there are some caveats to its use. Firstly, PLS analysis of average-sized neuroimaging data can be computationally expensive, with a regular number of permutation and bootstrap tests taking at least 30-45 minutes on a standard workstation. Secondly, PLS utilizes the SVD method to extract

mutually orthogonal patterns, which may fail to capture the true dependencies between patterns due to its orthogonality constraint [126]. An alternative solution could be replacing SVD with an algorithm like ICA, which achieves independence without imposing orthogonality, although ICA may be less sensitive and robust in extracting reliable signals [135]. Thirdly, extracted patterns from SVD may be nonlinear or difficult to interpret, making it challenging for LVs to align with a priori expectations. In such cases, using a non-rotated version of PLS (contrast PLS) is recommended to aid interpretation. Finally, PLS is not well-suited for fast event-related designs.

PLSC applications with multimodal neuroimaging data

PLS was initially introduced to PET in 1996 by McIntosh and colleagues. Its application was further extended to complex fMRI designs in 2004 by the same researchers [126], [133]. Since then, PLS has been extensively utilized in various neuroimaging datasets, including fMRI, structural MRI, PET, ERP (Event-Related Potential), and MEG (Magnetoencephalography), across different paradigms such as event-related designs and block designs. Below, are provided some examples of different applications of the same PLSC toolbox used in this project, applied principally to fMRI data, addressing a wide range of cognitive questions.

- Zoller et al. (2019) demonstrated that behaviour PLSC with brain network-based measures was able to show coactivation patterns for dynamic large-scale brain network analysis, uncovering patterns of brain network activation duration and coupling that are relevant in clinical risk factors for psychosis in *22q11* deletion syndrome [136].
- Kebets et al. (2019), using behaviour PLSC with connectivity measures and different grouping in PLSC and resampling, identified three robust distinct dimensions with dissociable (but overlapping) whole-brain resting-state functional connectivity signatures across healthy individuals and individuals with psychiatric illness [137].
- Zoller and colleagues, in their works of 2017 and 2018, used contrast PLSC for multivariate analysis of group differences and developmental effects. This method was able to confirm the strong implication of BOLD variance in (i) aging, giving an initial insight in its relationship with functional connectivity in the DMN and

(ii) psychotic symptoms, suggesting aberrant BOLD signal variability development as a potential biomarker for psychosis [138], [139].

In the aforementioned study of Voigt et al. (2022), researchers separately applied partial least squares correlation to connectivity matrices derived from fMRI (hemodynamic connectivity) and PET (metabolic connectivity) data in relation to cognitive outcome variables from a neuropsychological test battery, to assess differences between the two modalities with respect to cognition. PLSC analyses conducted on the fMRI and fPET data sets separately identified a significant latent variable describing the relationship between hemodynamic connectivity and cognition and another significant latent variable describing the relationship between metabolic connectivity and cognition. In addition, a separate PLSC analysis was performed by concatenating the fMRI and fPET matrices prior to single value decomposition. This latter analysis was one of the first applications of PLSC to assess the similarity of fMRI and fPET connectivity in relation to cognition [123]. Overall, as highlighted by the cited studies in the literature, PLSC has traditionally been applied between variables related to brain activity and design (or behavioural) variables. This raised the curiosity to apply this multivariate analysis method to data sets that are both related to brain activity but reflect two different and complementary aspects (fMRI and PET). Given the characteristics of the PLSC approach and its ability to find co-variation patterns between two data sets obtained with different techniques and considering the validity of the cited toolbox in recognizing these patterns significantly, the decision was made to use the PLSC toolbox implemented by Zoller et al. in the present thesis work. Therefore, the goal was to detect similarities and differences in the contribution of each brain region to the common co-variation pattern between the two modalities of brain data, functional and metabolic.

Chapter 2

Materials and methods

In this chapter, the fMRI and [^{18}F]FDG-PET data used for in the study are presented, along with an overview of their acquisition and collection protocols and the pre-processing techniques used to prepare the data for analysis. Subsequently, the methods used to estimate functional brain connectivity and its strength, brain metabolic parameters, and connectivity matrices are described. Then, the statistical analysis with PLSC multimodal integration of fMRI and [^{18}F]FDG-PET derived metrics, is explained in detail, for both healthy participants and patients.

2.1 Participants

In this study, 42 healthy adults (mean age 58.2±14.5 years, 23 females/19 males) were recruited as the control group. These individuals were participants in the Adult Metabolism & Brain Resilience (AMBR) study [140]. The study adhered to the principles outlined in the Declaration of Helsinki. Approval for all assessments and imaging procedures was obtained from the Human Research Protection Office and the Radioactive Drug Research Committee at Washington University in St. Louis. Written consent was obtained from each participant. Exclusion criteria for participants included contraindications to MRI, history of mental illness, potential pregnancy, or medication use that could affect brain function.

Conversely, presurgical data from 43 patients (mean age 58.9 ± 14.7 years, 20 females/23 males) with de novo brain tumours were collected at the University Hospital of Padua and included in the patient cohort. Diagnosis was based on the WHO classification system (2016 version). Details regarding the patient's demographics and clinical information are summarized in Table 2.1. Inclusion criteria for patients were: (1) de novo glioma (excluding recurrences), (2) age 18 years or older, (3) absence of other neurological or psychiatric disorders, and (4) availability of presurgical PET and MRI acquisitions, including pre- and post-contrast T1-weighted (T1w) sequences, T2-weighted (T2w), fluid attenuation inversion recovery (FLAIR), and rs-fMRI. All participants received regular anticonvulsants for seizure control and corticosteroids. The protocol was approved by the

local Ethics Committee of the University Hospital of Padua and conducted in accordance with the 1964 Declaration of Helsinki and its subsequent amendments. All participants provided informed, written consent in accordance with the local University Hospital Institutional Review Board.

Demographical and clinical characteristics	Controls (n=42)	Patients (n=43)
Gender		
Female	23	20
Male	19	23
Age	58.2 ± 14.5	58.9 ± 14.7
Tumour Histology		
Astrocytoma	-	2
Glioblastoma	-	28
Glioneuronal and neuronal tumours	-	3
Oligodendroglioma	-	1
Primary diffuse large B-cell lymphoma of the CNS	-	1
Others	-	8
Tumour grade		
Low	-	6
High	-	33
n.a.	-	4
IDHI mutation status		
Wild-type	-	26
Mutated	-	5
n.a.	-	12
Tumour site		
Left	-	21
Right	-	17
Bilateral	-	4
n.a.	-	1

Table 2.1: *Demographical and clinical details of the 42 healthy subjects and 43 glioma patients considered in this thesis.*

2.2 Data acquisition and collection

2.2.1 MRI data

Healthy controls

High-resolution structural MRI images were captured using a Siemens Magnetom Prismafit scanner, employing a 3D sagittal T1w magnetization-prepared 180° radio-frequency pulses and rapid gradient-echo (MPRAGE) multi-echo sequence. The parameters for the sequence were TE (echo time) = 1.81, 3.6, 5.39, 7.18 ms, TR (repetition time) = 2500 ms, TI (inversion time) = 1000 ms, with voxel dimensions of 0.8 × 0.8 × 0.8 mm. The final T1w image was obtained by averaging the first two echoes (Elam 2021). Additionally, T2*w gradient-echo echo planar imaging (GE-EPI) data were acquired on the same scanner, with parameters TR/TE (repetition time/echo time) = 800/33 ms, flip angle (FA) = 52°, voxel size = 2.4 × 2.4 × 2.4 mm, multi-band acceleration factor (MBAccFactor) = 6, and a total of 375 volumes acquired over 5 minutes. Two spin-echo (SE) acquisitions were also performed with parameters TR/TE = 6000/60 ms, FA = 90°, and opposite phase encoding directions (AP, PA).

Patients

Glioma patients underwent combined PET/MR scans using a Siemens 3T Biograph mMR scanner equipped with a 16-channel head-neck coil. The anatomical imaging included T1w 3D scans with specific parameters: TR of 2400 ms, TE of 3.24 ms, TI of 1000 ms, FA of 8°, field of view (FOV) of 256 × 256 mm^2, voxel size of 1 × 1 × 1 mm^3, acceleration factor iPAT = 2, and acquisition time (TA) of 5:45 minutes. These scans were acquired both before and after the administration of a contrast agent. Additionally, a 3D T2w image and 3D FLAIR image were acquired with specific parameters: TR = 3200 ms and TE = 5.35 ms for T2w, while TR = 5000 ms, TE = 284 ms and TI = 1800 ms for FLAIR (the other parameters FOV = 256 × 256 mm^2, voxel size = 1 × 1 × 1 mm^3, iPAT = 2, and TA = 5:47 minutes were equals for both T2w and FLAIR).

Functional imaging included rs-fMRI scans obtained with a T2*w GE-EPI sequence with TR = 1260 ms, TE = 30 ms, FA = 68°, FOV = 204 × 204 mm^2, voxel size = 3 × 3 × 3 mm^3, iPAT = 0, MBAccFactor = 2, 750 volumes, TA = 16:03 minutes, and phase encoding direction antero-posterior. Additionally, two SE acquisitions with reverse phase encoding were performed for EPI distortion correction purposes, with parameters TR = 4200 ms,

TE = 70 ms, FA = 90°, FOV = 204 × 204 mm², voxel size = 3 × 3 × 3 mm³, and TA = 8.4 seconds.

2.2.2 [^{18}F]FDG-PET data

Healthy controls

[^{18}F]FDG scans were conducted using a Siemens model 962 ECAT EXACT HR + PET scanner (Siemens/CTI), as previously described in (Vaishnavi, 2010) [141], following intravenous bolus injection of 5.1 ± 0.3 mCi (187.7 ± 12.1 MBq) of [^{18}F]FDG. PET emission data were dynamically acquired over a duration of 60 minutes with participants in the eyes-closed waking state. Participant head movements were minimized using a thermoplastic mask. PET data were reconstructed using filtered back-projection (ramp filter, 5 mm FWHM) into 128x128x63 matrices with a voxel size of 2.0x2.0x2.0 mm. Attenuation correction was performed using the participant's transmission scan. The reconstruction grid comprised 52 frames of increasing duration, including 24 frames of 5 seconds, 9 frames of 20 seconds, 10 frames of 1 minute, and 9 frames of 5 minutes.

Patients

Dynamic PET acquisitions lasting 60 minutes were conducted following an intravenous bolus injection of 203 ± 40 MBq. The images were reconstructed into matrices of size 256x256x127 with a voxel size of 2.8x2.8x2.0 mm using the OSEM algorithm from list-mode data. The reconstruction grid consisted of 39 frames with increasing duration: 10 frames of 6 seconds, 8 frames of 15 seconds, 9 frames of 60 seconds, and 12 frames of 240 seconds.

2.3 Data pre-processing

2.3.1 MRI data

For healthy controls (HCs), their structural T1w images underwent several processing steps. Initially, they were corrected for N4 bias field (Tustison 2010), then skull-stripped [142], and segmented into grey matter (GM), white matter (WM), and cerebrospinal fluid (CSF) using SPM12 [143]. Subsequently, these T1w images were aligned to the asymmetric MNI 152 FSL standard space via nonlinear diffeomorphic registration. For patients, their anatomical images were linearly registered to their T1w image using the ANTs tool [144]. An experienced neuroradiologist manually segmented lesions using ITK-SNAP software [145], resulting in two masks, one encompassing tumour core

(enhancing and non-enhancing regions), necrosis, and oedema (lesion masks), while the second one without the oedema (tumour mask). Lesion frequency map (right) and tumour frequency maps (left) are depicted in Figure 2.1. Following lesion segmentation, patient's MRI data underwent structural pre-processing similar to that of healthy controls.

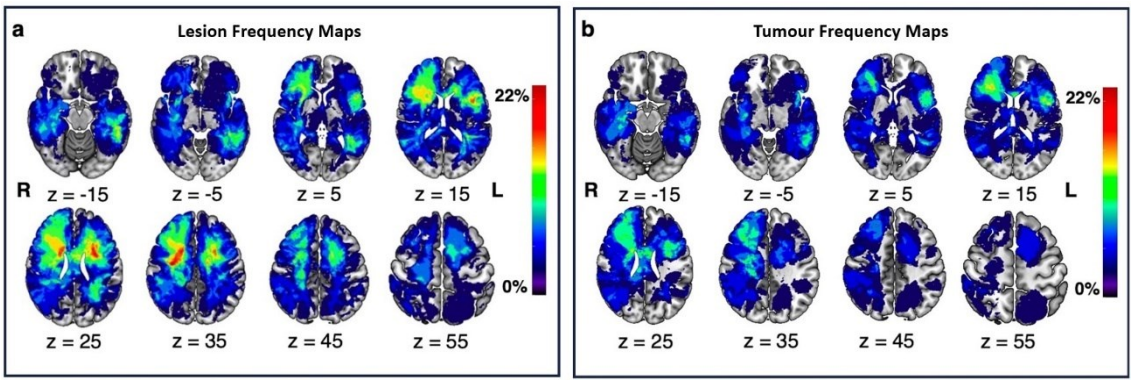

Figure 2.1: *Distribution of glioma topography. Frequency maps of lesions (left panel) and tumours (right panel) in MNI 152 FSL symmetric space for the cohort of 43 patients. The first map includes all lesion areas, while the second focuses solely on the tumour core and necrosis. These frequency maps are generated by overlaying individual binary masks and normalizing by the sample size. Notably, the maps show a sparse distribution, with tumours mainly affecting the right frontal and temporal lobes, exhibiting minimal spatial overlap (up to 19%).*

Regarding functional pre-processing, fMRI data were processed according to the Human Connectome Project minimal pre-processing pipeline [146]. For both healthy controls and patients, the first four fMRI volumes were discarded to mitigate non-equilibrium magnetization effects. Subsequently, the remaining volumes were corrected for slice timing differences [147] and magnetic field distortion (FSL's TOPUP) [148], then realigned to the median volume (FSL's mcflirt) [149]. Motion parameters, their first-order derivatives, and the first five temporal principal components obtained after PCA of WM and CSF EPI signals [150] were regressed out from the rs-fMRI timeseries. Individual EPI scans were nonlinearly aligned to the MNI152 FSL standard space [149], exploiting the subject-specific T1w (via FSL's boundary-based registration) [151]. Residual motion influence on rs-fMRI data was minimized through ICA-based automatic removal of motion artifacts (ICA-AROMA) [152] for HCs and a manual ICA-based approach for patients [153]. Finally, the BOLD signal was high-pass filtered with a cutoff frequency of 0.008 Hz.

Moreover, temporal traces of both HCs and patients were further band-pass filtered, resulting in two distinct frequency bands of the signal:

- the canonical band between 0.008-0.11 Hz (referred as F_1), as used in the literature, representing the largest contribution related to neuronal activity that emerges in the 0.01-0.5 Hz range and in the bands containing this range. These bands have been shown to reflect good spatial agreement in the pattern of hubs and similar modularity values [154].
- the second band between 0.008-0.21 Hz (referred as F_2) was chosen to also retain the range of frequencies that is typically supported by the canonical HRF in the DCM framework (J. E. Chen and Glover, 2015; Henson & Friston, 2007). This portion of the signal starts to be strongly influenced by the presence of slow hemodynamic function information and could more easily account for potential hemodynamic coupling with [^{18}F]FDG metabolism and alterations in oncological patients (see the next section for details).

For both healthy controls and patients, fMRI time courses were projected onto a clustered cortical parcellation of the Yan homotopic functional atlas, maintaining 74 regions [155]. Each parcel is assigned to one of the RSNs described by (Yeo 2011): Visual network (VIS) (5 parcels), Somatomotor network (SOMMOT) (13 parcels), Dorsal attention network (DORSATTN) (9 parcels), Saliency/Ventral attention network (SALVENATTN) (10 parcels), Limbic network (LIMBIC) (5 parcels), Control network (CONT) (13 parcels), and Default mode network (DMN/DEFAULT) (19 parcels) [156]. Additionally, 12 subcortical and cerebellar regions were included based on the Automated Anatomical Labelling (AAL3) segmentation: six regions per hemisphere, consisting of thalamus proper, caudate, putamen, pallidum, hippocampus, and cerebellum.

In both cases, the atlas was aligned to the MNI 152 FSL standard space. For patients, ROIs were delineated by excluding voxels within the lesion mask, as typically done in several studies on gliomas to ensure that possible alterations were not simply due to tumour-associated tissue loss and dysfunction [157], [158], [159]. This exclusion aimed also to remove grey matter areas adjacent to the tumour, where fMRI signal may be affected by pronounced alterations in hemodynamic response and/or neurovascular uncoupling due to tumour angiogenesis [160], [161], [162], [163], leading to attenuations and/or distortions that might not be effectively captured by the hemodynamic response function prior [164].

TACs were then extracted for each of the total 86 defined regions by averaging the voxel activities within the GM SPM mask (probability > 0.8) for cortical voxels and the non-cerebrospinal fluid (notCSF) SPM mask (probability > 0.95) for subcortical and cerebellum voxels. The selected segmentation approach is intentionally conservative, yielding a mean sample TAC that effectively mitigates partial volume effects (PVEs) while still retaining an adequate number of voxels.

Furthermore, each subject was assigned a binary temporal mask to identify brain volumes corrupted by head motion (Framewise Displacement > 0.4 mm). This mask was utilized to adjust the reliability of temporal frames, censoring the data with high-motion frames, and a minimal number of 400 remained volumes after censoring was set to include subject in the study, as in [165].

2.3.2 [^{18}F]FDG-PET data

The dynamic PET scans from both patients and HC groups were corrected for motion using the FSL's mcflirt algorithm [166]. Subsequently, for each patient, a static PET image was created by summing the motion-corrected late PET frames (40 and 60 minutes). This static image was then aligned with T1w space using FSL's flirt algorithm[149]. After, tumour and lesion masks, Hammers, and Yan parcellations, along with individual GM and WM tissue segmentations, were mapped from T1w to PET space. Each of these static PET images was then normalized dividing it by the average uptake of [^{18}F]FDG in the WM SPM map, where the probability of belonging to WM was greater than 0.95, specifically in the cerebellum on the same side as the lesioned hemisphere (as defined by the Hammers atlas), resulting in *SUVR*. The entire cerebellar WM was utilized for bilateral tumours as a reference region due to its low incidence of glioma occurrence (4.5% of all gliomas) and the occurrence of crossed cerebellar diaschisis in glioma patients [167].

Also for the HC group, the static PET image was generated by summing late PET frames (40-60 min) and normalized to *SUVR* by dividing each voxel value by the average uptake of [^{18}F]FDG in the entire brain [168].

In addition, for both healthy controls and patients, a voxel-level quantification of the [^{18}F]FDG-PET data, using the Sokoloff model and a Variational Bayesian inference framework (detailed in chapter 1.2.2), was performed to derive parametric maps of K_1, k_3, K_i. Subsequently, the voxel-wise maps of K_1, k_3, K_i, *SUVR* were mapped onto the

clustered cortical parcellation consisting of 74 cortical ROIs and 12 subcortical and cerebellar ROIs, excluding voxels within the lesion mask for patients.

So, regional values of PET parametric maps were derived for each ROI within the parcellation scheme by averaging voxel activities within the GM SPM mask for cortical voxels and the notCSF SPM mask for subcortical and cerebellum voxels, keeping the same conservative approach used for fMRI TACs to reduce PVEs while ensuring an adequate number of voxels. Furthermore, to minimize PVEs further, PET data underwent processing without additional spatial smoothing.

Then, TACs of [^{18}F]FDG were extracted from dynamic PET images – for each ROI belonging to the parcellation scheme– by averaging the voxel activities within the GM SPM-mask. Additionally, in calculating patient's ROI TACs, voxels within the entire lesion mask were excluded, following a similar rationale as in the computation of regional static PET parameter's values explained above. Regional TACs were then interpolated onto a uniform virtual grid with a one-second step.

2.4 Methods

Data have been inspected and processed using MATLAB R2020b, FSL v6.0 and BrainNet Viewer 1.7. Some packages have been downloaded to extend MATLAB functionalities: "Tools for NIfTI and ANALYZE image" v1.27, SPM12 and myPLS toolbox v1.0 [132].

2.4.1 Within-individual functional connectivity measures

For each subject and patient, the FC matrix was obtained by computing the Pearson's correlation coefficients between the time series of each pair of parcels, along with the corresponding matrix of p-values to assess statistical significance, as:

$$r = \frac{\sum_{i=1}^{T}\left(z_{i,1} - \overline{z_1}\right)\left(z_{i,2} - \overline{z_2}\right)}{\sqrt{\sum_{i=1}^{T}\left(z_{i,1} - \overline{z_1}\right)}\sqrt{\sum_{i=1}^{T}\left(z_{i,2} - \overline{z_2}\right)}}$$

where T is the number of samples, $z_{i,1}$ and $z_{i,2}$ are the individual samples, and $\overline{z_1}$ and $\overline{z_2}$ are the arithmetic sample averages.

Thus, two FC matrices were obtained for each subject and patient, one for each frequency band (0.008-0.11 Hz (F_1), 0.008-0.21 Hz (F_2)).

Before proceeding to the connectivity analysis using graph measures, the group-average FC matrix was derived by averaging all FC matrices from healthy subjects, both within frequency band $F_1$and F_2. Then, both average matrices were visualized in full and sparse

versions. The sparsified matrix was obtained by applying a threshold that retained only connections associated with FC weights above a predefined percentile of the FC weights distribution [169]. In this study, the threshold was set to the 80th percentile, following van den Heuvel et al. (2017) [170].

Subsequently, the FC matrices were organized by grouping the 7 RSNs (Yeo 2011) belonging to the two cerebral hemispheres, first left and then right, in the subsequent order: VIS, SOMMOT, DORSATTN, SALVENTATTN, LIMBIC, CONT, DEFAULT. These networks were concatenated with the twelve subcortical and cerebellum regions (organized into the SUBCORTICAL group), also divided into left and right hemisphere. This structured organization allowed highlighting the two secondary diagonals of the average FC matrices, representing interhemispheric homotopic connections (i.e., homologous regions belonging to different hemispheres). Several studies have indeed demonstrated the presence of strong homotopic connections in the human brain, becoming a distinctive feature of the functional connectivity map [22], [171], [63], [172]. On the contrary, average matrices were not computed and visualized for patients because the presence of tumours with highly heterogeneous grades, locations, and aggressiveness within the group makes the analysis at the group level less informative.

Considering that, according to graph theory (explained in detail in chapter 1.2.1), an FC matrix can be interpreted as a network, where nodes represent brain regions and links represent connection values, node strength was derived as a basic measure to characterize the network structure. To do this, the same 80th percentile threshold used for the average matrices was applied to the FC matrices of each individual subject (both healthy and patient, in both F_1 and F_2), retaining the top 20% of strongest connections. Thus, the strength of each node was calculated by summing the values of its connections along the rows (or equivalently columns, because FC is a symmetric matrix), providing the strength value for each region. Then, for each subject in the control group and patient group, two row vectors (1x number of ROIs) of strength were obtained, one for each frequency band.

2.4.2 Within-individual metabolic measures

Within-individual metabolic connectivity matrices were calculated using the method based on Euclidean Similarity (ES) implemented by (Volpi et al., 2022) [108], already detailed in chapter 1.2.3. For each pair of TACs, z_1 and z_2, the Euclidean distance $d_{z1,\,z2}$ is calculated:

$$d_{z1,z2=}\sqrt{\sum_{i=1}^{T}\left(z_{i,1}-z_{i,2}\right)^{2}}$$

where T is the number of time points. An index of the ES is derived by subtracting 1 from the normalized distance $d_{z1,z2}$, which is then divided by the maximum distance between TAC pairs, thereby scaling it within the interval [0, 1]. Because of the skewed distribution of ES values, a Fisher z-transformation is applied, followed by a subsequent rescaling of values within the range [0, 1]. Thus, the wi-MC are computed for both healthy controls and patients. In addition, subject-level *SUVR* and two-tissue compartmental model kinetic parameters (K_1, k_3, K_i) have been organized in row vectors (1 x number of ROIs), with one static value for each of the 86 ROIs.

Similar to the FC matrices, both the wi-MCs and the static metabolic parameters (K_1, k_3, K_i, *SUVR*) were also structured by categorizing the 7 RSNs, plus subcortical regions. Then, the group-average MC matrix was derived by averaging all healthy control's wi-MCs and visualized in full and sparse versions. The sparsified matrix was obtained by applying the same 80th percentile threshold used with FC matrices, to retain only the 20% of the highest metabolic connections. As shown by Volpi et al. (2022) [108], using Euclidean similarity as a metric, it is also possible to reveal a network structure in MC matrices, i.e. with clearly distinguishable interhemispheric homotopic connections (right hemisphere-left hemisphere), as expected from brain connectivity studies.

The same considerations made for mean FC matrices in patients also apply to mean MC matrices, which would be uninformative for patient-level analysis.

2.5 PLSC multimodal integration

For each pair of functional and metabolic measures collected from the control sample, a partial least squares correlation analysis (PLSC) was performed to assess the presence of multivariate correlation patterns between the two band-pass filtered functional components and the local (i.e., K_1, k_3, K_i, and *SUVR*) or network (i.e., MC) metabolic measures. As described in the previous chapter, PLSC is a powerful multivariate method designed to capture associations across two modalities of data and is particularly suited to handle the large datasets typical of contemporary neuroimaging research [128]. Specifically, the following multivariate combinations were evaluated (X-Y), for both F_1 and F_2 band-pass filtered FC measures:

- K_1 - FC_{STR}
- k_3 - FC_{STR}
- K_i - FC_{STR}
- *SUVR* - FC_{STR}
- FC-MC

In the case where local metabolic parameters K_1, k_3, K_i, and *SUVR* were considered as the metabolic counterparts, the corresponding node-wise strength of FC (FC_{STR}) was used for each subject. Meanwhile, for *MC*, the edgewise upper triangular features were selected to provide a whole-network assessment of the functional-metabolic coupling.

Therefore, the input matrices were obtained by concatenating:

- the vectors of the local metabolic parameters of all subjects to generate four matrices of dimensions 42 x 86 (number of subjects x number of ROIs), one for each of the parameters K_1, k_3, K_i, and *SUVR*;
- the strength vectors of all subjects, resulting in two matrices of dimensions 42 x 86 (number of subjects x number of ROIs), one for each frequency band of the corresponding FC (F_1 and F_2);
- all entries of the upper triangular portion of the FC matrices of each subject, resulting in two matrices of 42 x 3655 (number of subjects x entries of the upper triangular), one for F_1 and one for F_2;
- all entries of the upper triangular part of the MC matrix of each subject, resulting in a matrix of 42 x 3655 (number of subjects x entries of the upper triangular).

For each latent dimension, each PLSC analysis generates a pair of functional-metabolic salience maps corresponding to the left and right singular vectors of the data covariance matrix. It also produces a set of functional-metabolic latent scores representing the projection of the original data onto these saliences. The statistical significance of multivariate correlation patterns was assessed using permutation testing (200 permutations, with a critical value of α=0.01) [126], [138], while the reliability of nonzero salience values was assessed by bootstrapping (using 100 random samples) and calculating standard scores relative to the bootstrap distributions. The number of random permutations and bootstrapping samples was kept relatively low to manage computational complexity, especially for edgewise features. Salience matrices were considered reliable if the absolute standard score was greater than 3, following a previous work [173].

The significance of the salience vectors was determined by assessing whether zero was included in the corresponding 95% confidence interval distribution.

Given the smaller sample size compared to the imaging variables, PLS models are susceptible to overfitting, resulting in spurious associations that may not generalize well to new data. Therefore, the generalizability of the multivariate correlation patterns obtained from each PLSC analysis was tested using a K-fold cross-validation procedure with 7 folders (repeated for 100 iterations), retaining 14% of the subjects for the test set in each iteration. After removing the test subjects from the data set, salience maps were estimated from the remaining data (i.e., the training set), and the test-subject data were projected onto these saliences to obtain test latent scores. The correlation between the original and test latent scores was then evaluated, with high generalizability assumed if the scores aligned along the identity line [174]. The threshold for these correlation values to consider the corresponding metabolic-functional pair as generalizable was set at 0.5. Last, Pearson's correlation between metabolic and functional latent scores was used to quantify the amount of metabolic variance explained by the proposed functional counterpart. Prior to the PLSC analysis, z-score scaling was performed across subjects to ensure that the range of variability for all measures was comparable across subjects and features.

Due to significant differences observed between subjects in the metabolic parameter matrices (K_1, k_3, K_i, and $SUVR$), an additional analysis was performed by applying intra-individual z-score transformation prior to the between-subject scaling.

Each PLSC analysis yields individual-level latent scores, providing insight into the expression of underlying patterns for each subject. Leveraging subject-level measures of resting-state brain functionality and metabolism, the potential correlations between these measures and the individual latent scores was explored, shedding light on the role of brain functionality in shaping the significance of these latent components.

In particular, for the FC-MC pair (in both frequency bands), which showed the highest degree of coupling among all tested pairs, a deeper analysis of the nature of this functional-metabolic link was performed.

This was done by creating binary masks corresponding to only the significant positive (or negative) saliences of the FC and MC salience maps taken individually. These masks were then applied to the respective FC and MC matrices to obtain two masked matrices for

each connectivity matrix: one containing only entries corresponding to positive saliences and the other containing only entries corresponding to negative saliences. The values of the entries in the masked matrices were then summed to estimate the magnitude of the functional and metabolic variables associated with these salience weights of FC and MC (positive or negative). Overall, it was expected that in healthy subjects, a higher sum value (indicating a more influential weight of that variable) would correspond to a subject with a positive score if the salience was positive and negative if the salience was negative; conversely, lower sum values were expected.

Following this single-subject analysis, attention was shifted to examining significant saliences common to FC and MC, and thus a group-level analysis was conducted to assess which regions carry more weight in integration, along with their respective directionality in driving the coupling between FC and MC. This involved creating a mask indicating regions where significant saliences were either concordant or discordant between FC and MC salience maps, and subsequently quantifying the number of concordant and discordant saliences for each network on a percentage basis. Then, after masking the matrices of all subjects by considering only entries common to FC and MC in the salience pattern, HC group-averaged masked matrices of FC and MC were derived. The analysis of control subjects was concluded with a further investigation of differences in the pattern of significant saliences common to FC and MC between the two brain hemispheres. To this end, topographic maps of saliences common to FC and MC were generated, separately highlighting concordant and discordant regions for ease of interpretation.

2.5.1 Oncological patient's inclusion in the analysis

For each functional-metabolic pair demonstrating a strong level of generalizability (correlation of all scores to test scores greater than 0.5), the least-squares line that best captures the relationship between X and Y within the significant latent plane was identified. Subsequently, the shortest distance of each individual's latent point from this least-squares line was calculated, providing an estimate of the distance distribution within the HC sample. The 90^{th} percentile of this distribution was then determined to establish the "normality" range of coupling distances where HC scores are typically located. After normalizing features using mean and standard deviation values from the HC group, the functional and metabolic variables of patients were projected onto the latent plane. This involved computing, for both X and Y, subject-level linear combinations of functional

and metabolic measures, using salience weights previously computed for the HC group [175]. The resulting latent scores were then projected onto the latent plane, allowing identification of patients who deviate from the expected healthy range for the specific functional-metabolic coupling pair, termed “out-patients”.

To investigate potential associations between the deviation from the HC distance distribution of out-patients and the anatomical location of the tumour, further analysis was conducted on the corresponding tumour frequency map. This map was generated by averaging individual spatial tumour masks, with each mask weighted by the distance of the corresponding latent point from the regression line. This approach aimed to minimize sensitivity in identifying out-patients based on a specific threshold.

Additionally, potential associations between the degree of deviation of out-patients (i.e., their distance from the regression line) and the volume of the lesion were explored.

Given the considerations made for the FC-MC pair in the analysis of control subjects, before projecting the latent scores of the patients onto the latent space of the healthy subjects, the patient’s functional and metabolic connectivity matrices were masked using the binary mask that considers only the common saliences between FC and MC (described in the previous paragraph). This allowed a preliminary investigation of the differences in the topology of the FC and MC matrices and the variations in functional-metabolic coupling, not only between patients and healthy subjects, but also within the same patient group, which is characterized by significant heterogeneity in terms of lesion localization and volume.

Chapter 3

Results

3.1 Functional and metabolic patterns at group-level

This section provides a qualitative overview of the group-averaged patterns of metabolic parameters K_1, k_3, K_i *and SUVR*, and FC and MC matrices in control subjects.

First, from the observation of the topographical distributions of K_1, k_3, K_i *and SUVR* shown in Figure 3.1, the following considerations could be made:

- Higher values of K_1, which reflect cerebral blood flow and thus the distribution of the radiotracer among different brain regions, are found in regions associated with brain networks that exhibit higher metabolic activity. These include the medial occipital regions (part of the visual network) and regions involved in more active cognitive functions, such as the posterior cingulate (PCC), medial temporal and retrosplenial cortex (components of the default mode network), as well as certain subcortical areas (thalamus, putamen, and cerebellum).
- The irreversible elimination constant k_3, which reflects the rate at which [^{18}F]FDG is phosphorylated and incorporated into brain cells, is fairly uniform across brain regions, reflecting normal metabolic homogeneity. However, there are slight variations in frontal regions involved in more active cognitive functions, such as regions of the PCC that form control networks and the DMN, and especially in the subcortical putamen. Unlike K_1, the value of k_3 in the cerebellum is lower than in the other regions, consistent with the higher efficiency of the oxidative metabolic pathway that distinguishes the cerebellum from the cortex [120].
- The tissue uptake constant K_i, which reflects both cerebral blood flow (K_1) and metabolic activity (k_3), also shows a nearly uniform distribution throughout the brain, with slightly higher values in the precuneus (control network), intraparietal cortex (DMN) and putamen, all regions involved in more active cognitive functions. Lower K_i values are observed in the cerebellum (consistent with those found for k_3), as well as in the limbic area and hippocampus.

- In terms of *SUVR*, areas showing elevated metabolic activity consist of the medial occipital regions (visual network), the prefrontal regions (control network), and the precuneus/posterior cingulate and ventromedial prefrontal cortex (DMN), as outlined by Palombit et al., (2022) [122]. Conversely, regions such as the cerebellum (commonly used as a reference area), limbic, and subcortical ROIs exhibit lower levels of glucose consumption.

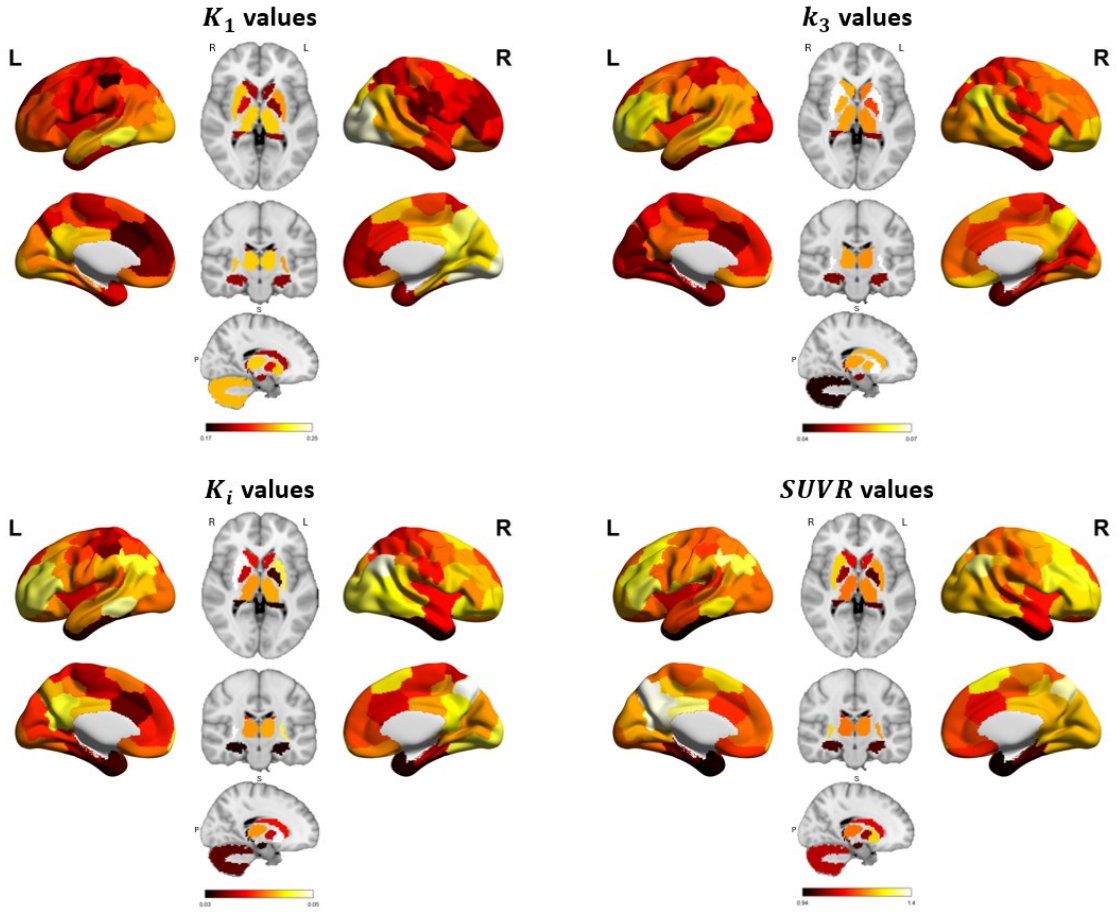

Figure 3.1: *Group-averaged metabolic parameters distribution. From top left to bottom right, there are ROI-level K_1, k_3, K_i and SUVR values in cortical parcels (in the lateral parts) and subcortical parcels (in the central part). Hemisphere orientation is reversed in the visualization of subcortical regions, as indicated by the letters "L" and "R" in the figure.*

Overall, among the four parameters, the distributions of K_i and *SUVR* are more similar to each other. In addition, the parameters K_1, k_3 and K_i show differences in values between the right and left hemispheres, albeit modest: K_1 tends to be more occipital in the right hemisphere, while k_3 and K_i are more frontal in the left hemisphere and more occipital in the right. Conversely, *SUVR* appears to be the most symmetrical parameter between the two hemispheres.

For what concerns the visualization of the FC matrices, below are reported the HC group-averaged FC full and sparse matrices (upper panel, left and right respectively), along with their corresponding standard deviation matrix and average p-value matrix thresholded at 0.05 (lower panel), both in F_1 (Figure 3.2) and F_2 (Figure 3.3).

In both frequency bands, both the full FC matrix and the sparsed version emphasize the homotopic interhemispheric connections (secondary diagonals of the matrices) and a diagonal block structure with limited isolated connections, which is representative of the high modularity of brain functional organization. Indeed, several long-range connections between functional areas are also evident. However, the correlation values between unimodal networks (i.e., VIS, SOMMOT, DORSATTN, SALVENTATTN) and the block of attentive and cognitive networks (i.e., DORSATTN, SALVENTATTN, CONT, and DMN) characterizing the transmodal ones, are negative, reminiscent of the anticorrelated activity between cognitive and unimodal networks reported by Tomasi (2011) [176]. These long-range connections are generally smaller in magnitude than intra- and short-range connections, consistent with Jamadar (2021) [121].

More specifically, the unimodal networks (VIS, SOMMOT, DORSATTN) show high connectivity values both in intra-network and in inter-network connections to each other and to the salience network. Among the transmodal networks, the CONT and the DMN show the highest values of intra-network and inter-network connectivity. Moreover, CONT tends to be more connected to the intra-hemispheric regions of the intraparietal sulcus of DORSATTN and the insular regions of the SALVENTATTN network. On the other hand, the DMN also shows increased connectivity with intra-hemispheric LIMBIC regions. However, the limbic network tends to be more disconnected from the rest of the ROIs in general. Subcortical regions are also generally less connected to the rest of the connectivity pattern, except for the thalamus, putamen, and intra-hemispheric hippocampus.

Although the FC matrices obtained in the two bands are generally similar, the main differences were observed in the LIMBIC, in some subcortical regions (thalamus and caudate) and in some parcels of the DEFAULT, where the FC values obtained in the second frequency band were lower than the corresponding ones obtained in the first frequency band.

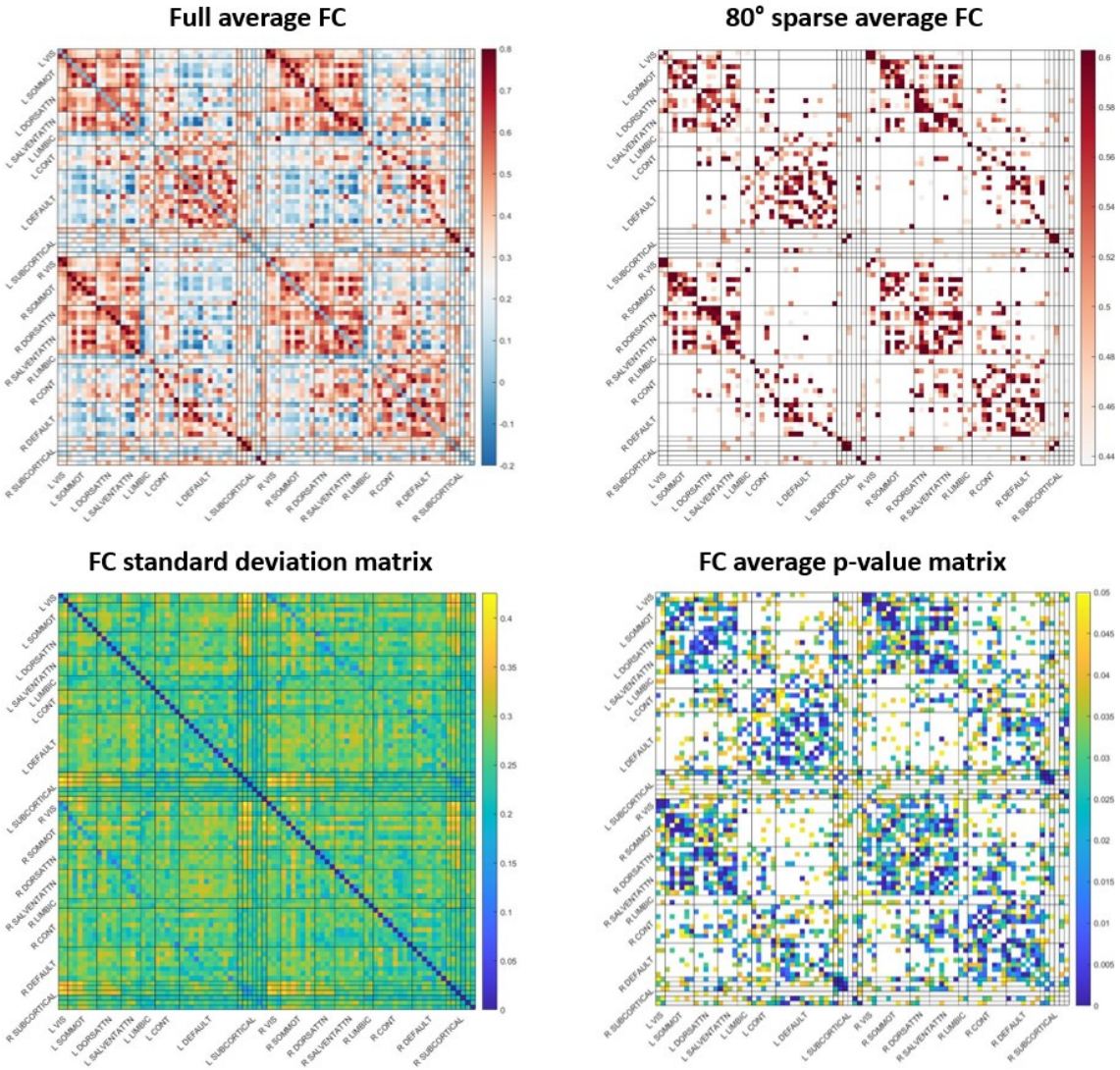

Figure 3.2: *Visualization of the HC group mean FC matrices in the F_1 band (0.008-0.11 Hz). The top panel shows the full version (left) and the sparsified version (right) at the 80th percentile, grouped into the seven RSNs (VIS, SOMMOT, DORSATTN, SALVENTATTN, LIMBIC, CONT, DEFAULT) and the SUBCORTICAL network. Both matrices highlight the homotopic interhemispheric connections and a diagonal block architecture with few isolated connections, representative of the high modularity of the brain functional organization. The lower panel shows the FC standard deviation matrix of the HC group (left) and the FC mean p-value matrix (right), in which the non-significant values (p-value>0.05) have been plotted in white to emphasize the statistically significant correlations.*

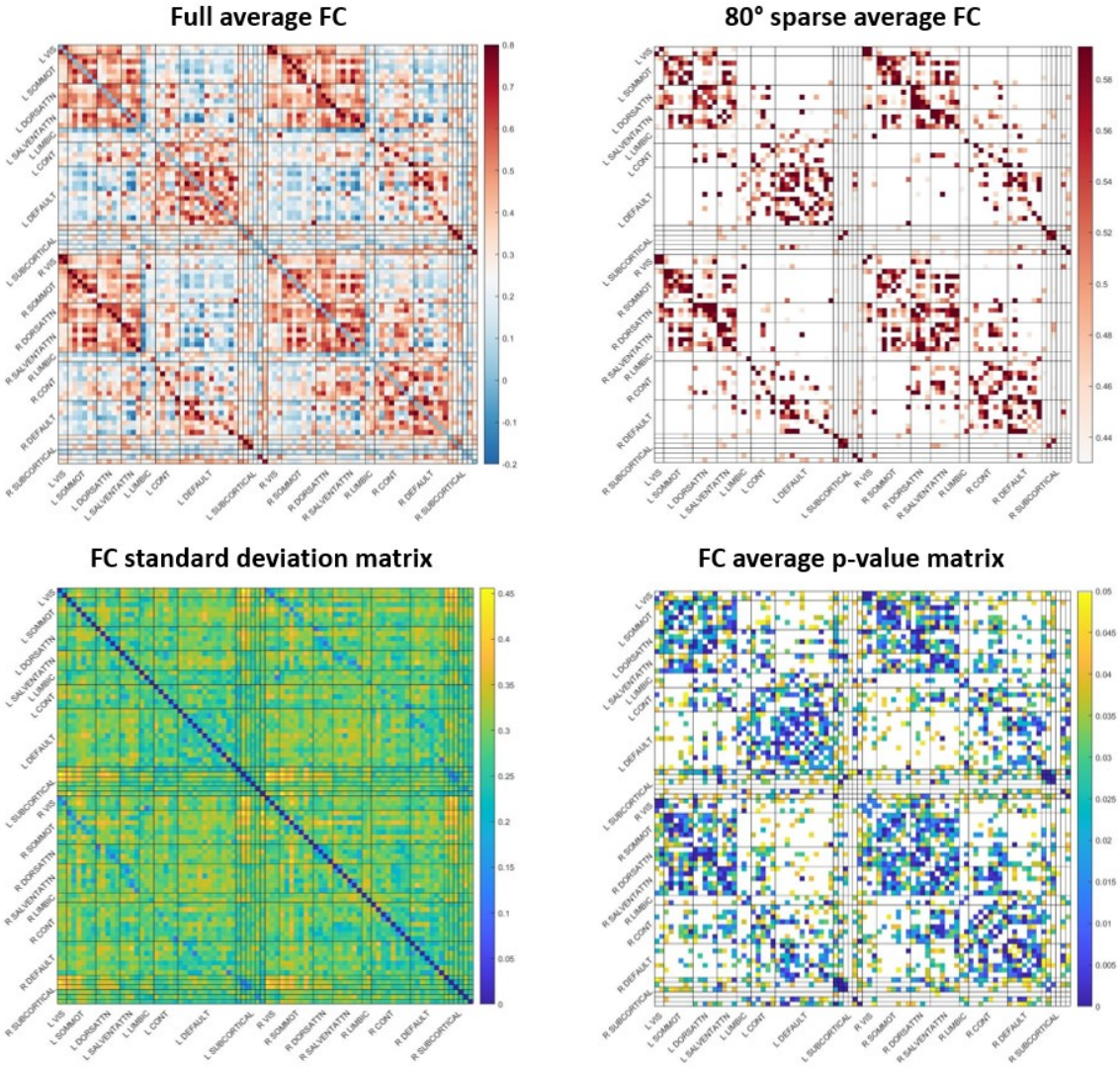

Figure 3.3: *Presentation of HC group average FC matrices within the F_2 frequency band (0.008-0.21 Hz). The upper section exhibits the complete matrix (on the left) and the sparsified version (on the right) at the 80th percentile. These are categorized into seven RSNs (VIS, SOMMOT, DORSATTN, SALVENTATTN, LIMBIC, CONT, DEFAULT) and the SUBCORTICAL network. Both matrices illustrate homotopic interhemispheric connections and a diagonal block structure with limited isolated connections, indicative of the brain's high modularity in functional organization. However, the values are lower compared to those in the F1-band filtered FC matrices, maybe due to the presence of slow hemodynamic function information. The lower section presents the FC standard deviation matrix of the HC group (on the left) and the FC mean p-value matrix (on the right), with non-significant values (p-value>0.05) displayed in white to underscore the statistically significant correlations.*

Figure 3.4 shows the HC group-average MC full and sparse matrices (upper panel, left and right respectively), with their corresponding standard deviation matrix. From the observation of the MC at the group level, in both matrices, the homotopic interhemispheric connections are clearly visible, but even more so in the sparsified matrix. Moreover, a pronounced connectivity can be noticed in unimodal regions (VIS,

SOMMOT), both in intra- and inter-network connections, as well as in some frontal regions of the DMN, and temporal areas of the DORSATTN, in line with Volpi (2022) [108]. Conversely, the CONT, LIMBIC, and SUBCORTICAL areas (except for the thalamus and putamen) tend to be more disconnected from the rest of the ROIs.

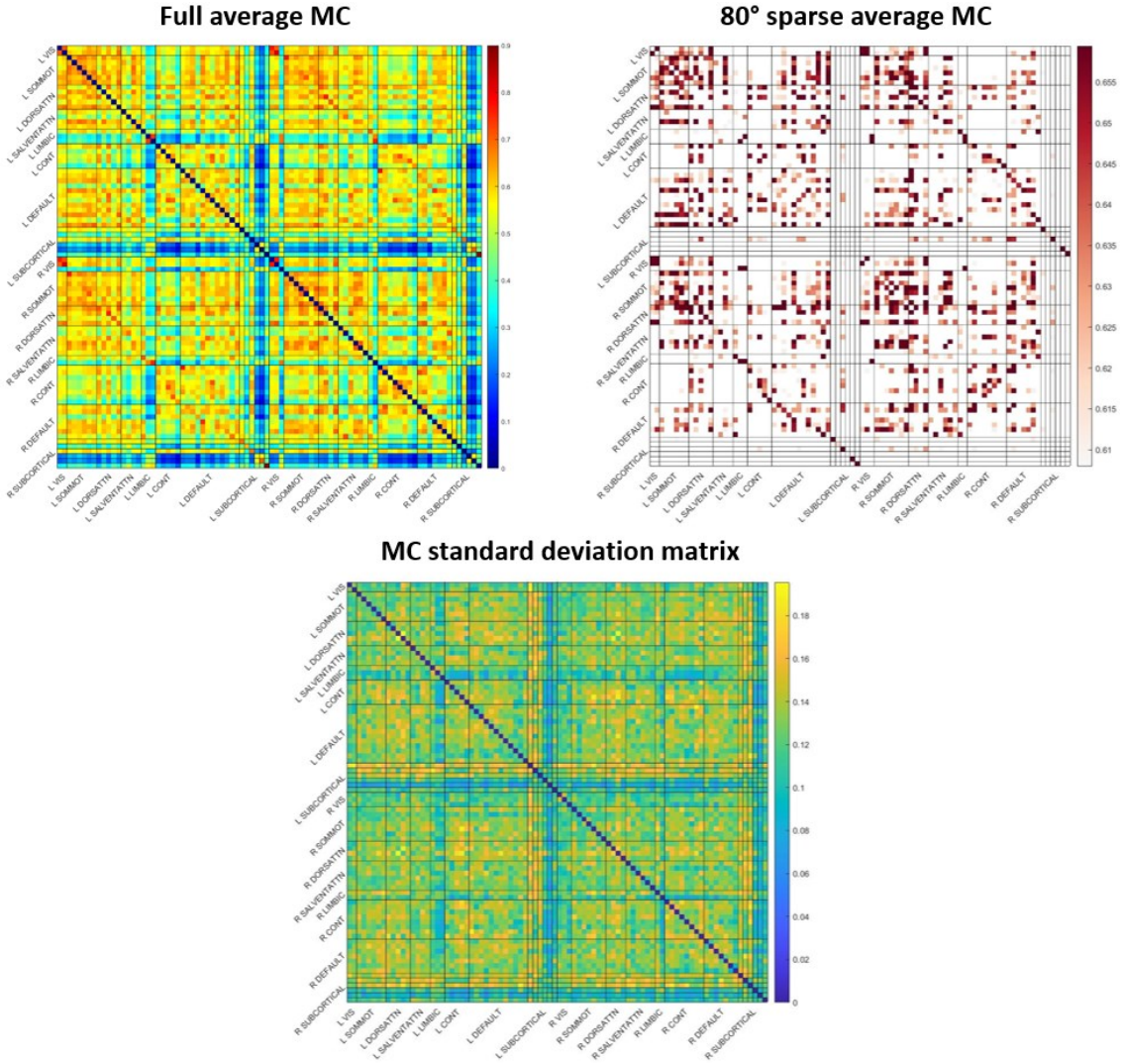

Figure 3.4: *Visualization of the HC group mean MC matrices. The top panel shows the full version (left) and the sparsified version (right) at the 80th percentile, grouped into the seven RSNs (VIS, SOMMOT, DORSATTN, SALVENTATTN, LIMBIC, CONT, DEFAULT) and the SUBCORTICAL network. In both matrices, the homotopic interhemispheric connections are clearly visible, but even more so in the sparsified matrix. The lower panel shows the MC full standard deviation matrix of the HC group.*

3.2 Generalizable functional-metabolic pairs

Before detailing the results obtained from the multivariate analysis performed, it is important to briefly recall the meaning of the PLSC outputs, as follows:

- The mutually orthogonal latent components (LCs), obtained from the SVD of the cross-covariance matrix *R*, are abstract representations of information in the data that are not directly observable. The first and subsequent LCs account for the largest and progressively smaller portions of the *R* matrix (indicated by the square of the singular value), respectively.
- The saliences (*V* and *U*) indicate the strength of the contribution of each functional (or metabolic) variable (ROI-level measures) to the functional-metabolic correlation explained by that particular latent variable.
- The scores (L_x and L_y) represent the projection of each subject's original functional (or metabolic) data (in X or Y) onto the multivariate functional (or metabolic) salience pattern (in *V* or *U*), thus providing a measure of the similarity of a subject's individual functional (or metabolic) data to the salient functional (or metabolic) pattern.

After applying PLSC to each of the functional-metabolic pairs summarized in Table 3.1, generalizability was then tested to identify combinations that yielded a Pearson's correlation coefficient between original and test latent scores greater than 0.5 in at least 50% of the 100 iterations in which the analysis was repeated. Specifically, pairs that showed generalizable results, reported as the average of all correlations above the threshold, are highlighted in green, while those that did not pass this test, reported as the average of all correlations below the threshold, are highlighted in red (Table 3.1).

	Pair	Latent component (LC)	corr(L_x,L_y)	X scores generalizability	Y scores generalizability
F_1 band (0.008-0.11 Hz)	***K_1-FC_{STR}***	1	0.6413	0.9903	0.5951
	zK_1*- FC_{STR}	2	0.7127	0.2100	0.2457
	k_3- FC_{STR}	1	0.6370	0.9972	0.2070
	zk_3*- FC_{STR}	2	0.7372	0.0858	0.0001
	Ki- FC_{STR}	1	0.6584	0.9976	0.0468
	zKi*- FC_{STR}	1	0.8020	0.2593	0.2048
	SUVR- FC_{STR}	1	0.7487	0.7475	0.5792
		3	0.7180	0.7393	0.6529
		4	0.7747	0.2340	0.1437
	zSUVR*- FC_{STR}	1	0.6680	0.0319	-0.2275
		2	0.6939	0.2437	0.2773
		3	0.7314	0.1370	0.2383
	****FC-MC**	1	0.7452	0.8786	0.8587
		2	0.7983	0.8405	0.6046

* within-individual z-scored, ** upper triangular portion

	Pair	Latent component (*LC*)	corr(L_x,L_y)	X scores generalizability	Y scores generalizability
F_2 band (0.008-0.21 Hz)	***K_1- FC_{STR}***	1	0.6573	0.9899	0.6066
	zK_1*- FC_{STR}	1	0.6135	0.2253	0.1417
	k_3- FC_{STR}	1	0.6368	0.9970	0.3690
	zk_3*- FC_{STR}	2	0.7459	0.1726	0.0556
	Ki- FC_{STR}	1	0.5902	0.9977	0.3020
	zKi*- FC_{STR}	1	0.8024	0.1483	0.0914
	SUVR- FC_{STR}	1	0.7406	0.3518	0.2374
		3	0.7215	0.2782	0.3179
		4	0.7763	0.3808	0.2925
	zSUVR*- FC_{STR}	1	0.7174	0.2844	0.1792
		3	0.7951	0.0330	0.0756
	****FC-MC**	1	0.7375	0.9194	0.8307
		2	0.7839	0.6982	0.5999

* within-individual z-scored, ** upper triangular portion

Table 3.1: *The results of the PLSC analyses are presented, for both F1 and F2 frequency bands. For each coupling pair, the ordinal number of the significant latent component derived from the PLSC analysis (second column) and the Pearson's correlation value between latent score, are reported. The corresponding p-values were less than 0.05 in all cases. Additionally, the outcomes of the generalizability tests for X (fourth column) and Y (fifth column) are provided. PLSC results are considered generalizable if the correlation between original and test latent scores exceeds 0.5 for both X and Y (as highlighted in green rows).*

It is immediately apparent that none of the pairs considering metabolic parameter matrices with the additional intra-individual z-score (*zK_1, zk_3, zK_i and zSUVR)* can be assumed generalizable (In Table 3.1, marked in red).

Looking at the values reported in the last two columns of Table 3.1, it is possible to observe that only the *K_1-FC_{STR}*, *SUVR-FC_{STR}*, and *FC-MC* pairs can be considered generalizable, while the generalizability test fails for both the *k_3-FC_{STR}* and *K_i-FC_{STR}* pairs. In particular, it can be noted that *K_1* is linked with the *FC_{STR}* in both frequency bands; the same occurs between the upper triangular portions of the *FC* and *MC* matrices. However, the coupling between *SUVR-FC_{STR}* turned out to be generalizable only in the case of *FC* derived from the F_1 frequency band. Moreover, it is noteworthy that in all the generalizable pairs, a significant functional-metabolic association is found in the first dimension, corresponding to the first singular value of the matrix of correlations between X and Y [128]. Additionally, for the *FC-MC* and *SUVR-FC_{STR}* pairs, a significant association was found in the second and third dimensions, respectively. However, in the *FC-MC* pair, in both frequency bands, the second component showed a higher correlation value between functional and metabolic scores (corr(L_x,L_y)) compared to the first component. For this reason, it was decided that only the second component in both frequency bands would be investigated in more detail. Instead, in the *SUVR-FC_{STR}* pair, the latent component with the highest corr(L_x,L_y) value is the first, so it was further explored in the analysis. Therefore, following the same criterion, it was considered to continue the investigation of the *K_1-FC_{STR}* coupling only in the F_2 frequency band, where the corr(L_x,L_y) value was found to be higher. Table 3.2 below summarizes all the pairs that were further considered in the analysis (examining the corresponding patterns of saliencies and scores), with the associated scatter plots of original vs. test latent scores shown in Figure 3.5.

	Pair	**Latent component (*LC*)**
F_1 band (0.008-0.11 Hz)	***SUVR-FC_{STR}***	1
	****FC-MC**	2
F_2 band (0.008-0.21 Hz)	***K_1-FC_{STR}***	1
	****FC-MC**	2

** upper triangular portion

Table 3.2*: The latent components of the generalizable functional-metabolic pairs that have undergone further considerations, observing their corresponding patterns of scores and saliences, are reported.*

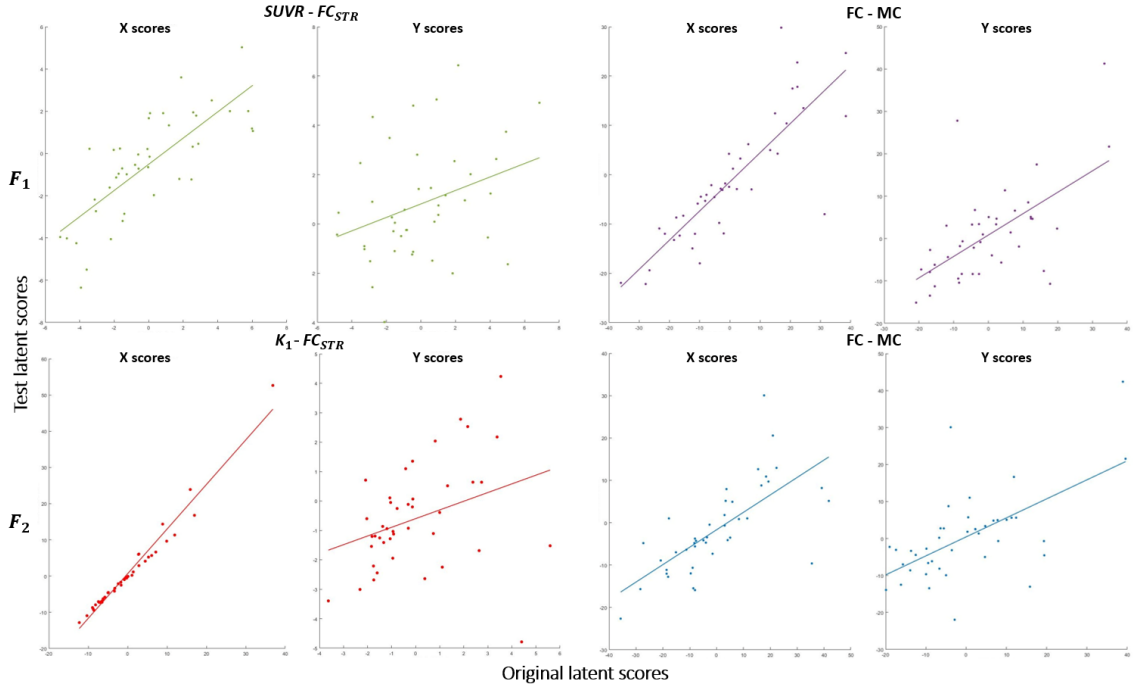

Figure 3.5: *Scatter plots showing the original versus test latent scores resulting from the 7-fold cross-validation process for functional and metabolic features latent scores within each potential coupling pair, in F_1 (top) and F_2 (bottom). Pearson's correlations between original and test latent scores are provided in Table 3.1. For PLSC patterns deemed generalizable, original (x-axis) and test (y-axis) latent scores are expected to align along the identity line (i.e., a correlation exceeding 0.5).*

In the following paragraphs, the results of the analysis performed will be reported and described, following the order in which the pairs were tested: K_1-FC_{STR}, $SUVR$-FC_{STR} and FC-MC. It is important to specify that the saliences were visualized by reordering the Yan atlas parcels to concatenate the homologous regions of the two hemispheres (left first, then right). This made it possible to distinguish the overall trend of saliences in the unimodal networks from that in the transmodal ones.

3.2.1 K_1-FC_{STR} pair

Regarding the salience maps, different scenarios emerge when comparing metabolic and functional weights, as shown in Figure 3.6. For K_1, it is evident that saliences are uniformly positive and consistent across networks, with relatively homogeneous values. On the other hand, FC_{STR} saliences show a mixture of positive and negative weights across networks. Specifically, there are predominantly positive saliences in unimodal (VIS, DORSATTN), DEFAULT, and some of the SUBCORTICAL networks (especially thalamus), while negative values are more prevalent in LIMBIC and CONT networks. Consequently, the agreement between K_1 and FC_{STR} salience is highest in VIS,

DORSATTN, DEFAULT, and some SUBCORTICAL networks, while LIMBIC and CONT networks show more discordance between the two patterns.

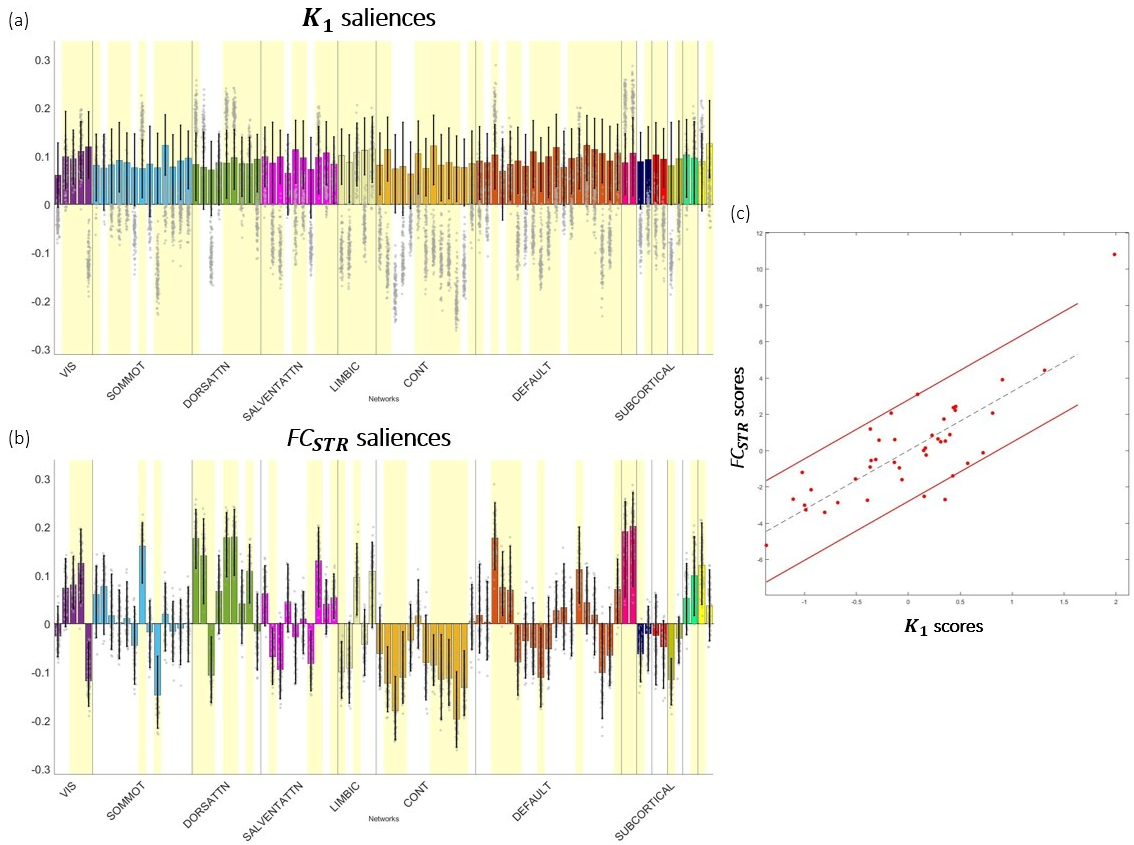

Figure 3.6: *The graphical representation on the left includes bars and individual dots indicating the average and spread of K_1 (a) and FC_{STR} (b) salience across 100 bootstraps. Yellow shading highlights salience weights significantly different from zero. The colour of the bars indicates the affiliation with RSN. Additionally, scatter dots are plotted on the latent space (c), with each dot corresponding to a subject. The plot also includes the least-square best-fitting line and a normality band defined by the 90th percentile of the group-level distance distribution.*

Looking at the latent scores shown in Figure 3.6c, these results suggest that two categories of subjects contribute to defining the variance of the component: some subjects have primarily negative K_1 values (relative to the group-averaged value) and high FC_{STR} values in LIMBIC and CONT networks, resulting in a negative score. Conversely, subjects who have an overall positive whole-brain K_1 value, coupled with high FC_{STR} values in unimodal, DMN, and certain subcortical (thalamic) networks, and low FC_{STR} values in high-order areas such as LIMBIC and CONT, tend to have a positive score.

3.2.2 *SUVR- FC_{STR}* pair

Looking at the salience maps in Figure 3.7, there are also different trends when comparing *SUVR* and FC_{STR} weights. In the case of *SUVR* saliences, all networks generally exhibit both positive and negative weights, although significant saliences are predominantly biased towards positivity. The highest magnitude of weights is observed in DORSATTN, CONT, certain parcels within the DMN, and SUBCORTICAL regions (especially thalamus, pallidum, and cerebellum).

Concerning FC_{STR} saliences, a substantial alternation of positive and negative weights within the network is observed, depending on the corresponding parcel. However, there's a prevalence of negative saliences in unimodal networks (VIS, SOMMOT, SALVENTATTN) compared to transmodal networks (CONT and DMN), where the number of parcels with positive weight increases. Furthermore, it's evident that the magnitude of the saliences increases with the transition from unimodal to transmodal networks (higher values in CONT). Among the subcortical regions, the cerebellum shows the highest weights. Overall, although a positive covariation pattern between *SUVR* and FC_{STR} is observed predominantly in transmodal networks and the cerebellum, these results demonstrate a moderate coupling between *SUVR* and FC_{STR} derived from *FC*, confirming what has been reported in the literature to date [122].

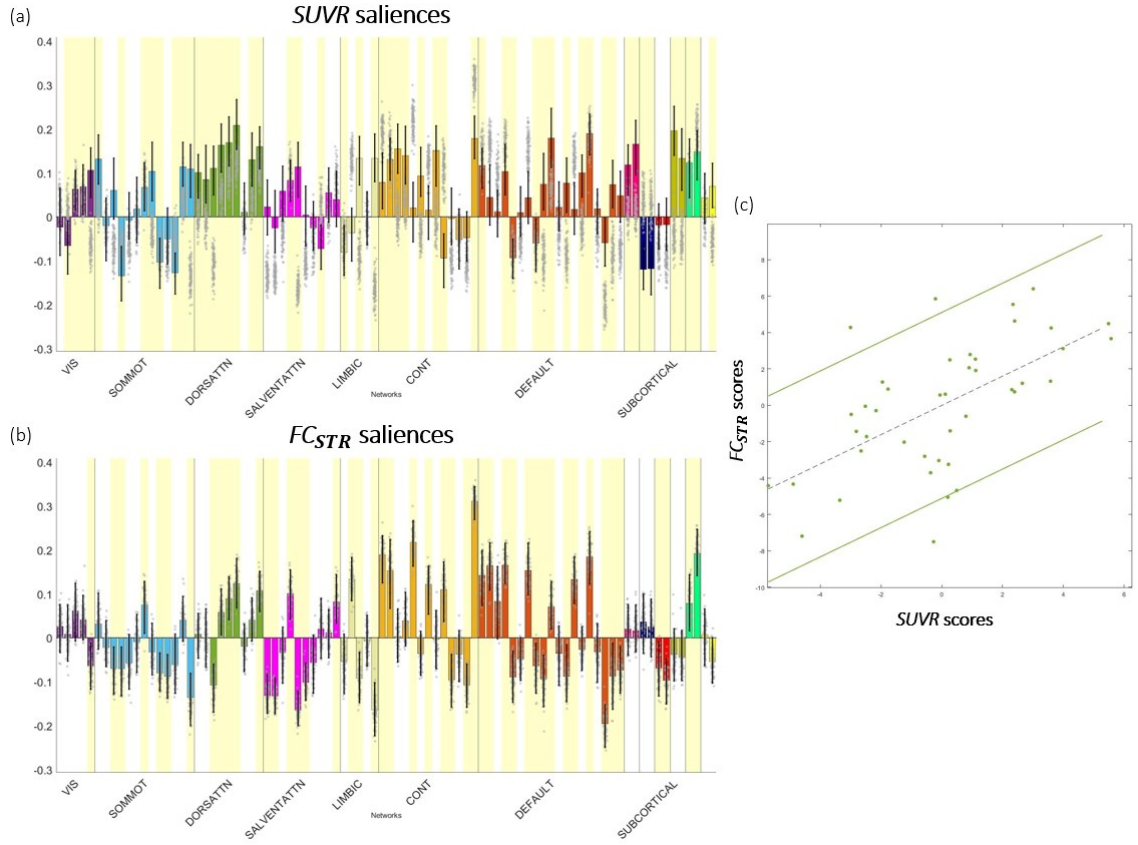

Figure 3.7: *The graphical representation on the left includes bars and individual dots indicating the average and spread of SUVR (a) and FC_{STR} (b) salience across 100 bootstraps. Yellow shading highlights salience weights significantly different from zero. The colour of the bars indicates the affiliation with RSN. Additionally, scatter dots are plotted on the latent space (c), with each dot corresponding to a subject. The plot also includes the least-square best-fitting line and a normality band defined by the 90th percentile of the group-level distance distribution.*

Looking at the scores plotted in Figure 3.7c, these results also suggest that two categories of subjects contribute to defining the variance of the component. Those represented by negative scores are characterized by a predominantly negative (relative to the group mean) *SUVR* and high FC_{STR} in ventromedial and dorsomedial prefrontal cortex (DMN) regions involved in high-level cognitive functions. Instead, those with a positive score showed an overall whole-brain positive *SUVR* associated with higher FC_{STR} in regions involved in attention and spatial perception and processing (temporo-occipital cortex, posterior cingulate cortex, and retrosplenial cortex of the DMN) and lower FC_{STR} in areas associated with high-level cognitive and behavioural functions.

3.2.3 FC-MC pair

Regarding the FC-MC pair in the F_1 band (Figure 3.8), the FC salience map shows that while the unimodal networks (VIS, SOMMOT, and DORSATTN) exhibit mainly positive saliences among themselves, the transmodal networks seem to have higher weights in connections between networks, especially SALVENTATTN with DEFAULT and CONT. Conversely, negative weights are predominantly observed in connections between VIS and transmodal networks. In addition, there is an interesting reversal in the salience between subcortical and unimodal networks, predominantly negative (except in the hippocampus), compared to the weights between subcortical and transmodal networks (predominantly positive).

The coupling with the metabolic counterpart, as indicated by the MC salience map, is supported by a distinct salience pattern, predominantly characterized by positive weights between unimodal and transmodal networks, and negative weights among unimodal networks. It is also noteworthy that SUBCORTICAL regions show negative weights with the unimodal networks and positive weights with the transmodal networks, as already highlighted in the FC salience map.

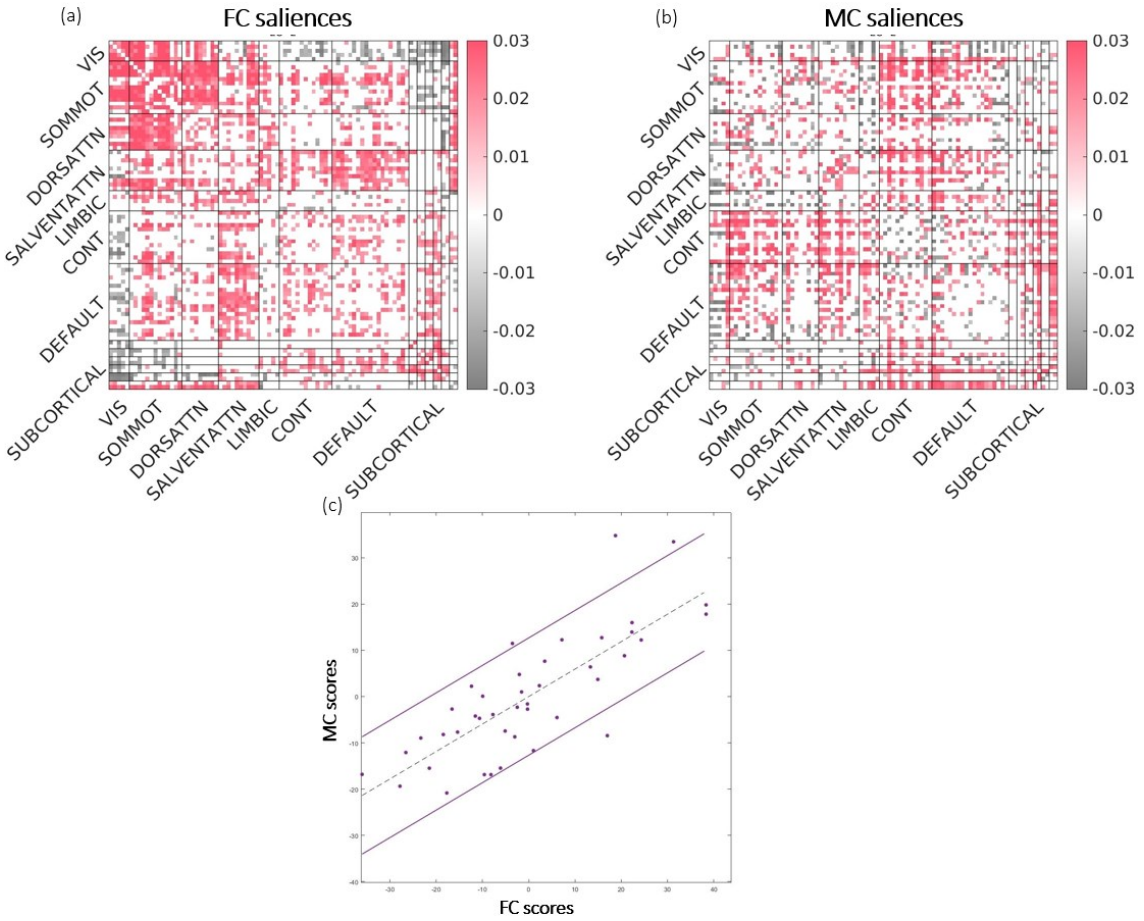

Figure 3.8: *The graphical representation on the left includes the salience pattern for FC (a) and MC (b) in F_1 band, with non-reliable weight values (i.e., absolute bootstrap ratio lower than 3) shown in white. Axis labels indicate the RSN affiliation of each ROI functional group. Additionally, scatter points are plotted on the latent space (c), with each point representing a subject. The plot includes a least-squares best-fit line and a band of normality defined by the 90th percentile of the group-level distance distribution.*

In this scenario, the correlation in the latent space is primarily influenced by two different groups of subjects, as shown in Figure 3.8c. The first group consists of individuals with negative FC connections, especially those with inter-unimodal network dependencies, and predominantly positive MC connections. These individuals are associated with negative latent scores. Conversely, the second group includes subjects with positive FC links and predominantly negative MC links within the unimodal networks, along with positive MC links facilitating communication between transmodal networks, resulting in positive latent scores.

In terms of MC, negative weights predominantly implicate the visual network and intra-network blocks, highlighting a dual state of metabolic integration and segregation that characterizes these two groups.

Figure 3.9 below shows the FC-MC pair in band F_2. Overall, the saliences patterns are very similar to those obtained in band F_1. However, it's worth noticing that both maps obtained in F_2 appear slightly sparser, especially in the inter-network connections, with even more negative values in the edges between unimodal and subcortical networks. As shown in Figure 3.9c, the pattern of latent scores also remains largely unchanged overall.

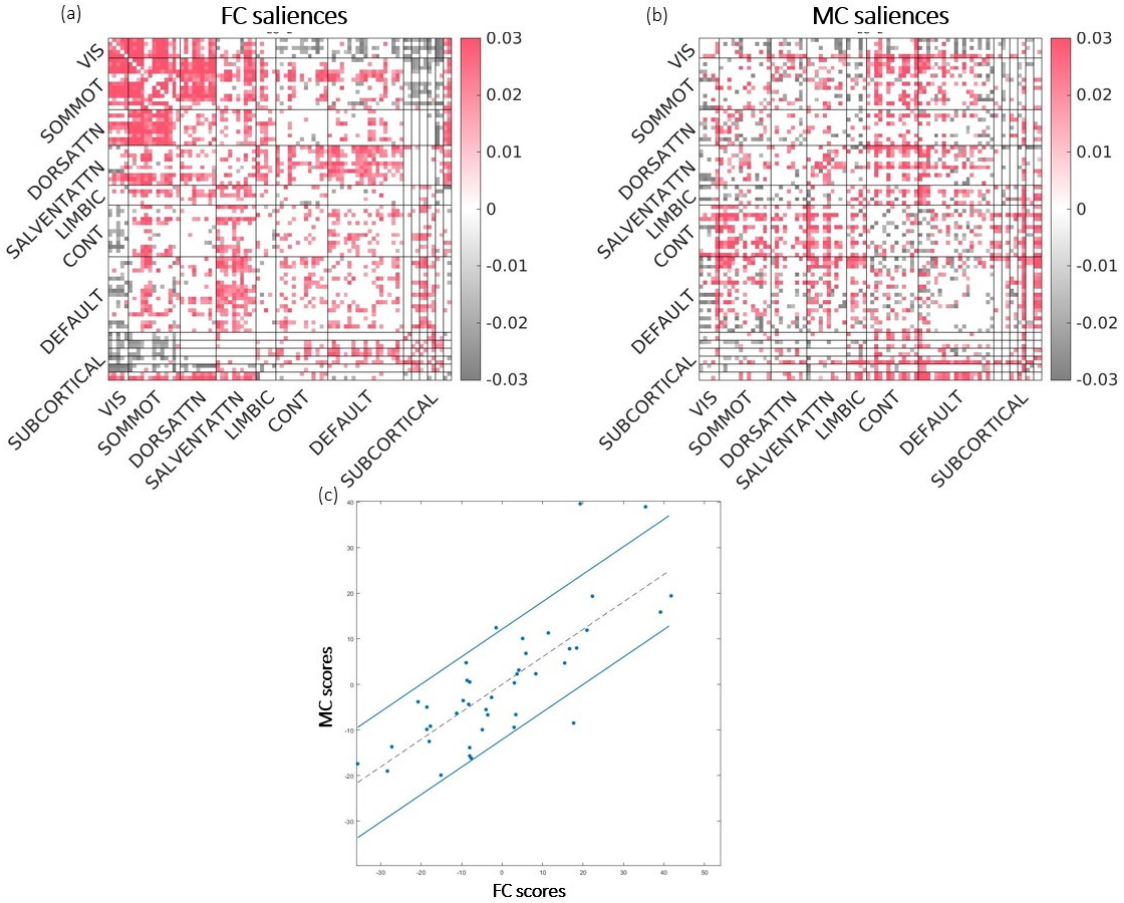

Figure 3.9: *The graphical representation on the left includes the salience pattern for FC (a) and MC (b) in F_2 band, with non-reliable weight values (i.e., absolute bootstrap ratio lower than 3) shown in white. Axis labels indicate the RSN affiliation of each ROI functional group. Additionally, scatter points are plotted on the latent space (c), with each point representing a subject. The plot includes a least-squares best-fit line and a band of normality defined by the 90th percentile of the group-level distance distribution.*

In-depth investigation of the FC-MC coupling

Considering that the FC-MC pair showed the highest values both in terms of corr(L_x,L_y) and generalizability (as reported in Table 3.1), further analysis of this coupling was performed in both frequency bands. Since the results obtained were nearly identical in both cases, it was decided to present only those obtained in the F_2 band below.

Figures 3.10 and 3.11 provide a more detailed insight into the relationship between the magnitude of each subject's score (a, b) and their respective matrices of functional variables (3.10 c, d, e, f) and metabolic variables (3.11 c, d, e, f). The sum value of the entries in the FC and MC matrices (masked for common significant saliences) corresponding to each subject is represented by a colour bar ranging from light blue to magenta, indicating increasing values. This value represents the total contribution of the functional variable (Figure 3.10) and the metabolic variable (Figure 3.11) in defining the score value for that subject. Observing the scatterplots, for both FC and MC values, considering positive salience (a), the sum increases with increasing score (i.e., progressively more magenta values), indicating that lower scores correspond to lower variable values, while higher scores correspond to higher values. Conversely, when negative salience is considered (b), the sum decreases with increasing score, indicating that lower scores correspond to higher variable values and higher scores correspond to lower values.

Observing the masked matrices of FC and MC corresponding to two extreme subjects, one with a low score (c, e) and one with a high score (d, f), it became clear that both FC and MC can discriminate essentially the same categories of subjects.

In particular, considering positive saliences (a), there are subjects:

- represented by a negative score and low sum (c), where lower FC values in unimodal regions and integration with SALVENTATTN correspond to lower MC integration values between unimodal and transmodal regions and higher values within CONT and DMN.
- characterized by a positive score and high sum (d), with higher FC values mainly in unimodal and subcortical regions corresponding to stronger MC relationships between CONT-SOMMOT, DMN-SOMMOT, and -DORSATTN, and weaker relationships within CONT and between CONT-DMN.

Complementary results are found by observing the masked matrices corresponding to negative saliences (b), where the subject with a negative score (e) has a higher sum value and a higher FC between VIS-transmodal and SUBCORTICAL with VIS and DORSATTN, while the subject with a positive score (f) has lower sum value and lower FC in the same regions of (e). Conversely, for the subject with a positive score and lower

sum (f), higher MC values are observed in CONT with itself and with DMN (negative score) and lower MC values (positive score).

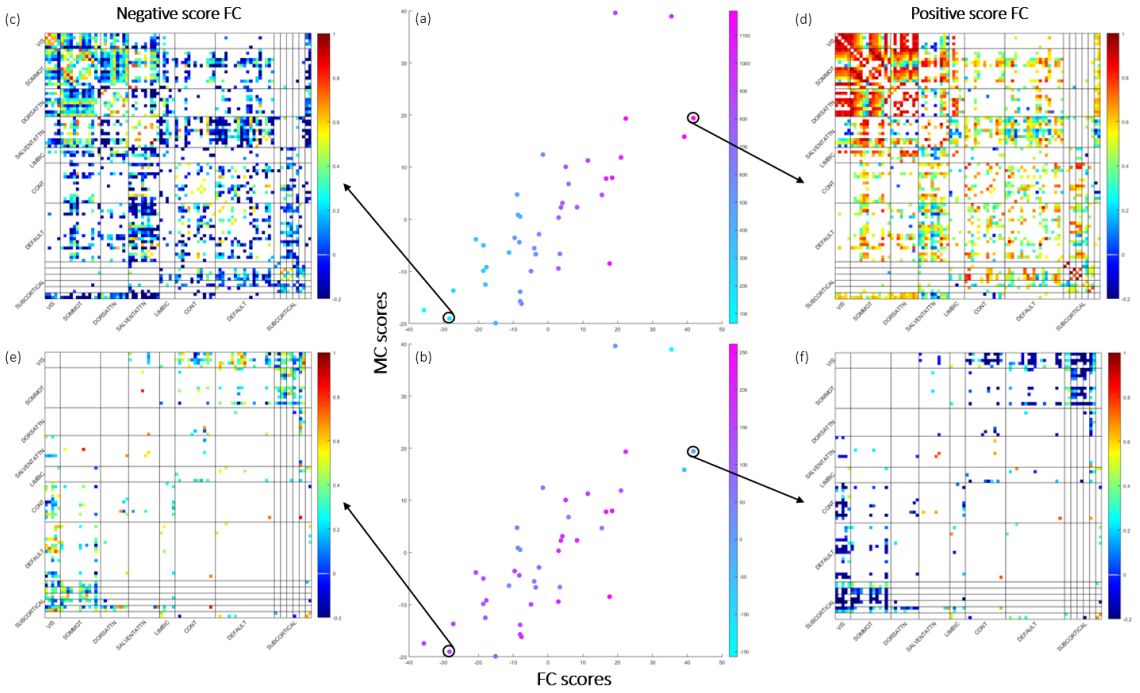

Figure 3.10: *In the top panel, scatterplots illustrate the scores of healthy subjects, where each score is weighted by the sum of the FC entries corresponding to positive (a) and negative (b) salience of FC. Increasing sum values are shown with colours ranging from light blue to magenta. Overall, a higher sum value corresponds to a subject with a positive score (d) when the salience is positive (a) and negative (e) when the salience is negative (b); conversely, lower sum values correspond to lower scores. The bottom panel shows matrices of FC, masked to consider only the entries associated to positive (c, d) and negative (e, f) salience.*

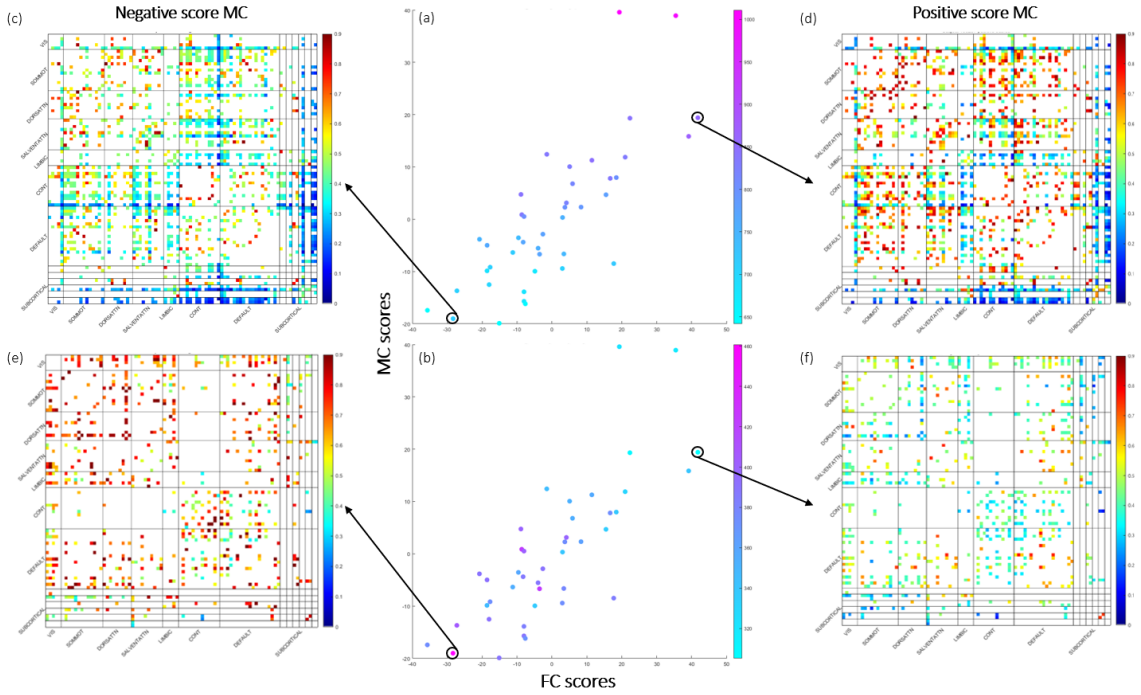

Figure 3.11: *In the top panel, scatterplots depict the scores of healthy subjects, with each score being weighted by the sum of MC entries corresponding to positive (a) and negative (b) MC salience. Increasing sum values are represented by colours ranging from light blue to magenta. Generally, a higher sum value corresponds to a subject with a positive score (d) when the salience is positive (a) and negative (e) when the salience is negative (b); conversely, lower sum values correspond to lower scores. The bottom panel displays matrices of MC, masked to include only the entries associated with positive (c, d) and negative (e, f) salience.*

After this single-subject analysis, the shared significant saliences between FC and MC were examined, leading to a group-level analysis aimed at identifying the regions with the most influence on the coupling between FC and MC.

Below is Figure 3.12, which shows the mask of significant saliences shared between FC and MC (a), along with the percentage distribution (based on the number of significant saliences in each network) of concordant (in red) and discordant (in green) saliences in each network (b). Then, the average matrices of FC (c) and MC (d) of healthy subjects are shown, masked by the mask (a). From the observation of these results, a difference in the localization of saliences has emerged: although in all networks, except the LIMBIC, the number of discordant saliences is lower than that of concordant ones, the latter are mainly localized in the SALVENTATTN, CONT, DMN and SUBCORTICAL networks, while they are more balanced with discordant ones in the unimodal networks. The masked average matrices highlight the different connectivity patterns that have emerged previously, namely higher FC values especially in the unimodal networks and lower

values in the uni-transmodal associations, as well as higher MC values overall, both in unimodal networks and between uni- and transmodal networks.

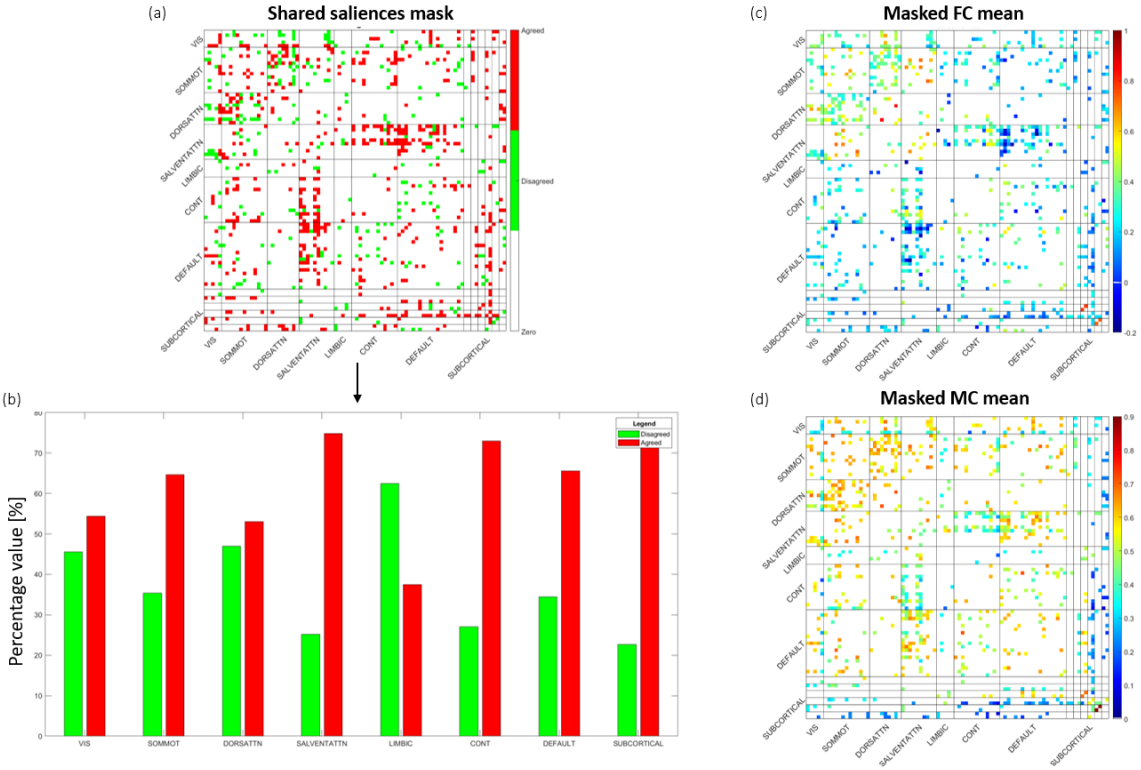

Figure 3.12: *Group-level investigation of the FC-MC coupling. (a) Matrix of common saliences between FC and MC, with red values indicating concordant saliences, green for discordant, and white for non-significant ones. (b) Barplot showing the number of concordant and discordant saliences in each network, percentage-wise based on the total number of significant saliences in the respective network. (c) Average matrices of FC (c) and MC (d) obtained considering the entries corresponding to the common saliences between the two, highlighted in (a).*

However, it is noteworthy that both in the pattern of common saliences and in the corresponding mean values of FC and MC, differences emerge within the same network between the two cerebral hemispheres (left parcels are listed before right parcels within the network). To further investigate this variation, topographic maps of the saliences shared by FC and MC are presented in Figure 3.13.

From the following figure, it is indeed clear that, overall, even when considering the division between the hemispheres, concordant saliences (on the left) have a greater magnitude compared to discordant ones (on the right), as previously highlighted in the bar plot of Figure 3.12b. Furthermore, there is a definite complementary localization of concordant and discordant saliences between the two hemispheres, i.e., where concordant saliences are more prevalent, discordant saliences are less so, and vice versa. Looking

more closely at the parcels, it becomes evident that, in general, more concordant saliences between FC and MC are located primarily in the frontal part of the left hemisphere and in the left thalamus, while in the right hemisphere they are more concentrated in the occipital lobe and in subcortical regions such as the right pallidum and hippocampus. Conversely, salience tends to be more disagreed in the left posterior temporal and subcortical regions (such as the cerebellum and hippocampus) and in the deeper insular regions of the right temporal lobe.

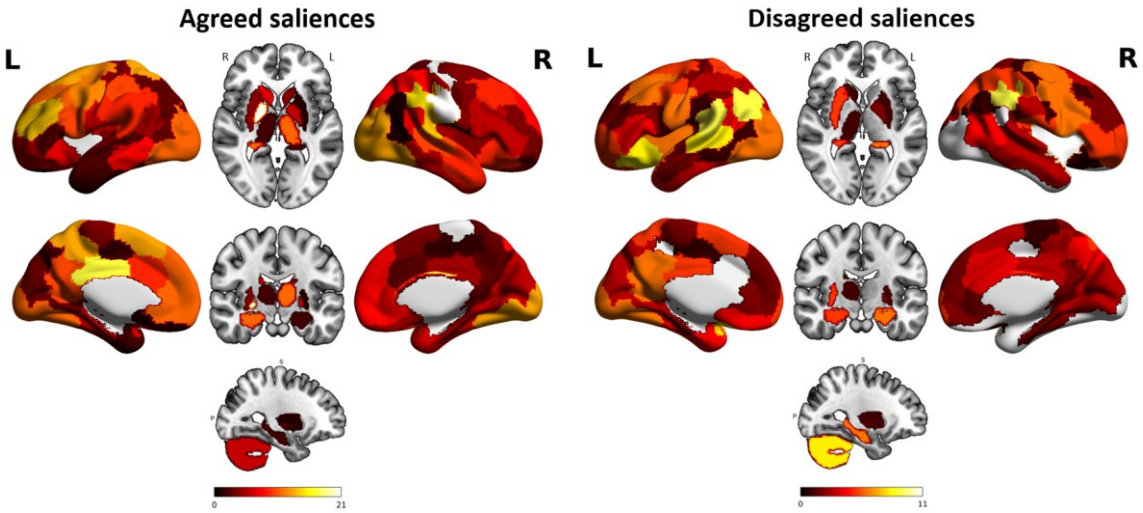

Figure 3.13: *Topographical distributions of the concordant (left) and discordant (right) common significant FC and MC saliences. The number of concordant (or discordant) saliences in a parcel is indicated by the colorbar, with lower values tending towards dark red and progressively lighter yellow shades indicating higher values. In both sides, the outer maps display cortical regions, while the inner maps depict subcortical regions. Hemisphere orientation is reversed in the visualization of subcortical regions, as indicated by the letters "L" and "R" in the figure.*

3.3 Projection of oncological scores on HCs latent space

By projecting the features of each oncological patient onto the latent spaces, three completely different scenarios describing the decoupling induced by the lesion were uncovered. The results obtained in the different pairs considered are explained in the following paragraphs, in the same order as presented in the previous section.

3.3.1 K_1- FC_{STR} decoupling

In the case of the K_1-FC_{STR} pair, as shown in Figure 3.14, some patients (highlighted by red data points) deviate significantly from the expected metabolic-functional coupling. Notably, there appears to be a moderate relationship between the degree of deviation and the volume of the lesion, as suggested by the marker size.

Consequently, by creating a tumour-weighted frequency map derived by combining the individual frequency maps of the out-patients through a weighted sum, it was possible to identify the lobe of the lesion based on the pair under consideration. As can be seen from the regions where the group-level tumour frequency maps achieve the highest values (indicated by colours tending toward orange/yellow), the K_1-FC_{STR} pair decoupling predominantly highlights tumours located in the frontal lobe, with a widespread distribution on the right side, and in a more localized frontoparietal areas on the left side.

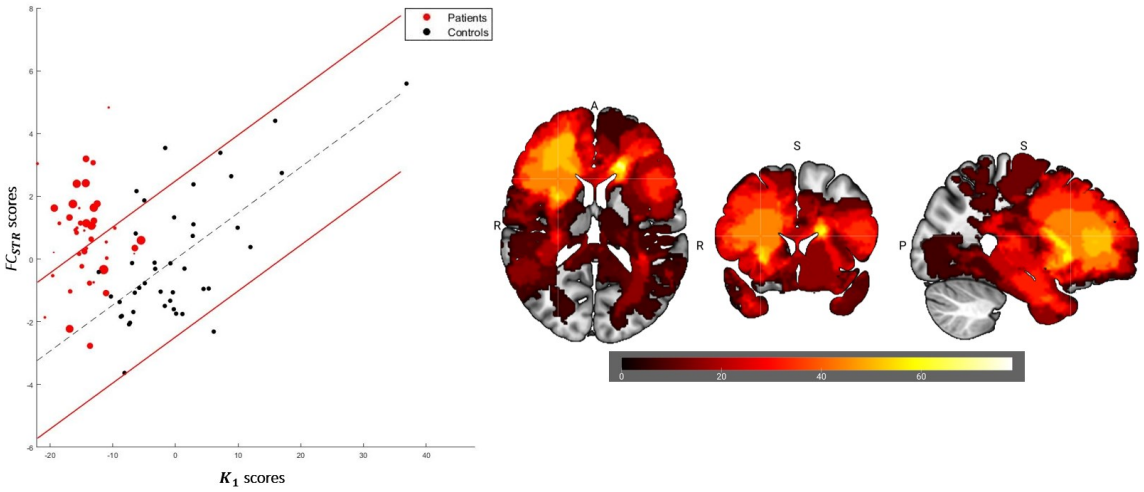

Figure 3.14: *Patient's latent points are projected onto the K_1-FC_{STR} latent space shown in Figure 3.6. Oncological subjects are represented by red dots, while healthy controls are depicted as black dots, consistent with Figure 3.6. For patients, the size of the markers corresponds to the volume of the lesion. Alongside the scatterplot, the corresponding tumour weighted frequency map is provided, derived from combining individual frequency maps of the out-patients through a weighted sum. Hemisphere orientation is reversed in the visualization, as indicated by the letters "L" and "R".*

3.3.2 *SUVR- FC_{STR}* decoupling

Also for the *SUVR-FC_{STR}* pair, as shown in Figure 3.15, certain patients (highlighted by green data points) show significant deviations from the linear metabolic-functional pattern observed in healthy subjects. In contrast to the K_1-FC_{STR} pair, no significant correlation was found between the magnitude of the deviation and the lesion volume, as indicated by the marker size in Figure 3.15. Although higher values of tumour-weighted frequency maps are observed in the right parietal lobe in this case, the maps overall show widespread values throughout the cortex, suggesting that the *SUVR-FC_{STR}* pair lacks robustness to precisely localize tumours in the presence of metabolic-functional decoupling.

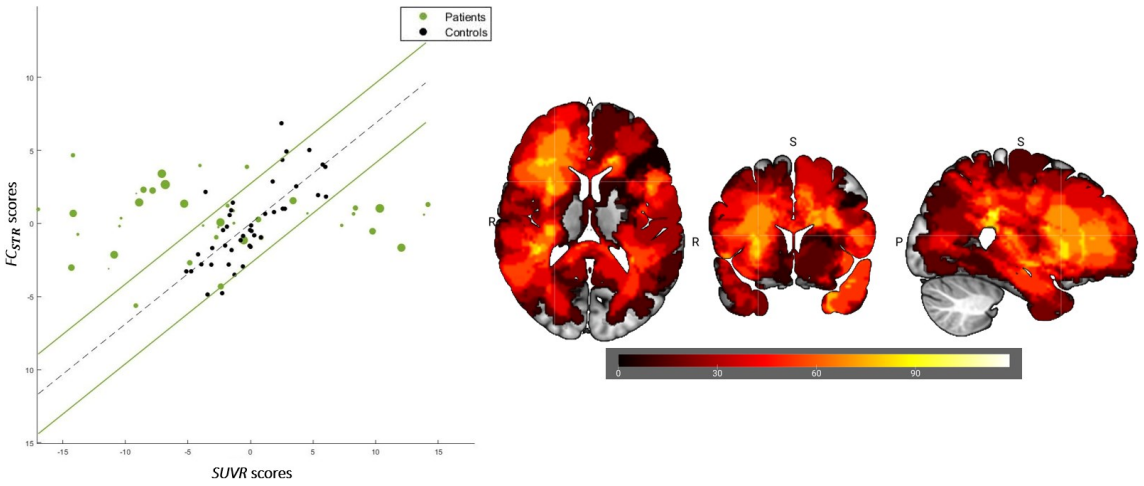

Figure 3.15: *Patient's latent points are projected onto the SUVR-FC_{STR} latent space shown in Figure 3.7. Oncological subjects are represented by green dots, while healthy controls are depicted as black dots, consistent with Figure 3.7. For patients, the size of the markers corresponds to the volume of the lesion. Alongside the scatterplot, the corresponding tumour weighted frequency map is provided, derived from combining individual frequency maps of the out-patients through a weighted sum. Hemisphere orientation is reversed in the visualization, as indicated by the letters "L" and "R".*

3.3.3 FC-MC decoupling

Considering the insights gained from the FC-MC pair analysis in control subjects, the topology of the patient's functional and metabolic connectivity matrices in F_2 band was explored before projecting the patient's latent scores onto the HC's latent space. This preliminary analysis assessed not only the differences between patients and healthy subjects, but also the variations between patients, given their significant heterogeneity in lesion localization and volume.

In particular, in patients with frontal lobe lesions (Figure 3.16 a, b), there is a clear reversal in the coupling between FC and MC. That is, a decrease in FC values (compared to the average values of control subjects, as shown in c) is associated with an increase in MC values (compared to the average values in d), and vice versa. This phenomenon is mainly observed in unimodal areas and in the connections between unimodal and transmodal areas, especially between DEFAULT and SALVENTATTN. Conversely, in patients with lesions localized in the parietal-temporal-occipital lobes (Figure 3.16 e, f), there is a widespread decrease in both FC and MC values (compared to the average values in c and d), particularly evident in connections within the DORSATTN network, both internally and with unimodal networks. On the contrary, an increase in FC, localized in some intra-transmodal and trans-unimodal connections, is associated with a rather widespread

increase in MC between networks, especially in the transmodal networks and their connections with certain subcortical regions (pallidum, cerebellum, and hippocampus).

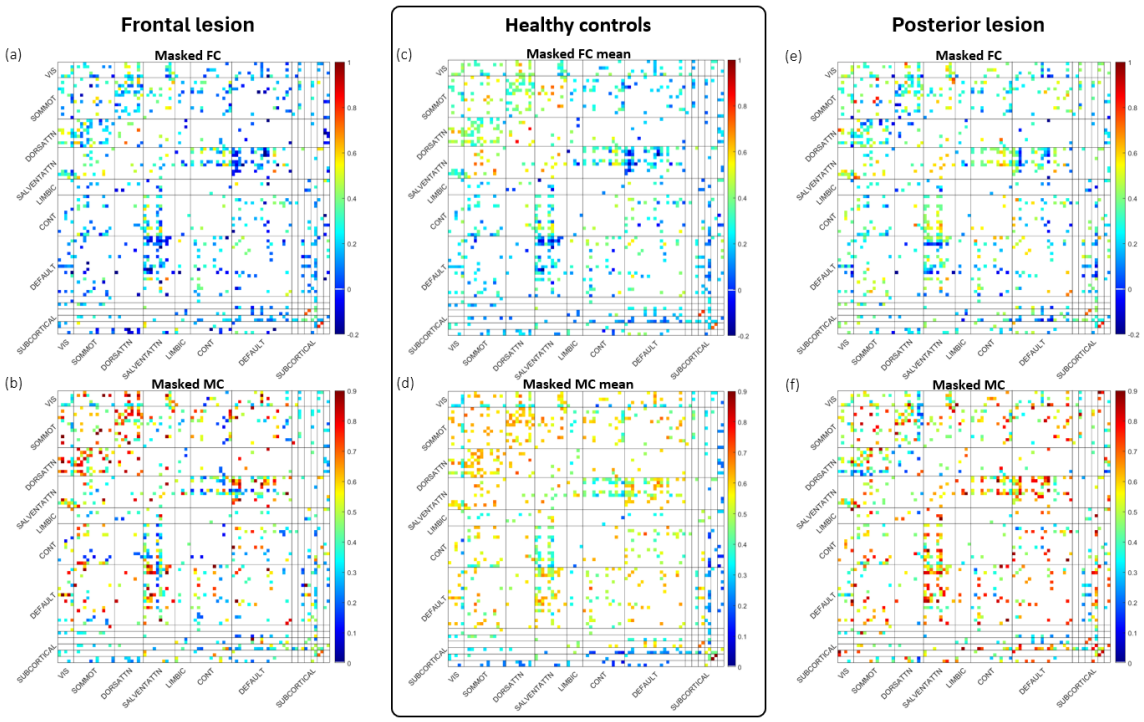

Figure 3.16: *Comparison of average functional and metabolic connectivity matrices of control subjects (c, d) with the corresponding FC and MC matrices of a patient with a frontal lobe lesion (a, b) and a patient with a more widespread lesion across the parietal-temporal-occipital lobes (e, f). The FC matrices considered belong to the F_2 frequency band. All matrices shown were masked to include only entries corresponding to common saliences between FC and MC patterns.*

Moving to the analysis of the results concerning the projections of the patient's latent scores onto the HCs latent plane, in the case of the FC-MC pair, Figures 3.17 and 3.18 show that in both frequency bands F_1 and F_2, only a few patients (highlighted by purple (F_1) and blue (F_2) data points) exhibit significant deviations from the expected functional-metabolic coupling compared to the other two previous cases. Furthermore, no significant correlation was observed between the degree of deviation and the lesion volume, as indicated by the marker size in the figures below. However, an inversion of the linear relationship between functional-metabolic scores can be observed in both frequency bands. Specifically, by calculating the Pearson correlation coefficient, along with the corresponding p-value, between the patient's FC and MC scores, a significantly negative value (albeit of moderate magnitude) was obtained, amounting to -0.3147 (p-value=0.04)

and -0.3347 (p-value=0.03) for bands F_1 and F_2, respectively. The related scatterplots are shown in Figure 3.19.

Moreover, as can be seen from the areas where the group-level tumour frequency maps reach peak values, the decoupling of both FC-MC pairs predominantly emphasizes tumours located in the frontal lobe, with a more precise localization in the right hemisphere compared to what is observed with the decoupling between K_1-FC_{STR}.

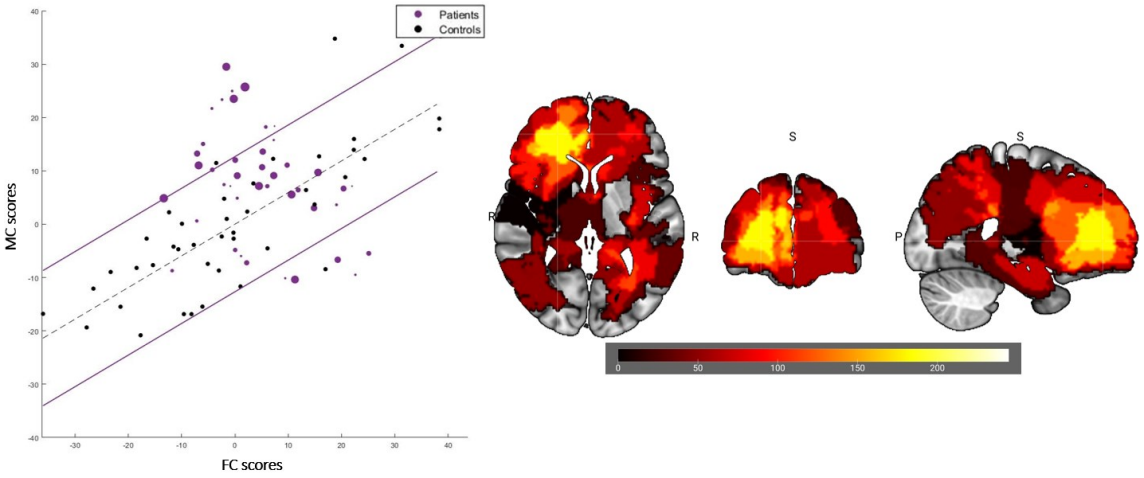

Figure 3.17: *Patient's latent points are projected onto the FC-MC latent space in F_1 shown in Figure 3.8. Oncological subjects are represented by purple dots, while healthy controls are depicted as black dots, consistent with Figure 3.8. For patients, the size of the markers corresponds to the volume of the lesion. Alongside the scatterplot, the corresponding tumour weighted frequency map is provided, derived from combining individual frequency maps of the out-patients through a weighted sum. Hemisphere orientation is reversed in the visualization, as indicated by the letters "L" and "R".*

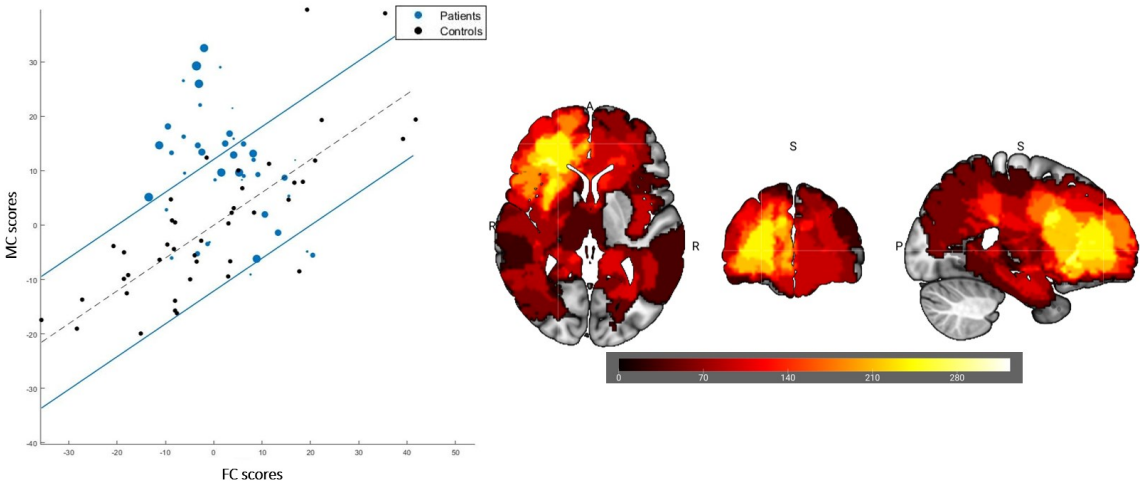

Figure 3.18: *Patient's latent points are projected onto the FC-MC latent space in F_2 shown in Figure 3.9. Oncological subjects are represented by blue dots, while healthy controls are depicted as black dots, consistent with Figure 3.9. For patients, the size of the markers corresponds to the volume of the lesion. Alongside the scatterplot, the corresponding*

tumour weighted frequency map is provided, derived from combining individual frequency maps of the out-patients through a weighted sum. Hemisphere orientation is reversed in the visualization, as indicated by the letters "L" and "R".

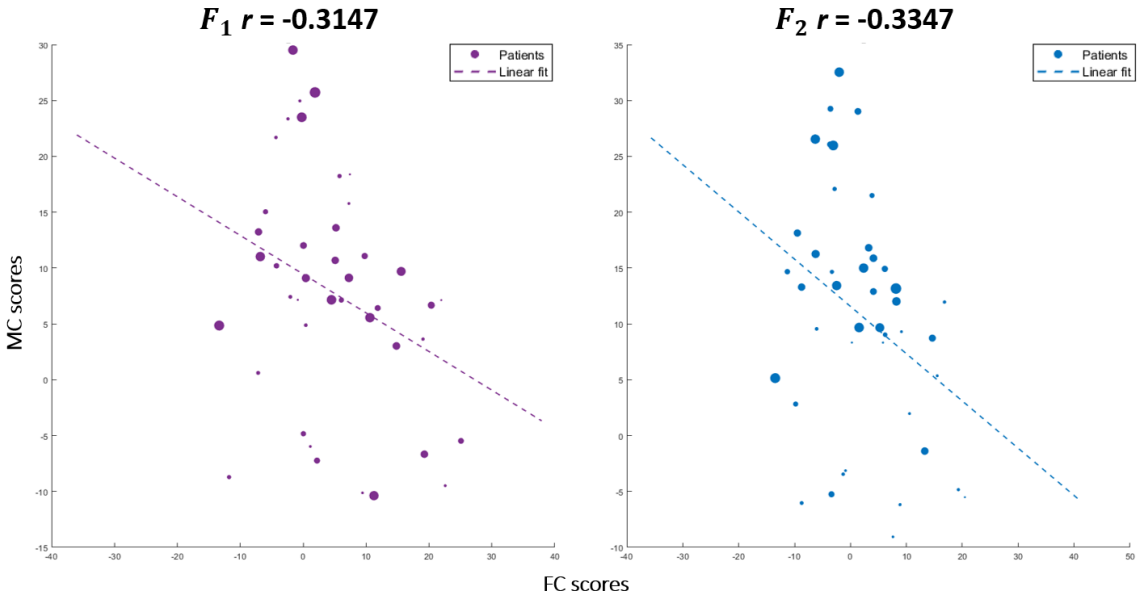

Figure 3.19: *Inversion of the FC-MC score relationship in oncological patients, observed in both F_1 (left) and F_2 (right) frequency bands. Calculating the Pearson correlation coefficient and corresponding p-value between the patient's FC and MC scores revealed a moderately significant negative correlation, with coefficients of -0.3147 (p-value=0.04) for F_1 and -0.3347 (p-value=0.03) for F_2. Oncological subjects are represented by coloured dots and the size of the markers corresponds to the volume of the lesion. In the scatterplot, the corresponding linear fitting of the FC and MC scores is also visualized, highlighted by a colour dotted line.*

Thus, it can be concluded that among the two FC-MC pairs in the frequency bands, the one that showed the most evidence of decoupling reversal between the functional and metabolic connectivity patterns was the F_2 band, where the magnitude of the correlation was highest, and the p-value was lowest (most statistically significant).

Chapter 4

Discussion

The interplay between metabolic and neural processes is critical for maintaining the adaptability of the human brain during complex cognitive tasks [177]. This study explores the intricate relationship between glucose metabolism and functional network communication, focusing on the functional-metabolic link. Specifically, it examines how glucose kinetics affect the strength of relationships within and between functional networks, shedding light on differences in metabolic support for ROIs based on their role in brain signalling. In addition, associations between functional and metabolic matrices are explored at the level of interactions between and within networks, providing insight into the influence of tissue metabolic properties on patterns of communication and synchronization between brain areas. Also, insights are provided into how the nature of functional-metabolic (de)coupling varies depending on the anatomical location of tumours. This finding highlights the potential impact of glioma progression in inducing multimodal dysfunction associated with neuroplasticity phenomena [178]. Through these analyses, a deeper understanding of the complex interplay between metabolic processes and functional interactions in the brain is sought, providing valuable insights for both neuroscience research and clinical applications.

4.1 Functional and metabolic patterns at group-level

The functional (Figure 3.2, 3.3) and metabolic patterns (Figure 3.1, 3.4) at group level confirm the close relationship between cerebral blood flow and neural metabolic activity [179] [180], [181]. In line with these studies, brain regions associated with more active cognitive functions, such as the medial occipital cortex and putamen, exhibit higher K_1 and k_3 values, reflecting increased blood flow and faster radiotracer incorporation into brain cells, respectively. The PCC and RSC, with elevated K_1 values, are key “hubs” of the DMN, central to its function due to extensive interconnections with other DMN regions. During rest or when not focused on external tasks, these regions display synchronized metabolic activity alongside other DMN components [176]. The observation of lower k_3 and K_i values in the cerebellum, coupled with the uniform

distribution of k_3 in other brain regions, suggests differences in metabolic efficiency between different brain areas, higher in the cerebellum compared to the cortex, in line with Tomasi (2017) [120]. The distribution of K_1, k_3, and K_i values in regions involved in neural networks, such as the visual network and the DMN, suggests that these networks play a critical role in regulating cerebral blood flow and neuronal metabolism. These networks are known to play a central role in complex cognitive processes such as attention, memory, and information processing, and their activity is closely correlated with cerebral perfusion and metabolism. The presence of interhemispheric differences in K_1, k_3, and K_i values suggests a lateralization of brain functions, albeit to a modest extent. However, the symmetry observed in *SUVR* values between hemispheres may indicate bilateral regulation of glucose consumption, underscoring the importance of metabolic balance for cognitive functions [182], [183].

The results obtained from the parameters K_1, k_3, and K_i, and *SUVR* can be related to those found in the FC and MC matrices, which highlight the presence of robust and well-organized functional connections, with high modularity and clear distinction between unimodal and transmodal networks. Before analysing connectivity patterns, it's crucial to clarify two fundamental concepts in neuroscience: integration and segregation. Integration involves specialized brain regions collaborating to process complex information and support higher cognitive functions, enabling long-range synchronization. Segregation, conversely, involves distinct brain regions specializing in specific functions while maintaining their autonomy. Both FC and MC matrices emphasize homotopic interhemispheric connections, indicating coordinated activity and balanced metabolic function between corresponding brain regions, also consistent with symmetric *SUVR*. The FC matrices show a block structure with limited connections between different networks, reflecting functional segregation, in line with the anticorrelated activity observed between unimodal and attentive/cognitive networks [176]. This reflects the functional segregation between these types of networks, similar to the observed differences in K_1, k_3, and K_i, and *SUVR* values across different brain regions. Similarly, the high intra- and inter-network connectivity values in unimodal regions (e. g., VIS, SOMMOT) and specific areas of transmodal networks (e. g., frontal regions of DMN, temporal areas of DORSATTN), as observed in MC matrices, indicate functional specialization within different brain networks and the presence of dynamic modulation of neuronal activity. According to

Volpi (2022), factors such as high neuronal density, intense synaptic activity, and high energy demands may contribute to increased metabolic connectivity in these brain regions [108]. The observed disconnection of certain regions, such as the limbic network and subcortical areas, from the rest of the connectivity pattern in the FC and MC matrices underscores their unique functional roles and connectivity profiles. This is in line with the lower metabolic activity and glucose consumption levels observed in regions such as the cerebellum and subcortical ROIs in the *SUVR* analysis. These regions, while less connected in the overall network, play critical roles in mediating specific cognitive processes or regulating network dynamics, reflecting a diversified functional contribution of these regions to complex cognitive functions. Furthermore, the observed discrepancies in functional connectivity values across frequency bands imply dynamic shifts in network organization and information processing. These variations, predominantly observed in limbic and subcortical regions, may be due to differences in the computational demands of cognitive activities, highlighting the intricate interplay between structural connectivity, functional connectivity, and metabolic demands [184]. Particularly, the lower values observed in the 0. 008-0.21 Hz frequency band could be attributed to the presence of slow hemodynamic functional information. Thus, regions like the limbic system and thalamus, which are less active during slower hemodynamic processes, may have a greater impact on functional connectivity at lower frequencies compared to higher ones.

4.2 Generalizable functional-metabolic pairs

By comparing local and network measures of brain metabolism with network patterns of functional flow, a dual functional-metabolic coupling was revealed. The observed relationship between the strength of functional connectivity and regional metabolic parameters (K_1, k_3, K_i, and *SUVR*) suggests that local energy supplies support the amount of functional communication and/or interaction at the ROI level. In addition, PLSC analysis revealed a close coupling between FC and MC matrices, suggesting that the functional system is supported by metabolic sources regulated at the network level.

Furthermore, an attempt was made to address the issue of intra-individual differences in parameters K_1, k_3, K_i and *SUVR* by further intra-individual z-scoring prior to PLSC analysis. However, it turned out that this step was unnecessary as the normalization across individuals was sufficient to obtain reliable results; indeed, all generalizable pairs were without intra-individual z-scores.

An important initial finding from the analysis conducted is the lack of a generalizable coupling between the strength derived from FC and the kinetic parameters k_3 and K_i (red rows in Table 3.1). There could be several reasons for this result, as discussed below. Kinetic parameters such as k_3 and K_i reflect rapid biochemical processes related to tracer phosphorylation and uptake that occur over relatively short time scales (in contrast to the parameter K_1, which have typically higher values). On the contrary, functional connectivity measures the temporal correlation of neural activity over longer periods of time, often minutes or longer. Thus, the differences in temporal dynamics between these processes may result in limited coupling between them. Furthermore, the processes represented by k_3 and K_i, may not be directly related to the functional interactions between brain regions captured by FC matrices. While both reflect aspects of brain function, they operate at different biological levels and may not have direct causal relationships with each other. Given the complexity and dynamic nature of the brain, with multiple interactions between different factors and neural processes, it is possible that the metabolic parameters k_3 and K_i do not fully capture the complexity of the relationship between metabolism and functional connectivity, or that there are other unconsidered factors influencing this relationship. Moreover, the estimation and measurement of kinetic parameters and functional connectivity involve different techniques and methodologies, each with its own sources of variability and limitations. Consequently, the measures used to assess FC and metabolic parameters may not be sensitive or accurate enough to detect subtle relationships between them, leading to discrepancies or lack of coupling between the measures. In fact, the regulation of tracer uptake and metabolism may be influenced by factors other than functional connectivity, such as vascular or metabolic factors, which could further complicate the relationship between kinetic parameters and FC strength [21], [185].

4.2.1 K_1-FC$_{STR}$ pair

The PLSC analysis identifies a significant relationship between ROI-level measures of K_1 and FC strength in each subject, observed across both frequency bands. Particularly, the correlation between the scores L_x and L_y is stronger when considering FC strength derived from the frequency band containing slower BOLD signal fluctuations, which contains more hemodynamic information. This close coupling, detailed by Amend and colleagues (2019), is explained by the bolus injection of the tracer, where the K_1 constant,

reflecting tracer distribution from the bloodstream, is more closely related to FC the F_2 band, since both data modalities contain hemodynamic contributions [186]. Indeed, studies have reported prominent metabolic correlations during the early phase of bolus injection-based PET measurements, further emphasizing the dependence of [^{18}F]FDG and rs-fMRI signals coupling on the glucose transport rate K_1 [120]. Additionally, the research of Storti et al. (2017) suggests a relationship between arterial spin labelling (ASL) and concomitant BOLD (ccBOLD)-based betweenness centrality (BC) in key regions and baseline perfusion, indicating significant influence of highly perfused tissue on information transfer through the network under the assumption that item transfer follows the shortest paths [187]. In addition, Liang et al. (2013) demonstrated a robust association between regional cerebral blood flow (rCBF), used as a surrogate for cerebral metabolism, and resting-state functional connectivity. They found that regions with high rCBF during rest, including those within the DMN and visual areas, overlapped with functional hubs, indicating a close link between metabolic demand and network connectivity. The greater association between blood supply and functional connectivity organization in higher-order brain systems, such as the DMN and subcortical areas, underscores the intricate relationship between metabolic demands and network dynamics [188]. It's possible to recognize these findings also in the salience's pattern (Figure 3.6), since the positive coupling between K_1 and FC_{STR} is observed in regions such as the PCC, RSC, inferior-parietal and temporal areas of the DMN and in the VIS network, underscoring the significance of metabolic demand in shaping functional connectivity patterns [21]. This outcome aligns with prior research suggesting that regions with higher glucose transport often exhibit stronger functional connectivity, indicative of their involvement in information processing and integration with other brain areas [189]. However, the discrepancy between K_1 and FC_{STR} saliences in LIMBIC and CONT networks suggests a more nuanced relationship between metabolic activity and functional connectivity. While some regions demonstrate a strong alignment between the two measures, suggesting optimizing functional connectivity for efficient information processing at the expense of high energy consumption, others show a dissociation, indicating that additional factors may modulate functional connectivity patterns independently of metabolic activity or prioritize metabolic energy conservation through local functional hubs [188]. This divergence may reflect the complex interplay between

various neurobiological factors, including neurotransmitter systems, structural connectivity, and neuronal dynamics, all of which contribute to the organization of functional brain networks [25].

From the analysis of the corresponding K_1-FC_{STR} latent scores (Figure 3.6c), it is possible to distinguish two categories of individuals contributing to the variance of the component. The first category comprises those with positive latent scores, characterized by predominantly positive K_1 values throughout the brain. These individuals exhibit high FC_{STR} in unimodal, posterior parcels of DMN, and thalamic networks, while displaying lower FC_{STR} in high-order areas such as the limbic and control networks. The second category consists of individuals with negative latent scores, exhibiting predominantly negative K_1 values compared to the group's mean and high FC_{STR} in cognitive networks (limbic and control). This demonstrates the existence of a linear relationship between the tracer influx rate and the strength of functional interaction with other brain regions. Specifically, the strength of the FC matrix quantifies the intensity or level of synchronization in neural activity between pairs of brain regions, providing a deeper interpretation of a node's importance in the communication pattern among brain areas. Higher strength values indicate stronger functional connections, suggesting a greater degree of coordinated activity between those regions, interpreted as being functionally related or involved in similar neural processes. Conversely, lower strength values indicate weaker or less synchronized functional connections. Based on this, a distinction emerges between the two groups of individuals: in the first group, high-order networks showing lower strength values are characterized by higher K_1 values compared to the remaining areas, while in the second group, these networks have stronger functional importance with lower K_1 values. Therefore, a reversal of the node's importance is associated with lower K_1 values (if it is more integrating) or higher K_1 values (if it is more segregating).

This finding is consistent with the more flexible and context-dependent activity of the high-order areas, leading to greater temporal variability in their functional interactions. Additionally, limbic regions are involved in emotional regulation and affective processing, thus weaker functional connectivity in these regions may reflect their more variable and contextual nature of activation, necessary to respond to evolving emotional challenges [51].

Thus, it can be concluded that regions within high-order networks showing lower FC strength but higher K_1 values are characterized by elevated metabolic activity. This suggests that despite their lower functional connectivity strength, these regions may play a more integrative role in coordinating neural activity or supporting cognitive processes. Conversely, networks showing slower influx rate of the radiotracer into brain tissue and thus reduced metabolic activity, have stronger functional importance, indicating a specialization or segregation of function within these networks.

Therefore, by examining the interplay between FC strength and K_1 values, it is possible to gain insights into both the functional importance of brain regions and their metabolic demands. This provides a more comprehensive understanding of how brain networks are organized and how different regions contribute to overall brain function Also, the identification of distinct subgroups based on latent scores further underscores the heterogeneity in the relationship between K_1 and FC_{STR} across individuals. This variability emphasizes the importance of considering individual differences in metabolic and functional connectivity profiles, as these differences may have implications for understanding brain function and dysfunction on an individual level [156]. This is consistent with the chosen PLSC approach that conducts an analysis at subject level and with the non-generalizable results obtained with the further intra-individual z-score that eliminates these crucial differences.

4.2.2 *SUVR*- FC_{STR} pair

The second generalizable pair highlighted by the PLSC analysis is between the ROI-level measures of *SUVR* and FC strength for each subject. Conversely to the previous coupling, it is noteworthy that this relationship emerged as significant only in the frequency 0.008-0.11 Hz, suggesting a closer relationship between these two measures at lower frequencies. In fact, low-frequency fluctuations in neural activity are associated with metabolism, supported by research indicating that spikes in activity correspond to glucose utilization [190] and that metabolic constraints limit high-frequency activity [191], [192]. Additionally, studies using magnetoencephalography (MEG) and electroencephalography (EEG) suggest that low-frequency fluctuations in alpha/beta power, which interact with higher frequencies [193], [194], are robust neurophysiological correlates of BOLD FC [195], [196], [197]. Therefore, the modest yet reliable correlation between *SUVR* and FC strength may depend on an interaction of factors including blood

flow and oxygen consumption, structural variables, local activity, and inter-regional synchronization at faster temporal scales than the K_1 -FC_{STR} relationship [122].

The findings from the analysis of salience maps in Figure 3.7 provide valuable insights into the relationship between *SUVR* and FC_{STR}. The distribution of *SUVR* saliences across different brain networks suggests varying levels of metabolic activity across regions involved in attention, executive control, sensory processing, and high-level cognitive functions. The observation of both positive and negative saliences in *SUVR* underscores the dynamic nature of brain metabolism, with regions exhibiting diverse metabolic demands depending on their functional roles within the brain network.

On the other hand, the alternation of positive and negative saliences within FC_{STR}, with a prevalence of negative saliences in unimodal networks compared to transmodal networks, highlights the differential functional connectivity patterns across distinct brain networks. The moderate coupling between *SUVR* and FC_{STR}, particularly in transmodal networks and the cerebellum, suggests a complex relationship between brain metabolism and functional connectivity. Regions exhibiting higher *SUVR* coupled with increased FC_{STR} may play a more integrative role in coordinating neural activity, whereas regions with lower *SUVR* but higher FC_{STR} may be involved in specialized functions within specific brain networks. These findings underscore the importance of considering both metabolic activity and functional connectivity in understanding brain function and organization.

The analysis of the corresponding *SUVR*-FC_{STR} latent scores also suggest two categories of subjects contributing to the variance of the component (Figure 3.7c). Subjects with positive scores exhibit an overall positive *SUVR* across the whole brain, associated with higher FC_{STR} in regions involved in attention and spatial perception and processing, and lower FC_{STR} in areas associated with high-level cognitive and behavioural functions. Conversely, subjects with negative scores are characterized by a predominantly lower *SUVR* coupled with higher FC_{STR} in high-level cognitive functions. These results are consistent with previous studies reporting the linear relationship between regional metabolism and FC strength [119], [122], reflecting what previously explained for the coupling between K_1-FC_{STR}.

Based on the neurophysiological meaning of the FC strength and *SUVR*, a distinction emerges between the two groups of individuals. In the first, high-level cognitive and behavioural areas showing lower strength values exhibit higher *SUVR* values, suggesting

that these regions are more segregated. Conversely, in the second group, these networks have stronger functional importance but lower *SUVR* values, indicating more integrative or functionally important regions and thus a reversal of the node's importance related to *SUVR* values. It is important to consider how these results align with findings from the previous section investigating the K_1-FC_{STR} coupling, emphasizing the dynamic nature of brain function, where regions may play different roles depending on the context or task demands, and the complex relationship between brain metabolism, functional connectivity, and cognitive functions.

However, it is necessary to clarify that the coupling between FC_{STR} and *SUVR*, compared to that with K_1, is of humbler magnitude across the entire brain network's topology (as also evidenced by the lower generalizability values of scores X and Y in Table 3.1). This finding has been widely reported in the literature by studies such as Sundar et al. (2020), Volpi et al. (2021, 2024), Palombit et al. (2022), and the most recent study by Li et al. (2024). The findings of Sundar and colleagues suggest that rs-fMRI blood flow fluctuations are superimposed on a larger blood flow baseline not captured by fMRI measurements, which ultimately determines overall energy expenditure in the brain. Despite the importance of oxygen and glucose delivery, the unknown blood flow baseline and the mechanisms underlying neurovascular coupling remain poorly understood [198]. Both Volpi et al. studies demonstrated a positive covariation between strength derived from static functional connectivity and *SUVR*, albeit moderate compared to other measures, indicating that local activity and synchronization are crucial predictors of glucose metabolism. However, non-linear relationships were observed between *SUVR* and most rs-fMRI features, with stronger associations observed at lower *SUVR* values [199], [200]. Palombit et al. reported that the moderate coupling between *SUVR* and FC strength is due to *SUVR*'s relative assessment compared to quantitative [^{18}F]FDG-PET analysis. An approach based on *SUVR* is therefore not able to disentangle the different physiological processes describing the kinetics of brain glucose consumption (which are better described by K_1), thus preventing a full understanding of its relationship with fMRI FC. Li et al. provided in vivo evidence that metabolic-functional associations occur not only in colocalized regions but also across long-range connections, emphasizing a diverse yet intimate relationship between metabolism and brain function [201]. These recent findings using multimodal analysis techniques, such as canonical correlation analysis

(CCA), closely resemble the analysis conducted within this dissertation using PLSC. Indeed, a general limitation of analyses performed in previous studies is that they are often conducted at the group level, thereby obscuring important details of the individual functional organization in terms of both FC and *SUVR*. Therefore, the subject-level PLSC analysis in this study was able to better explore the between-subject variability of these *SUVR-FC*$_{STR}$ associations across regions, as well as novel *SUVR-FC*$_{STR}$ associations across subject groups. In fact, the identification of two categories of subjects based on *SUVR* and *FC*$_{STR}$ scores further emphasizes the heterogeneity in brain-metabolism relationships. Subjects with negative scores, characterized by lower *SUVR* and higher *FC*$_{STR}$ in regions associated with high-level cognitive functions, may exhibit a distinct pattern of neural activity compared to those with positive scores, highlighting potential differences in cognitive processing and behaviour. This underscores the variability in the spatial relationship between functional and metabolic aspects across individuals, as highlighted by Volpi (2024): while for some individuals, glucose consumption was closely linked to the underlying spontaneous functional architecture, for others, it appeared to be largely independent of such data. Additionally, they observed a notable negative correlation between the strength of functional-metabolic coupling and participant covariates (such as weight, body mass index, body surface area, and insulin levels). Consequently, they hypothesized that variations in peripheral metabolism among individuals influence how glucose is utilized to meet the brain's functional demands, thereby impacting individual functional-metabolic coupling [200].

4.2.3 FC-MC pair

The third and fourth generalizable pair highlighted by the PLSC analysis are those between the edgewise level measures of FC and MC for each subject. It is noteworthy that this relationship emerged as significant in both frequency bands, suggesting a robust coupling between these two measures. This is because both frequency bands capture low-frequency BOLD signals relevant for functional connectivity analysis, reflecting neuronal activity and metabolic processes in the brain. Although there are slight differences in the correlations and generalizability values between F_1 and F_2, by examining multiple frequency bands, it becomes possible to gain comprehensive insights into the relationships between functional connectivity and metabolism across diverse neural networks and temporal scales.

An important result to highlight is that the agreement between FC and MC matrices is stronger, both in terms of correlation between scores and generalizability, compared to the agreement between FC strength and local metabolic parameters (K_I and *SUVR*). This finding is consistent with the results of Volpi (2021) and Li (2024). Specifically, Volpi et al. demonstrated the metabolic properties underlying "hubness" in the MC network may be inherently linked to a region's ability to connect with other regions, both locally and globally. This further underscores that the coupling between glucose metabolism and fMRI FC, which appears somewhat limited when considering only local metabolic measures such as *SUVR*, becomes stronger when both PET and rs-fMRI are considered within a large-scale connectivity framework [199].

In addition, Li et al. suggested that synaptic activity reflected by FDG uptake may influence ATP-requiring functions of remote or downstream regions and promote structural and pathological changes. This supports the idea that the stronger link between function and metabolism is not found in a localized analysis, but rather in a global, network-level analysis that considers the synchronization of functional and metabolic activity across structurally distant areas of the brain [201].

It is intriguing to explore the reasons for the correspondence between pharmacokinetic similarity between brain regions and FC. Therefore, a subsequent investigation of FC-MC coupling at a finer scale is reported and explained in detail.

After evaluating the pattern of FC and MC saliences (Figure 3.8 a, b and Figure 3.9 a, b) and latent scores (Figure 3.8 c and Figure 3.9 c), the investigation at the individual level has been conducted by masking the FC and MC original matrices with the significant saliences of FC and MC pattern separately. This step led to the identification of two main categories of subjects: the first group, associated with negative scores, consists of individuals with lower FC values in unimodal regions and integration with SALVENTATTN, corresponding to lower MC integration values between unimodal and transmodal regions, and higher values within CONT and DMN. Conversely, the second group, characterized by a positive score, includes subjects with positive FC connections and predominantly negative MC connections within the unimodal networks, along with positive MC connections facilitating greater integration between uni- and transmodal regions and less integration among the transmodal regions themselves. Also, in terms of MC, negative weights predominantly implicate the visual network and intra-network

blocks, highlighting a dual state of metabolic integration and segregation that characterizes these two groups.

Overall, therefore, from observing the FC and MC matrices of two extreme subjects masked for the significant saliences of FC and MC taken individually (Figures 3.10 and 3.11), it can be inferred that while the FC matrix is more segregated in unimodal areas, the corresponding MC is more integrated between uni- and transmodal networks. This could be explained by the fact that greater metabolic integration between uni- and transmodal areas is necessary for the functioning of unimodal areas. Conversely, when unimodal areas are less active (lower FC), there is also a reduction in uni-transmodal metabolic integration. However, despite this distinction between groups of healthy subjects, it is important to emphasize that the pattern of covariance between FC and MC remains the same for all, regardless of the score value. In fact, there is always a more segregated FC in unimodal areas, corresponding to a globally more integrated MC.

This important finding is consistent with the results of Volpi et al. (2024), who used two multimodal datasets from healthy participants to build a multivariable, multilevel model of functional-metabolic associations. They evaluated several functional features, including rs-fMRI signal, hemodynamic response, static and time-varying functional connectivity, as predictors of the metabolic architecture of the human brain. Among other significant results, they found that the temporal variability of FC (tvFC) was negatively associated with metabolism [200]. This suggests that metabolic consumption tends to be higher when functional connectivity remains stable over time, implying that maintaining stable FC is an energy-consuming process, as also suggested by Deng et al. (2022) [202]. Indeed, unimodal regions are characterized by more stable patterns of functional connectivity over time due to the extrinsic nature of these correlations, in contrast to transmodal networks, which are governed by faster and more labile interactions due to their high involvement in numerous intrinsic processes.

At this point, the analysis was shifted to group-level and then the contribution of each region to the coupling between FC and MC was examined, considering only the significant saliences common to FC and MC patterns (Figure 3.12).

Considering these results, the observed difference in the localization of saliences suggests varying degrees of functional-metabolic coupling across brain regions. Specifically, while most networks exhibit a higher number of concordant saliences compared to discordant

ones, the distribution of concordant saliences is notably prominent in regions such as SALVENTATTN, CONT, DMN, and SUBCORTICAL networks, whereas a more balanced distribution with discordant saliences is observed in the unimodal networks. The masked average matrices further illustrate distinct connectivity patterns, including higher FC values, especially in the unimodal networks, and lower values in uni-transmodal associations. Additionally, overall higher MC values are observed, both within unimodal networks and between uni- and transmodal networks (as already explained from the subject-level analysis).

Considering these results, the observed difference in the localization of saliences suggests varying degrees of functional-metabolic coupling across brain regions, that can be interpreted in relation to the functional specificity of the involved brain networks. Specifically, while most networks exhibit a higher number of concordant saliences compared to discordant ones, the distribution of concordant saliences is notably prominent in regions such as SALVENTATTN, CONT, DMN, and SUBCORTICAL networks, whereas a more balanced distribution with discordant saliences is observed in the unimodal networks (consistent with [119], [203], [204]). Instead, the difference between the limbic network and all the others is clearly visible, as it is the only one in which the percentage of discordant saliences is greater than that of concordant ones. This result can be explained by the complexity and diversity of cognitive functions involved in the limbic network, since it is associated with emotional, memory, and motivational processes [205]. Because these functions involve a wide range of neural circuits and can be influenced by various external and internal factors, it is plausible that the correlation between FC and MC is less consistent. For example, metabolic activity may be influenced by factors such as emotional state or attention, which may not directly reflect the observed functional connectivity during a particular state [206], [207].

On the other hand, networks such as SALVENTATTN, CONT, DMN, and SUBCORTICAL are more directly involved in specific cognitive processes and show greater coherence between FC and MC. For example, the DMN is associated with self-referential processes and mind-wandering, whereas the SALVENTATTN is involved in attentional selection and control processes [25], [208]. Because these networks have more specific and well-defined cognitive functions, their metabolic activity is more likely to be directly correlated with their functional connectivity during specific cognitive tasks.

Conversely, unimodal networks specialized for sensory processing, such as vision or audition, exhibit a balanced distribution between concordant and discordant saliences in their FC and MC pattern. In fact, these networks are highly specialized and show consistent patterns of FC and MC due to their predictable nature of sensory processing [22]. For instance, in the visual cortex, neurons are predominantly activated by visual stimuli, leading to similar patterns of neuronal activation across different individuals and contexts [209]. This consistency fosters a more predictable relationship between FC and MC, in line with the top-down modulation of unimodal networks described by Gazzaley et al. (2012). In fact, it has been demonstrated that this mechanism dynamically modulates neuronal excitability both in the presence of stimuli, i.e., during selective encoding of items to be remembered and selective retrieval of a memorandum, as well as in the absence of external stimuli, i.e., in expectation of items to encode or ignore and during maintenance of items during a temporal delay. Additionally, unimodal networks involve simpler processing tasks compared to higher-order cognitive network since they are primarily influenced by external sensory inputs rather than internal factors, resulting in a straightforward relationship between FC and MC within these networks [210].

The masked average matrices further illustrate distinct connectivity patterns, including higher FC values, especially in the unimodal networks, and lower values in uni-transmodal associations, coupled with overall higher MC values, both within unimodal networks and between uni- and transmodal networks.

Then the topographic maps of the saliences shared by FC and MC presented in Figure 3.13 clearly depict differences within the same network between the two cerebral hemispheres.

In particular, greater concordant coupling is observed in the left frontal and right occipital regions while discordant coupling is mainly located in the posterior and subcortical regions (particularly the cerebellum) on the left, as well as deep insular regions on the right. So far, studies have consistently reported stronger functional-metabolic associations in frontal regions compared to other brain regions [121], [122], [123], [186], [199]. Thus, these findings contribute novel information regarding the lateralization of this coupling, which has not been previously explored in the literature.

The localization of greater concordance in the left frontal lobe and the right occipital lobe may be attributed to their stable and repeated connectivity patterns over time, consistently

with findings in the analysis at subject level and coherent with Volpi (2024) [200]. In fact, these brain regions are involved in fundamental cognitive and sensory functions, which require consistent neural activity and metabolic support. The left frontal lobe, known for its involvement in language, planning, and executive functions [211], and the right occipital lobe, crucial for visual perception and object recognition [212], exhibit relatively stable functional connectivity due to the nature of their activities. Therefore, there might be greater concordance in functional-metabolic coupling in this region, as intense visual activity is associated with increased brain metabolism.

Conversely, the localization of greater discordance of saliences in the posterior and subcortical regions, particularly the left cerebellum, and deep insular regions on the right, may be linked to their highly specialized functions and the need for frequent metabolic shifts to support their diverse connectivity patterns. The cerebellum, involved in motor coordination and cognitive processes such as attention, language, and emotional regulation, may exhibit greater discordance in functional-metabolic coupling due to its diverse functions and extensive connectivity with various brain regions, including both cortical and subcortical structures [213]. Similarly, the deep insular regions on the right side, implicated in emotion processing, interoception, and autonomic regulation, must continuously adapt their metabolic demands to accommodate the variability of functional connections they engage in, particularly with limbic structures, such as the amygdala, and higher-order cortical regions [214]. Thus, the discordance in functional-metabolic coupling observed in these regions may reflect the intricate interplay between emotional processing and autonomic functions, which are known to modulate metabolic activity in response to environmental and internal cues. In summary, the localization of greater discordance in saliences in the posterior and subcortical regions on the left side, including the cerebellum, and deep insular regions on the right side, may be driven by the specialized functions and connectivity profiles of these brain regions, involving complex interactions between motor, cognitive, emotional, and autonomic processes.

However, it is essential to note that while these results provide valuable insights, further research is needed to fully understand the underlying mechanisms and implications of lateralized functional-metabolic coupling. This deeper investigation may offer new perspectives on brain organization and function, shedding light on the nuanced interplay between brain function and metabolism in different regions and hemispheres.

4.3 Projection of oncological scores on HCs latent space

In this scenario, the interplay between local coupling, which includes glucose influx rate and uptake with strength of FC, and network coupling, which involves functional and metabolic connectivity matrices, was investigated in glioma patients. This investigation was motivated by the hypothesis that perturbations in either coupling may provide valuable insights into the pathophysiological mechanisms underlying brain tumour progression. This choice was further supported by the emergence of the field of "cancer neuroscience", which seeks to elucidate the connections and interactions between neurons and gliomas, their impact on overall brain organization, cognition, neurological impairment, and, interestingly, tumour progression and prognosis [215].

Therefore, functional and metabolic variables were then estimated for patients and projected onto the maximizing covariance latent space (generalizable pairs only), identified in HCs.

4.3.1 K_1- FC_{STR} decoupling

For the K_1-FC_{STR} pair, Figure 3.14 shows that some patients (highlighted by red data points) deviate significantly from the expected metabolic-functional coupling.

The trend of the oncology patient's scores tends to be upward, with all K_1 scores being negative. Since the saliencies are common to healthy subjects, this implies that the K_1 values of the patients are all lower compared to the average of controls, resulting in negative scores. Therefore, there is a clear inversion of K_1 compared to controls, which is not observed in the same way for FC strength, as the scores for patients continue to vary within the same range. Consequently, there will be patients for whom a negative K_1 score corresponds to a positive FC_{STR} score, and since the saliences are common, this suggests that the decoupling between K_1 and strength is shifted more towards a variation in K_1 rather than FC_{STR}. In addition, it is observed that more patients deviate from the normal range of healthy subjects as the volume of their lesion increases, indicating that in these patients lower K_1 values correspond to almost positive FC strength values, probably due to pathological compensatory mechanisms at the whole-brain level and thus greater integration implemented by the brain in the presence of an extensive lesion [216]. This occurs in regions that have been shown to be significant in the coupling between K_1-FC_{STR} in controls.

Considering the greater weight given to patients further from the normality line, it is evident that this decoupling highlights more overlap in frontal regions, predominantly on the right side, because the group of patients had a lesion mostly localized in the right hemisphere rather than the left. Thus, it is interesting to note that this decoupling between K_1 and FC strength is crucial for the localization of frontal tumours rather than others. This could be due to the fact that these areas, as shown for HCs, are characterized by an inverse coupling in terms of K_1-FC_{STR} saliences, i.e. positive K_1 weights correspond to negative FC strength weights. This could mean that these areas, which already have an inverse coupling by nature, are more susceptible and sensitive to variations due to the presence of the tumour lesion, especially in terms of K_1, which in patients, as shown by the pattern of scores analysed above, tends to have lower values compared to the average of controls.

The findings of Orukari et al. (2018) suggested that gliomas induce local vascular dysregulation, characterized by increased CBF, elevated low-frequency power, and temporal lag relative to the unaffected hemisphere that confounds proximal FC measures. However, vascular dysregulation was not observed in regions remote from the glioma, suggesting that FC perturbations in these remote areas are likely driven by changes in neural activity rather than vascular factors. Thus, the results of this study highlighted a dual behaviour of FC in glioma patients, where local FC changes in networks proximal to the tumour occur due to hemodynamic alterations, while more distant FC changes are independent of vascular mechanisms [216]. Therefore, the observed decoupling between K_1 and FC_{STR} may reflect these aspects, as hemodynamic alterations, especially temporal delay, may be represented by patient's decreased tracer influx rate from bloodstream to. These abnormal K_1 values are associated with variations in FC_{STR} compared to the HCs, as evidenced by the fact that FC strength tends to remain positive at the local level despite significant hemodynamic alterations.

Overall, the observed differences in K_1 and FC_{STR} scores between glioma patients and healthy controls underscore the complex interplay between brain metabolism and functional connectivity in the context of glioma pathology. Thus, it can be concluded that lower K_1 values associated with almost "normal" FC strength values could be considered as potential biomarkers for the presence of a tumour lesion in the frontal lobe.

However, considering that FC can depict polysynaptic network communication, it is imperative to conduct a more comprehensive analysis using techniques capable of measuring direct, monosynaptic connections between regions, such as optogenetics. Such an approach would offer insights into how focal lesions distinctly impact network communication with greater precision [216].

4.3.2 *SUVR*- FC_{STR} decoupling

For the *SUVR*- FC_{STR} pair, Figure 3.15 shows that certain patients (highlighted by green data points) deviate significantly from the expected metabolic-functional coupling. However, consistent with the findings that reported a weaker coupling between *SUVR* and FC_{STR} with respect to that of K_1 and FC_{STR} in control subjects, also *SUVR*- FC_{STR} functional-metabolic decoupling is evident but less informative in glioma patients. Specifically, the scores do not show a well-defined trend, with *SUVR* values fluctuating significantly in both positive and negative directions and suggesting significant alterations in glucose metabolism in these patients compared to healthy controls. This could be due to the presence of the tumour itself, which may disrupt normal metabolic processes in the brain. Additionally, the stability of FC_{STR} scores within a consistent range indicates that functional connectivity remains relatively preserved despite metabolic changes. The prevalence of negative *SUVR* scores further highlights the pronounced decrease in glucose metabolism in glioma patients compared to controls. However, the lack of a clear relationship between *SUVR* and FC strength suggests that the coupling between metabolic and functional measures is weak and characterized by nonlinear associations. This weak coupling may be attributed to various factors, including the heterogeneous nature of gliomas, which can affect different brain regions differently, as well as compensatory mechanisms that the brain may employ to maintain functional connectivity despite metabolic disruptions. This highlights the even more complex interplay between functional dimensions and metabolic factors in glioma patients, that cannot be simply described by these two functional and metabolic measures at local level [177]. In addition, although higher values of tumour-weighted frequency maps are observed in the right parietal lobe, the maps show overall widespread values throughout the cortex, further suggesting that the *SUVR*- FC_{STR} pair lacks robustness in accurately localizing tumours in the presence of metabolic-functional decoupling.

4.3.3 FC-MC decoupling

Regarding the FC-MC coupling, it was initially interesting to note how the decoupling effect induced by the presence of the glioma is not influenced by the bandwidth change, consistent with what was found in the analysis of control subjects. This further demonstrates how investigating the relationship between function and metabolism at the network level is more robust than the analysis at local level, both from a physiological and pathological standpoint. Indeed, the preliminary analysis of the topology of patient's masked FC and MC matrices, considering only the entries corresponding to common saliences between FC and MC, has allowed not only the differences between patients and healthy subjects to be evaluated but also the variations between patients, given their significant heterogeneity in lesion localization and volume. In fact, it has already been demonstrated that tumour location appears to be crucial for network changes: while frontal and temporal tumours showed bilateral functional modifications, parietal and insular tumours appeared to display only local effects (functional changes in the left hemisphere notably) [217].

Indeed, from the visual analysis of these matrices belonging to two patients (Figure 3.16), a substantial difference in FC-MC decoupling between the patient with a lesion localized in the frontal lobe and the one with lesions involving more posterior parts of the brain (precisely parietal-temporal-occipital lesions) has emerged. More specifically, in the presence of a lesion localized in the frontal lobe with a significant volume, a decrease in FC values compared to the average values of HCs is associated with an increase in MC values, and vice versa. This phenomenon is mainly observed in unimodal areas and in connections between unimodal and transmodal areas, especially between the DMN and the SALVENTATTN networks. Such decoupling may reflect reduced functional integration in areas involved in attention regulation and basic cognitive functions. This suggests that the brain might be metabolically strained, increasing connectivity even between unimodal areas not typically involved in metabolic support in healthy subjects, potentially reducing the efficiency of metabolic pathways to support functional connectivity, albeit much reduced, between these areas. This is supported by the decoupling between K_1 and FC strength, where lower K_1 values still correspond to positive FC values, indicating that as K_1 decreases in patients, the efficiency of metabolic communication between brain areas also decreases, resulting in higher metabolic

connectivity in areas where functional connectivity is reduced (but still present). In addition, since it was known that this patient has a High-Grade Gliom (HGG), these findings further support the idea that HGG displayed decreased network connectedness, as already found in the study of Pasquini et al. (2022) [217].

Furthermore, these findings can be linked to the known Warburg effect, which describes the metabolic shift towards aerobic glycolysis observed in cancer cells, including glioma cells [218], [219]. This metabolic alteration results in increased glucose uptake and lactate production even in the presence of oxygen, providing the necessary energy and substrates for tumour growth and proliferation. In the context of gliomas, the Warburg effect can impact the brain's functional and metabolic connectivity. Increased metabolic demands of glioma cells may alter the brain's metabolic landscape, affecting both local and distant neuronal populations. Specifically, in regions directly affected by the glioma, such as those with lesions in the frontal lobe, the metabolic demands of the tumour may lead to a decoupling between FC and MC. The increased metabolic activity associated with tumour growth could result in higher MC values, while the disruption of neuronal networks due to tumour infiltration may lead to decreased FC values [220], [221]. This decoupling reflects the complex interplay between tumour metabolism, neuronal function, and brain connectivity.

Conversely, in patients with lesions localized in the parietal-temporal-occipital lobes, there is a widespread decrease in both FC and MC values, particularly evident in connections within the DORSATTN, both internally and with unimodal networks. However, an increase in FC values localized in some intra-transmodal and trans-unimodal connections is associated with a rather widespread increase in MC values between networks, especially in transmodal networks and their connections with certain subcortical regions (pallidum, cerebellum, and hippocampus). This decoupling may reflect the brain's attempt to compensate for the disruption of long-range connections, particularly within compromised attention control networks, utilizing alternative connections or cognitive resources to maintain the integrity of fundamental cognitive functions. This could be related to the findings of Pasquini (2022) in Low-Grade-Glioma (LGG) patients, since they demonstrated that LGG induce functional reorganization of the eloquent cortex within the same hemisphere, resulting in increased efficiency of the network. The increased global efficiency of the left hemispheric network in LGG patients

indicated higher inter-connectedness compared to HCs [217]. This aligns with previous studies by Derks et al., which reported increased connectivity between hubs and non-hubs in glioma patients compared to healthy subjects. Thus, these network modifications may be linked to intra-hemispheric functional reorganization, particularly within the language network, that is attributed to LGG slow growth rate, facilitating the development of plastic changes[159]. These findings supported the hypothesis of a beneficial intra-hemispheric reorganization in LGG, characterized by the recruitment of additional brain regions within the left hemisphere, leading to a shift from local to global efficiency [217]. These functional changes appear to be supported by a more widespread increase in metabolic connectivity (compared to that observed for a frontal tumour) among brain areas not involved in the tumour lesion. Indeed, regions belonging to the DORSATTN network and the connections between this network and other unimodal networks are significantly metabolically impaired, likely due to their closer proximity to the tumour lesion.

Overall, these findings could be considered in line with the results of Pasquini (2022) that showed mixed connectivity changes in the presence of frontal tumours while a decrease in all graph metrics in both LGG and HGG of both hemispheres in temporal tumour locations.

Then, considering the results of the projection of the patient latent scores onto the HCs latent plane, Figures 3.17 and 3.18 illustrate that in both frequency bands F_1 and F_2, only a few patients show significant deviations from the expected functional-metabolic coupling compared to what results from K_1-FC_{STR} and $SUVR$-FC_{STR} decoupling. Furthermore, no significant correlation was observed between the degree of deviation and the lesion volume (as indicated by the marker size). Instead, of interest was the clear inversion of the linear relationship between functional-metabolic scores, which was significant (albeit of modest magnitude) in both frequency bands and greater (in magnitude) for the F_2 band (Figure 3.19). This result further confirms what was previously inferred by simply observing the FC and MC matrices of two patients: the reversal in the relationship between FC and MC (lower FC where MC is higher, and vice versa), which is more evident in patients with a tumour localized in the frontal lobe, is consistent with recent literature findings from the study of Zimmerman et al. (2024) [222]. Indeed, they reported that peri-tumoral activity, which is most highly correlated with metabolic activity, was pathologically high in patients and that patients showed higher

clustering and lower centrality than controls. Their within-patient analyses revealed negative associations between regional deviations in brain activity and clustering, such that pathologically high activity (from a metabolic point of view) coincided with low network clustering (an index of reduced functional connectivity), whereas regions with "normal" activity levels showed high network clustering [222].

Moreover, as can be seen from the areas where the group-level tumour frequency maps reach peak values, the decoupling of both FC-MC pairs predominantly emphasizes tumours located in the frontal lobe, with a more precise localization in the right hemisphere (given that most patients had a tumour in the right hemisphere) compared to what is observed with the decoupling between K_1-FC_{STR}. This result is consistent with the effects of altered cerebral hemodynamic due to the presence of the glioma obtained for the decoupling between K_1-FC_{STR}. Furthermore, interestingly, the fact that this decoupling emphasizes frontal lesions further supports the hypothesis that the strongest relationship between functional connectivity and metabolism in terms of positive concordance occurs in the frontal regions of the brain. Indeed, the complex nature of cognitive functions in the frontal lobe may make it more sensitive to pathological changes associated with tumours. This may explain why the FC-MC pair is particularly effective in locating frontal tumours, since changes in brain networks in these regions may be more pronounced and thus more easily detected by FC and MC measurements.

Therefore, considering all the results obtained from the analysed pairs, both in physiological and pathological terms, it can be concluded that the pair that best describes and generalizes the relationship between brain function and metabolism is the FC-MC pair (in terms of entries from the upper triangular part). Indeed, this investigation at network level has shown consistent and robust behaviour in both frequency bands in which FC was obtained, supporting the idea that the function-metabolism link is not only to be found in the "canonical" frequency band of fMRI signals (0.008-0.11 Hz), but also by including parts of the BOLD signal at higher temporal scales that more strongly account for the contribution of the hemodynamic component (0.008-0.21 Hz). The more hemodynamic part of the BOLD signal is no longer negligible when studying its relationship with information about brain metabolism, since the latter is closely linked to the supply of glucose and oxygen contained in the bloodstream, which are necessary to guarantee the capacity to generate energy in the form of ATP molecules in the cells. In

fact, the presence of this contribution has proven to be decisive in determining a greater decoupling, in the form of a more significant negative correlation between patient scores, between the FC and MC matrices in the F_2 frequency band.

Chapter 5

Conclusions

The aim of this thesis is to assess the PLSC's ability to recognize covariation patterns between two distinct brain data modalities: functional data obtained from rs-fMRI and metabolic data from [^{18}F]FDG-PET scans.
This investigation is motivated by several gaps in existing literature:

I. Firstly, to test the applicability of PLSC, traditionally employed for variables related to brain activity and design/behavioural variables, to datasets representing different but complementary aspects of brain activity (fMRI and PET).
II. Secondly, to delve deeper into the investigation of coupling between brain function and metabolism using a multivariate analysis method capable of detecting similarities and differences in each brain region contribution to the common covariation pattern between functional and metabolic data.
III. Lastly, to utilize the insights gained from control subjects (specifically, saliences) to project glioma patient's data onto the latent space derived from healthy controls. This enables the investigation of how gliomas affect the coupling between function and metabolism, both locally and within brain networks.

Both control subjects and patients underwent ROI-level measurements of metabolism and function, estimating Sokoloff model parameters (K_1, k_3, and K_i) from dynamic PET data, *SUVR* from static PET data, and deriving functional connectivity strength from fMRI data. Functional connectivity matrices in F_1 (0.008-0.11 Hz) and F_2 (0.008-0.21 Hz) bands and metabolic connectivity matrices were then derived for network-level analysis. From the PLSC analysis conducted on control subject data, pairs between local metabolic parameters (K_1, k_3, K_i and *SUVR*) and the corresponding node-wise strength of functional connectivity (FC_{STR}) were evaluated for each subject. Meanwhile, for FC and MC matrices, upper triangular edgewise features were selected to assess the whole-network functional-metabolic coupling.

The results demonstrate the PLSC's capability to capture covariation patterns between brain function and metabolism using both local and network-level approaches, with analysis revealing differences in results based on the frequency band in which the BOLD signal was filtered to obtain FC. Despite utilizing a full version of PLS, which is prone to overfitting, especially with a small sample size like in this study, the method proved robust and consistent in identifying both similarities and intrinsic differences between multimodal fMRI and PET data, which strongly influence their whole-brain relationship.

The first finding is the lack of a generalized coupling between FC strength and kinetic parameters k_3, and K_i. Differences in these parameters, reflecting rapid biochemical processes, and FC measures, assessing neural activity correlations over longer periods, may lead to limited coupling between them. Moreover, they operate at different biological levels and may lack direct causal relationships, given the complexity of brain dynamics.

Overall, the results corroborate existing literature, showing limited spatial correspondence between functional and metabolic brain data at the local level. This discrepancy is particularly notable for the *SUVR-*FC_{STR} pair, which exhibited poor capacity to describe the intricate relationships between brain function and metabolism. This discrepancy primarily arises from the nonlinear nature of the relationship between glucose uptake and consumption with fMRI data, especially when described by metrics derived from static functional connectivity like the strength used in this study.

In the F_2 band, the coupling between K_1 and FC_{STR} was notably higher, likely due to both data modalities encapsulating hemodynamic components. This reveals a direct correlation between regional glucose influx rate and the strength of functional interactions, delineating two distinct groups. The first group exhibits high-order networks with lower FC strength but higher K_1 values, indicative of heightened metabolic activity, possibly signifying a more integrative neural role. Conversely, the second group displays stronger FC but lower K_1 values, suggesting a more specialized function. This variability emphasizes the necessity of accounting for individual metabolic and functional connectivity differences to comprehend brain function and dysfunction at a personalized

level. Thus, considering the patient-level analysis, this pair highlights how lower K_1 values associated with nearly "normal" FC strength in peri-tumoral areas could be potential biomarkers for frontal lobe tumor presence.

Even more significant results were obtained from the network-level analysis between FC and MC matrices, which demonstrated consistent and robust behaviour in both frequency bands in which FC was obtained. This supports the notion that the link between brain function and metabolism operates at various temporal scales, capturing the contribution of the hemodynamic component. This analysis highlighted how, regardless of subject differences, the covariance pattern between FC and MC remains consistent, with more segregated FC in unimodal areas corresponding to globally more integrated MC, suggesting that stable FC consumes more energy. Moreover, the study identified important differences in functional-metabolic coupling also between homologous areas of different hemispheres. Higher concordance in saliences was observed in the left frontal and right occipital lobes, indicative of their involvement in fundamental cognitive and sensory functions requiring consistent neural activity and substantial metabolic energy. Conversely, greater discordance in saliences was found in posterior and subcortical regions, such as the left cerebellum and deep insular regions on the right, possibly due to their specialized functions and the need for frequent metabolic adjustments to support diverse connectivity patterns.

From the patient-level analysis, it was interesting to note a modest but significant reversal of the positive linear trend observed in HCs, indicating that the presence of a glioma, particularly in the frontal lobe, leads to a decrease in FC values compared to the average values of HCs, which is associated with an increase in MC values. This suggests that the brain struggles more metabolically, increasing metabolic connectivity to support the much-reduced functional connectivity between these areas and vice versa. Lastly, it was intriguing to observe how the decoupling between FC and MC was even more precise in localizing a tumor in the frontal lobe compared to the K_1-FC_{STR} pair, further supporting the hypothesis that the strongest relationship between functional connectivity and metabolism, in terms of positive concordance, occurs in the frontal regions of the brain.

Despite the innovative findings presented in this study, it is crucial to acknowledge certain limitations.

1) While acquisitions for healthy subjects weren't simultaneous, they were for patients, facilitated by a hybrid PET/MRI system capturing concurrent metabolic and functional changes efficiently. This is crucial for accurately evaluating their interwoven relationship, eliminating interference from intra-subject variations [201].
2) Despite K-fold cross-validation used for assessing PLS model generalizability, small sample size risks overfitting, addressable by more sophisticated regularized extensions of PLS, like sparse variants [175].
3) Analysing only saliences lacks insight into which variables contribute most to the PLS-derived latent variables; incorporating loadings would provide a clearer picture of each variable contribution to patient's deviation [123].
4) Age range disparity in healthy datasets might limit finding's generalizability due to age-related alterations in brain parameters, like regional cerebral blood flow (rCBF), glucose consumption, and structural covariance [186].
5) The study didn't differentiate between low- and high-grade glioma functional and metabolic features despite known grade impacts on brain network integrity [80], [82], [159]. Also, most patients had high-grade tumours, resulting in a dataset skewed towards HGG. Thus, larger, diverse patient samples could reveal distinct alterations based on tumour grade.
6) [^{18}F]FDG-PET imaging limitations in detecting non-oxidative metabolic pathways hinder a comprehensive understanding of physiological processes governing brain glucose consumption kinetics, crucial in gliomas [223].
7) Greater inter-subject variability in glucose consumption during resting-state acquisitions compared to task-based ones is influenced by various neural intrinsic processes, complicating interpretation [198].

The nonlinear relationship between *SUVR* and FC strength suggests high-metabolism regions possess properties not well-captured by rs-fMRI, complicating functional predictor's interpretation. Direct assessment of CBF and $CMRO_2$ using PET imaging could offer a more comprehensive understanding of functional-metabolic relationships [200], [202].

In conclusion, although this thesis has delved deeply into the investigation of the coupling between brain function and metabolism, the inherent complexity of these mechanisms requires further analysis. Regional metabolic variability is only partially elucidated by resting-state brain activity as described by rs-fMRI, indicating the need for further exploration of the remaining spatial and inter-individual variability in brain glucose consumption. Building on these findings, future efforts will focus on evaluating resting-state networks using multitracer approaches targeting different neurotransmitter systems. Critical questions include determining whether the strongest negative relationship between brain function and metabolism occurs proximal to the tumour or within relevant cognitive networks. Furthermore, exploring the potential to predict patient's clinical and cognitive trajectories based on these deviations may provide insights into how neuron-glioma interactions influence clinical outcomes and prognosis. Ultimately, such insights may help clinicians manage expectations and identify patients who may benefit from clinical interventions.

References

[1] E. R. Kandel, J. H. Schwartz, T. M. Jessell, S. Siegelbaum, A. J. Hudspeth, and S. Mack, *Principles of neural science*, vol. 4. McGraw-hill New York, 2000.

[2] G. Bonvento and J. P. Bolaños, 'Astrocyte-neuron metabolic cooperation shapes brain activity', *Cell Metab.*, vol. 33, no. 8, pp. 1546–1564, Aug. 2021, doi: 10.1016/j.cmet.2021.07.006.

[3] P. E. Ludwig, V. Reddy, and M. Varacallo, 'Neuroanatomy, neurons', 2017.

[4] 'Brain Basics: Know Your Brain | National Institute of Neurological Disorders and Stroke'. Accessed: Apr. 06, 2024. [Online]. Available: https://www.ninds.nih.gov/health-information/public-education/brainbasics/brain-basics-know-your-brain.

[5] P. J. Magistretti, 'Neuron-glia metabolic coupling and plasticity: Neuron-glia metabolic coupling and plasticity', *Exp. Physiol.*, vol. 96, no. 4, pp. 407–410, Apr. 2011, doi: 10.1113/expphysiol.2010.053157.

[6] C. R. Figley and P. W. Stroman, 'The role(s) of astrocytes and astrocyte activity in neurometabolism, neurovascular coupling, and the production of functional neuroimaging signals: Astrocyte control of fMRI and PET signals', *Eur. J. Neurosci.*, vol. 33, no. 4, pp. 577–588, Feb. 2011, doi: 10.1111/j.1460-9568.2010.07584.x.

[7] P. Mulica, A. Grünewald, and S. L. Pereira, 'Astrocyte-Neuron Metabolic Crosstalk in Neurodegeneration: A Mitochondrial Perspective', *Front. Endocrinol.*, vol. 12, p. 668517, May 2021, doi: 10.3389/fendo.2021.668517.

[8] A. Almeida, D. Jimenez-Blasco, and J. P. Bolaños, 'Cross-talk between energy and redox metabolism in astrocyte-neuron functional cooperation', *Essays Biochem.*, vol. 67, no. 1, pp. 17–26, Mar. 2023, doi: 10.1042/EBC20220075.

[9] M. V. Sofroniew and H. V. Vinters, 'Astrocytes: biology and pathology', *Acta Neuropathol. (Berl.)*, vol. 119, pp. 7–35, 2010.

[10] B. He and Z. Liu, 'Multimodal functional neuroimaging: integrating functional MRI and EEG/MEG', *IEEE Rev. Biomed. Eng.*, vol. 1, pp. 23–40, 2008.

[11] A. Hahn *et al.*, 'High-temporal resolution functional PET/MRI reveals coupling between human metabolic and hemodynamic brain response', *Eur. J. Nucl. Med. Mol. Imaging*, pp. 1–13, 2023.

[12] Alessandra Bertoldo, 'Lectures of Imaging for Neuroscience course', University of Padua, 2012.

[13] R. B. Buxton, 'Dynamic models of BOLD contrast', *Neuroimage*, vol. 62, no. 2, pp. 953–961, 2012.

[14] S. Ogawa, T.-M. Lee, A. S. Nayak, and P. Glynn, 'Oxygenation-sensitive contrast in magnetic resonance image of rodent brain at high magnetic fields', *Magn. Reson. Med.*, vol. 14, no. 1, pp. 68–78, 1990.

[15] T. L. Atenas, E. C. Díaz, J. C. Quiroga, S. U. Arancibia, and C. C. Rodríguez, 'Functional magnetic resonance imaging: basic principles and application in the neurosciences', *Radiol. Engl. Ed.*, vol. 60, no. 5, pp. 368–377, 2018.

[16] A. M. Howseman and R. W. Bowtel, 'Functional magnetic resonance imaging: imaging techniques and contrast mechanisms', *Philos. Trans. R. Soc. Lond. B. Biol. Sci.*, vol. 354, no. 1387, pp. 1179–1194, 1999.

[17] K. Uludağ, 'Physiological Modeling of the BOLD signal and Implications for Effective Connectivity: a primer', *Neuroimage*, vol. 277, p. 120249, 2023.

[18] S. A. Huettel, A. W. Song, and G. McCarthy, 'Functional magnetic resonance imaging', *No Title*, 2004.

[19] K. J. Friston, 'Statistical parametric mapping', *Neurosci. Databases Pract. Guide*, pp. 237–250, 2003.

[20] M. E. Raichle and M. A. Mintun, 'Brain work and brain imaging', *Annu Rev Neurosci*, vol. 29, pp. 449–476, 2006.

[21] M. D. Fox and M. E. Raichle, 'Spontaneous fluctuations in brain activity observed with functional magnetic resonance imaging', *Nat. Rev. Neurosci.*, vol. 8, no. 9, pp. 700–711, 2007.

[22] B. Biswal, F. Zerrin Yetkin, V. M. Haughton, and J. S. Hyde, 'Functional connectivity in the motor cortex of resting human brain using echo-planar MRI', *Magn. Reson. Med.*, vol. 34, no. 4, pp. 537–541, 1995.

[23] B. Biswal, A. G. Hudetz, F. Z. Yetkin, V. M. Haughton, and J. S. Hyde, 'Hypercapnia reversibly suppresses low-frequency fluctuations in the human motor cortex during rest using echo–planar MRI', *J. Cereb. Blood Flow Metab.*, vol. 17, no. 3, pp. 301–308, 1997.

[24] M. D. Fox, A. Z. Snyder, J. L. Vincent, M. Corbetta, D. C. Van Essen, and M. E. Raichle, 'The human brain is intrinsically organized into dynamic, anticorrelated functional networks', *Proc. Natl. Acad. Sci.*, vol. 102, no. 27, pp. 9673–9678, 2005.

[25] R. L. Buckner, J. R. Andrews-Hanna, and D. L. Schacter, 'The brain's default network: anatomy, function, and relevance to disease', *Ann. N. Y. Acad. Sci.*, vol. 1124, no. 1, pp. 1–38, 2008.

[26] R. L. Buckner and J. L. Vincent, 'Unrest at rest: default activity and spontaneous network correlations', *Neuroimage*, vol. 37, no. 4, pp. 1091–1096, 2007.

[27] M. D. Greicius, K. Supekar, V. Menon, and R. F. Dougherty, 'Resting-state functional connectivity reflects structural connectivity in the default mode network', *Cereb. Cortex*, vol. 19, no. 1, pp. 72–78, 2009.

[28] B. B. Biswal, ‘Resting state fMRI: a personal history’, *Neuroimage*, vol. 62, no. 2, pp. 938–944, 2012.

[29] J. S. Damoiseaux *et al.*, ‘Consistent resting-state networks across healthy subjects’, *Proc. Natl. Acad. Sci.*, vol. 103, no. 37, pp. 13848–13853, 2006.

[30] M. De Luca, S. Smith, N. De Stefano, A. Federico, and P. M. Matthews, ‘Blood oxygenation level dependent contrast resting state networks are relevant to functional activity in the neocortical sensorimotor system’, *Exp. Brain Res.*, vol. 167, pp. 587–594, 2005.

[31] M. J. Lowe, M. Dzemidzic, J. T. Lurito, V. P. Mathews, and M. D. Phillips, ‘Correlations in low-frequency BOLD fluctuations reflect cortico-cortical connections’, *Neuroimage*, vol. 12, no. 5, pp. 582–587, 2000.

[32] R. Salvador, J. Suckling, M. R. Coleman, J. D. Pickard, D. Menon, and E. D. Bullmore, ‘Neurophysiological architecture of functional magnetic resonance images of human brain’, *Cereb. Cortex*, vol. 15, no. 9, pp. 1332–1342, 2005.

[33] M. Van Den Heuvel, R. Mandl, and H. Hulshoff Pol, ‘Normalized cut group clustering of resting-state FMRI data’, *PloS One*, vol. 3, no. 4, p. e2001, 2008.

[34] D. Cordes *et al.*, ‘Mapping functionally related regions of brain with functional connectivity MR imaging’, *Am. J. Neuroradiol.*, vol. 21, no. 9, pp. 1636–1644, 2000.

[35] D. Cordes *et al.*, ‘Frequencies contributing to functional connectivity in the cerebral cortex in “resting-state” data’, *Am. J. Neuroradiol.*, vol. 22, no. 7, pp. 1326–1333, 2001.

[36] Y. Nir *et al.*, ‘Interhemispheric correlations of slow spontaneous neuronal fluctuations revealed in human sensory cortex’, *Nat. Neurosci.*, vol. 11, no. 9, pp. 1100–1108, 2008.

[37] A. Shmuel *et al.*, ‘Sustained negative BOLD, blood flow and oxygen consumption response and its coupling to the positive response in the human brain’, *Neuron*, vol. 36, no. 6, pp. 1195–1210, 2002.

[38] A. Shmuel and D. A. Leopold, ‘Neuronal correlates of spontaneous fluctuations in fMRI signals in monkey visual cortex: Implications for functional connectivity at rest’, *Hum. Brain Mapp.*, vol. 29, no. 7, pp. 751–761, 2008.

[39] R. M. Birn, M. A. Smith, T. B. Jones, and P. A. Bandettini, ‘The respiration response function: The temporal dynamics of fMRI signal fluctuations related to changes in respiration’, *NeuroImage*, vol. 40, no. 2, pp. 644–654, Apr. 2008, doi: 10.1016/j.neuroimage.2007.11.059.

[40] M.-C. Chiang *et al.*, ‘Genetics of Brain Fiber Architecture and Intellectual Performance’, *The Journal of Neuroscience*, vol. 29, no. 7. pp. 2212–2224, 2009.

[41] M. Van Buuren *et al.*, ‘Cardiorespiratory effects on default-mode network activity as measured with fMRI’, *Hum. Brain Mapp.*, vol. 30, no. 9, pp. 3031–3042, 2009.

[42] A. Weissenbacher, C. Kasess, F. Gerstl, R. Lanzenberger, E. Moser, and C. Windischberger, 'Correlations and anticorrelations in resting-state functional connectivity MRI: a quantitative comparison of preprocessing strategies', *Neuroimage*, vol. 47, no. 4, pp. 1408–1416, 2009.

[43] T. Jiang, Y. He, Y. Zang, and X. Weng, 'Modulation of functional connectivity during the resting state and the motor task', *Hum. Brain Mapp.*, vol. 22, no. 1, pp. 63–71, 2004.

[44] M. P. Young, K. Friston, J. Phillips, D. Chawla, and C. Buchel, 'Nonlinear PCA: characterizing interactions between modes of brain activity', *Philos. Trans. R. Soc. Lond. B. Biol. Sci.*, vol. 355, no. 1393, pp. 135–146, Jan. 2000, doi: 10.1098/rstb.2000.0554.

[45] C. F. Beckmann, M. DeLuca, J. T. Devlin, and S. M. Smith, 'Investigations into resting-state connectivity using independent component analysis', *Philos. Trans. R. Soc. B Biol. Sci.*, vol. 360, no. 1457, pp. 1001–1013, 2005.

[46] V. D. Calhoun, T. Adali, G. D. Pearlson, and J. J. Pekar, 'A method for making group inferences from functional MRI data using independent component analysis.', *Hum. Brain Mapp.*, vol. 14, no. 3, pp. 140–151, Nov. 2001, doi: 10.1002/hbm.1048.

[47] V. G. van de Ven, E. Formisano, D. Prvulovic, C. H. Roeder, and D. E. Linden, 'Functional connectivity as revealed by spatial independent component analysis of fMRI measurements during rest', *Hum. Brain Mapp.*, vol. 22, no. 3, pp. 165–178, 2004.

[48] D. Cordes, V. Haughton, J. D. Carew, K. Arfanakis, and K. Maravilla, 'Hierarchical clustering to measure connectivity in fMRI resting-state data', *Magn. Reson. Imaging*, vol. 20, no. 4, pp. 305–317, 2002.

[49] B. Thirion, S. Dodel, and J.-B. Poline, 'Detection of signal synchronizations in resting-state fMRI datasets', *Neuroimage*, vol. 29, no. 1, pp. 321–327, 2006.

[50] M. Van Den Heuvel, R. Mandl, J. Luigjes, and H. H. Pol, 'Microstructural organization of the cingulum tract and the level of default mode functional connectivity', *J. Neurosci.*, vol. 28, no. 43, pp. 10844–10851, 2008.

[51] M. P. Van Den Heuvel and H. E. H. Pol, 'Exploring the brain network: a review on resting-state fMRI functional connectivity', *Eur. Neuropsychopharmacol.*, vol. 20, no. 8, pp. 519–534, 2010.

[52] L. Q. Uddin, B. T. T. Yeo, and R. N. Spreng, 'Towards a Universal Taxonomy of Macro-scale Functional Human Brain Networks', *Brain Topogr.*, vol. 32, no. 6, pp. 926–942, Nov. 2019, doi: 10.1007/s10548-019-00744-6.

[53] K. Smitha *et al.*, 'Resting state fMRI: A review on methods in resting state connectivity analysis and resting state networks', *Neuroradiol. J.*, vol. 30, no. 4, pp. 305–317, Aug. 2017, doi: 10.1177/1971400917697342.

[54] K. Wang *et al.*, ‘Spontaneous activity associated with primary visual cortex: a resting-state FMRI study’, *Cereb. Cortex*, vol. 18, no. 3, pp. 697–704, 2008.

[55] M. D. Fox, M. Corbetta, A. Z. Snyder, J. L. Vincent, and M. E. Raichle, ‘Spontaneous neuronal activity distinguishes human dorsal and ventral attention systems’, *Proc. Natl. Acad. Sci.*, vol. 103, no. 26, pp. 10046–10051, Jun. 2006, doi: 10.1073/pnas.0604187103.

[56] K. Farrant and L. Q. Uddin, ‘Asymmetric development of dorsal and ventral attention networks in the human brain’, *Dev. Cogn. Neurosci.*, vol. 12, pp. 165–174, Apr. 2015, doi: 10.1016/j.dcn.2015.02.001.

[57] B. J. Tamber-Rosenau, C. L. Asplund, and R. Marois, ‘Functional dissociation of the inferior frontal junction from the dorsal attention network in top-down attentional control’, *J. Neurophysiol.*, vol. 120, no. 5, pp. 2498–2512, Nov. 2018, doi: 10.1152/jn.00506.2018.

[58] C. Gratton, H. Sun, and S. E. Petersen, ‘Control networks and hubs’, *Psychophysiology*, vol. 55, no. 3, p. e13032, Mar. 2018, doi: 10.1111/psyp.13032.

[59] M. L. Dixon *et al.*, ‘Heterogeneity within the frontoparietal control network and its relationship to the default and dorsal attention networks’, *Proc. Natl. Acad. Sci.*, vol. 115, no. 7, pp. E1598–E1607, 2018.

[60] S. Achard and E. Bullmore, ‘Efficiency and Cost of Economical Brain Functional Networks’, *PLOS Comput. Biol.*, vol. 3, no. 2, p. e17, Feb. 2007, doi: 10.1371/journal.pcbi.0030017.

[61] S. Achard, R. Salvador, B. Whitcher, J. Suckling, and E. D. Bullmore, ‘A resilient, low-frequency, small-world human brain functional network with highly connected association cortical hubs’, *J. Neurosci.*, vol. 26, no. 1, pp. 63–72, 2006.

[62] M. P. van den Heuvel, C. J. Stam, M. Boersma, and H. H. Pol, ‘Small-world and scale-free organization of voxel-based resting-state functional connectivity in the human brain’, *Neuroimage*, vol. 43, no. 3, pp. 528–539, 2008.

[63] M. P. Van Den Heuvel, R. C. W. Mandl, R. S. Kahn, and H. E. Hulshoff Pol, ‘Functionally linked resting-state networks reflect the underlying structural connectivity architecture of the human brain’, *Hum. Brain Mapp.*, vol. 30, no. 10, pp. 3127–3141, Oct. 2009, doi: 10.1002/hbm.20737.

[64] M. Rubinov and O. Sporns, ‘Complex network measures of brain connectivity: uses and interpretations’, *Neuroimage*, vol. 52, no. 3, pp. 1059–1069, 2010.

[65] K. J. Friston, P. Jezzard, and R. Turner, ‘Analysis of functional MRI time-series’, *Hum. Brain Mapp.*, vol. 1, no. 2, pp. 153–171, 1994.

[66] F. V. Farahani, W. Karwowski, and N. R. Lighthall, ‘Application of Graph Theory for Identifying Connectivity Patterns in Human Brain Networks: A Systematic Review’, *Front. Neurosci.*, vol. 13, p. 585, Jun. 2019, doi: 10.3389/fnins.2019.00585.

[67] M. Rubinov and O. Sporns, ‘Weight-conserving characterization of complex functional brain networks’, *Neuroimage*, vol. 56, no. 4, pp. 2068–2079, 2011.

[68] S. L. Simpson, F. D. Bowman, and P. J. Laurienti, ‘Analyzing complex functional brain networks: fusing statistics and network science to understand the brain’, *Stat. Surv.*, vol. 7, p. 1, 2013.

[69] J. Wang *et al.*, ‘Parcellation-dependent small-world brain functional networks: A resting-state fMRI study’, *Hum. Brain Mapp.*, vol. 30, no. 5, pp. 1511–1523, 2009.

[70] A. Barrat, M. Barthelemy, R. Pastor-Satorras, and A. Vespignani, ‘The architecture of complex weighted networks’, *Proc. Natl. Acad. Sci.*, vol. 101, no. 11, pp. 3747–3752, 2004.

[71] C. E. Ginestet, T. E. Nichols, E. T. Bullmore, and A. Simmons, ‘Brain network analysis: separating cost from topology using cost-integration’, *PloS One*, vol. 6, no. 7, p. e21570, 2011.

[72] C. J. Stam *et al.*, ‘Graph theoretical analysis of magnetoencephalographic functional connectivity in Alzheimer’s disease’, *Brain*, vol. 132, no. 1, pp. 213–224, 2009.

[73] M. Ercsey-Ravasz *et al.*, ‘A predictive network model of cerebral cortical connectivity based on a distance rule’, *Neuron*, vol. 80, no. 1, pp. 184–197, 2013.

[74] E. Gonzalez-Mulé, M. K. Mount, and I.-S. Oh, ‘A meta-analysis of the relationship between general mental ability and nontask performance.’, *J. Appl. Psychol.*, vol. 99, no. 6, p. 1222, 2014.

[75] B. J. He, A. Z. Snyder, J. L. Vincent, A. Epstein, G. L. Shulman, and M. Corbetta, ‘Breakdown of functional connectivity in frontoparietal networks underlies behavioral deficits in spatial neglect’, *Neuron*, vol. 53, no. 6, pp. 905–918, 2007.

[76] D. P. Auer, ‘Spontaneous low-frequency blood oxygenation level-dependent fluctuations and functional connectivity analysis of the ‘resting’brain’, *Magn. Reson. Imaging*, vol. 26, no. 7, pp. 1055–1064, 2008.

[77] S. O’Connor and M. Agius, ‘A systematic review of structural and functional MRI differences between psychotic and nonpsychotic depression’, *Psychiatr. Danub.*, vol. 27, no. suppl 1, pp. 235–239, 2015.

[78] A. Gallo *et al.*, ‘Visual resting-state network in relapsing-remitting MS with and without previous optic neuritis’, *Neurology*, vol. 79, no. 14, pp. 1458–1465, 2012.

[79] S. Ghumman, D. Fortin, M. Noel-Lamy, S. C. Cunnane, and K. Whittingstall, ‘Exploratory study of the effect of brain tumors on the default mode network’, *J. Neurooncol.*, vol. 128, pp. 437–444, 2016.

[80] R. J. Harris *et al.*, ‘Altered functional connectivity of the default mode network in diffuse gliomas measured with pseudo-resting state fMRI’, *J. Neurooncol.*, vol. 116, pp. 373–379, 2014.

[81] H. Duffau, ‘Letter to the Editor: Cognitive assessment in glioma patients’, *J. Neurosurg.*, vol. 119, no. 5, pp. 1348–1349, Nov. 2013, doi: 10.3171/2012.2.JNS112372.

[82] S. Maesawa *et al.*, ‘Evaluation of resting state networks in patients with gliomas: connectivity changes in the unaffected side and its relation to cognitive function’, *PloS One*, vol. 10, no. 2, p. e0118072, 2015.

[83] S. Agarwal, H. I. Sair, S. Gujar, J. Hua, H. Lu, and J. J. Pillai, ‘Functional magnetic resonance imaging activation optimization in the setting of brain tumor-induced neurovascular uncoupling using resting-state blood oxygen level-dependent amplitude of low frequency fluctuations’, *Brain Connect.*, vol. 9, no. 3, pp. 241–250, 2019.

[84] Q. T. Ostrom *et al.*, ‘The epidemiology of glioma in adults: a “state of the science” review’, *Neuro-Oncol.*, vol. 16, no. 7, pp. 896–913, Jul. 2014, doi: 10.1093/neuonc/nou087.

[85] A. N. Mallela, K. K. Peck, N. M. Petrovich-Brennan, Z. Zhang, W. Lou, and A. I. Holodny, ‘Altered resting-state functional connectivity in the hand motor network in glioma patients’, *Brain Connect.*, vol. 6, no. 8, pp. 587–595, 2016.

[86] Q. Wang *et al.*, ‘The diagnostic performance of magnetic resonance spectroscopy in differentiating high-from low-grade gliomas: A systematic review and meta-analysis’, *Eur. Radiol.*, vol. 26, no. 8, pp. 2670–2684, Aug. 2016, doi: 10.1007/s00330-015-4046-z.

[87] D. S. Chow *et al.*, ‘Glioblastoma Induces Vascular Dysregulation in Nonenhancing Peritumoral Regions in Humans’, *Am. J. Roentgenol.*, vol. 206, no. 5, pp. 1073–1081, May 2016, doi: 10.2214/AJR.15.14529.

[88] N. Tuovinen *et al.*, ‘Transient effects of tumor location on the functional architecture at rest in glioblastoma patients: three longitudinal case studies’, *Radiat. Oncol.*, vol. 11, no. 1, p. 107, Dec. 2016, doi: 10.1186/s13014-016-0683-x.

[89] J. E. Park, H. S. Kim, K. J. Park, S. J. Kim, J. H. Kim, and S. A. Smith, ‘Pre-and posttreatment glioma: comparison of amide proton transfer imaging with MR spectroscopy for biomarkers of tumor proliferation’, *Radiology*, vol. 278, no. 2, pp. 514–523, 2016.

[90] M. G. Hart, S. J. Price, and J. Suckling, ‘Connectome analysis for pre-operative brain mapping in neurosurgery’, *Br. J. Neurosurg.*, vol. 30, no. 5, pp. 506–517, Sep. 2016, doi: 10.1080/02688697.2016.1208809.

[91] C. Niu *et al.*, ‘Motor network plasticity and low-frequency oscillations abnormalities in patients with brain gliomas: a functional MRI study’, *PLoS One*, vol. 9, no. 5, p. e96850, 2014.

[92] E. Mittra and A. Quon, ‘Positron Emission Tomography/Computed Tomography: The Current Technology and Applications’, *Radiol. Clin. North Am.*, vol. 47, no. 1, pp. 147–160, Jan. 2009, doi: 10.1016/j.rcl.2008.10.005.

[93] S. R. Cherry and M. Dahlbom, ‘PET: Physics, Instrumentation, and Scanners’, in *PET*, M. E. Phelps, Ed., New York, NY: Springer New York, 2006, pp. 1–117. doi: 10.1007/0-387-34946-4_1.

[94] M. Quigg and B. Kundu, ‘Dynamic FDG-PET demonstration of functional brain abnormalities’, *Ann. Clin. Transl. Neurol.*, vol. 9, no. 9, pp. 1487–1497, Sep. 2022, doi: 10.1002/acn3.51546.

[95] E. Carson and C. Cobelli, *Modelling methodology for physiology and medicine*. Newnes, 2013.

[96] W. Wang *et al.*, ‘Association of longitudinal cognitive decline with diffusion MRI in Gray Matter, Amyloid, and Tau deposition’, *Neurobiol. Aging*, vol. 121, pp. 166–178, Jan. 2023, doi: 10.1016/j.neurobiolaging.2022.10.013.

[97] A. P. Seiffert *et al.*, ‘Differences in Striatal Metabolism in [^{18}F]FDG PET in Parkinson’s Disease and Atypical Parkinsonism’, *Diagnostics*, vol. 13, no. 1, p. 6, Dec. 2022, doi: 10.3390/diagnostics13010006.

[98] P. Vemuri *et al.*, ‘Tau-PET uptake: Regional variation in average SUVR and impact of amyloid deposition’, *Alzheimers Dement. Diagn. Assess. Dis. Monit.*, vol. 6, no. 1, pp. 21–30, Jan. 2017, doi: 10.1016/j.dadm.2016.12.010.

[99] L. Sokoloff *et al.*, ‘The [14C] deoxyglucose method for the measurement of local cerebral glucose utilization: theory, procedure, and normal values in the conscious and anesthetized albino rat 1’, *J. Neurochem.*, vol. 28, no. 5, pp. 897–916, 1977.

[100] A. Bertoldo, G. Rizzo, and M. Veronese, ‘Deriving physiological information from PET images: from SUV to compartmental modelling’, *Clin. Transl. Imaging*, vol. 2, no. 3, pp. 239–251, Jun. 2014, doi: 10.1007/s40336-014-0067-x.

[101] W.-D. Heiss, G. Pawlik, K. Herholz, R. Wagner, H. Göldner, and K. Wienhard, ‘Regional kinetic constants and cerebral metabolic rate for glucose in normal human volunteers determined by dynamic positron emission tomography of [18F]-2-fluoro-2-deoxy-D-glucose’, *J. Cereb. Blood Flow Metab.*, vol. 4, no. 2, pp. 212–223, 1984.

[102] E. Rapisarda, L. Presotto, E. De Bernardi, M. C. Gilardi, and V. Bettinardi, ‘Optimized Bayes variational regularization prior for 3D PET images’, *Comput. Med. Imaging Graph.*, vol. 38, no. 6, pp. 445–457, 2014.

[103] Y. Xia, J. Wang, S. Eberl, M. Fulham, and D. D. Feng, ‘Brain tissue segmentation in PET-CT images using probabilistic atlas and variational Bayes inference’, in *2011 Annual International Conference of the IEEE Engineering in Medicine and Biology Society*, IEEE, 2011, pp. 7969–7972.

[104] M. Castellaro *et al.*, ‘A Variational Bayesian inference method for parametric imaging of PET data’, *Neuroimage*, vol. 150, pp. 136–149, 2017.

[105] H. Attias, ‘A variational baysian framework for graphical models’, *Adv. Neural Inf. Process. Syst.*, vol. 12, 1999.

[106] M. J. Beal, *Variational algorithms for approximate Bayesian inference*. University of London, University College London (United Kingdom), 2003.

[107] B. Horwitz, R. Duara, and S. I. Rapoport, ‘Intercorrelations of glucose metabolic rates between brain regions: application to healthy males in a state of reduced sensory input’, *J. Cereb. Blood Flow Metab.*, vol. 4, no. 4, pp. 484–499, 1984.

[108] T. Volpi *et al.*, ‘A new framework for metabolic connectivity mapping using bolus [^{18}F]FDG PET and kinetic modelling’. Dec. 30, 2022. doi: 10.1101/2022.12.27.522050.

[109] I. Yakushev, A. Drzezga, and C. Habeck, ‘Metabolic connectivity: methods and applications’, *Curr. Opin. Neurol.*, vol. 30, no. 6, pp. 677–685, Dec. 2017, doi: 10.1097/WCO.0000000000000494.

[110] H. F. Wehrl *et al.*, ‘Simultaneous PET-MRI reveals brain function in activated and resting state on metabolic, hemodynamic and multiple temporal scales’, *Nat. Med.*, vol. 19, no. 9, pp. 1184–1189, 2013.

[111] K. Das, B. Mittal, R. Vasistha, P. Singh, and S. Mathuriya, ‘Role of ^{18} F-fluorodeoxyglucose Positron Emission Tomography scan in differentiating enhancing brain tumors’, *Indian J. Nucl. Med.*, vol. 26, no. 4, p. 171, 2011, doi: 10.4103/0972-3919.106698.

[112] G. Di Chiro *et al.*, ‘Glucose utilization of cerebral gliomas measured by [18F] fluorodeoxyglucose and positron emission tomography’, *Neurology*, vol. 32, no. 12, pp. 1323–1323, 1982.

[113] J. L. Tyler *et al.*, ‘Metabolic and hemodynamic evaluation of gliomas using positron emission tomography’, *J. Nucl. Med.*, vol. 28, no. 7, pp. 1123–1133, 1987.

[114] N. Kimura, Y. Yamamoto, R. Kameyama, T. Hatakeyama, N. Kawai, and Y. Nishiyama, ‘Diagnostic value of kinetic analysis using dynamic 18F-FDG-PET in patients with malignant primary brain tumor’, *Nucl. Med. Commun.*, vol. 30, no. 8, pp. 602–609, Aug. 2009, doi: 10.1097/MNM.0b013e32832e1c7d.

[115] M. Pourdehnad *et al.*, ‘Reduced grey matter metabolism due to white matter edema allows optimal assessment of brain tumors on 18F-FDG-PET.’, *Hell. J. Nucl. Med.*, vol. 14, no. 3, pp. 219–223, 2011.

[116] L. Li *et al.*, ‘A Non-invasive Radiomic Method Using 18F-FDG PET Predicts Isocitrate Dehydrogenase Genotype and Prognosis in Patients With Glioma’, *Front. Oncol.*, vol. 9, p. 1183, Nov. 2019, doi: 10.3389/fonc.2019.01183.

[117] I. N. Pronin *et al.*, ‘Phosphorus MR spectroscopy and 18F-FDG PET/CT in the study of energy metabolism of glial tumors’, *Vopr. Neirokhirurgii Im. NN Burdenko*, vol. 85, no. 2, p. 26, 2021, doi: 10.17116/neiro20218502126.

[118] D. Tomasi, G.-J. Wang, and N. D. Volkow, ‘Energetic cost of brain functional connectivity’, *Proc. Natl. Acad. Sci.*, vol. 110, no. 33, pp. 13642–13647, 2013.

[119] M. Aiello *et al.*, ‘Relationship between simultaneously acquired resting-state regional cerebral glucose metabolism and functional MRI: A PET/MR hybrid scanner study’, *NeuroImage*, vol. 113, pp. 111–121, Jun. 2015, doi: 10.1016/j.neuroimage.2015.03.017.

[120] D. G. Tomasi *et al.*, ‘Dynamic brain glucose metabolism identifies anti-correlated cortical-cerebellar networks at rest’, *J. Cereb. Blood Flow Metab.*, vol. 37, no. 12, pp. 3659–3670, Dec. 2017, doi: 10.1177/0271678X17708692.

[121] S. D. Jamadar, P. G. D. Ward, E. X. Liang, E. R. Orchard, Z. Chen, and G. F. Egan, ‘Metabolic and Hemodynamic Resting-State Connectivity of the Human Brain: A High-Temporal Resolution Simultaneous BOLD-fMRI and FDG-fPET Multimodality Study’, *Cereb. Cortex*, vol. 31, no. 6, pp. 2855–2867, May 2021, doi: 10.1093/cercor/bhaa393.

[122] A. Palombit *et al.*, ‘Variability of regional glucose metabolism and the topology of functional networks in the human brain’, *NeuroImage*, vol. 257, p. 119280, Aug. 2022, doi: 10.1016/j.neuroimage.2022.119280.

[123] K. Voigt, E. X. Liang, B. Misic, P. G. D. Ward, G. F. Egan, and S. D. Jamadar, ‘Metabolic and functional connectivity provide unique and complementary insights into cognition-connectome relationships’, *Cereb. Cortex*, vol. 33, no. 4, pp. 1476–1488, Feb. 2023, doi: 10.1093/cercor/bhac150.

[124] J. Y. Hansen *et al.*, ‘Multimodal, multiscale connectivity blueprints of the cerebral cortex’. Dec. 02, 2022. doi: 10.1101/2022.12.02.518906.

[125] J. Sui, T. Adali, Q. Yu, J. Chen, and V. D. Calhoun, ‘A review of multivariate methods for multimodal fusion of brain imaging data’, *J. Neurosci. Methods*, vol. 204, no. 1, pp. 68–81, 2012.

[126] A. R. McIntosh and N. J. Lobaugh, ‘Partial least squares analysis of neuroimaging data: applications and advances’, *Neuroimage*, vol. 23, pp. S250–S263, 2004.

[127] H. Abdi, ‘Partial least squares regression and projection on latent structure regression (PLS Regression)’, *Wiley Interdiscip. Rev. Comput. Stat.*, vol. 2, no. 1, pp. 97–106, 2010.

[128] A. Krishnan, L. J. Williams, A. R. McIntosh, and H. Abdi, ‘Partial Least Squares (PLS) methods for neuroimaging: a tutorial and review’, *Neuroimage*, vol. 56, no. 2, pp. 455–475, 2011.

[129] P. Bai, H. Shen, X. Huang, and Y. Truong, ‘A supervised singular value decomposition for independent component analysis of fMRI’, *Stat. Sin.*, pp. 1233–1252, 2008.

[130] Y. Takane, ‘Relationships among various kinds of eigenvalue and singular value decompositions’, in *New Developments in Psychometrics: Proceedings of the*

International Meeting of the Psychometric Society IMPS2001. Osaka, Japan, July 15–19, 2001, Springer, 2003, pp. 45–56.

[131] T. Courville and B. Thompson, 'Use of structure coefficients in published multiple regression articles: β is not enough', *Educ. Psychol. Meas.*, vol. 61, no. 2, pp. 229–248, 2001.

[132] D. Zöller and V. Kebets, 'myPLS - Partial least squares analysis for medical image processing'.

[133] A. R. McIntosh, W. K. Chau, and A. B. Protzner, 'Spatiotemporal analysis of event-related fMRI data using partial least squares', *Neuroimage*, vol. 23, no. 2, pp. 764–775, 2004.

[134] B. Efron and R. Tibshirani, 'Bootstrap methods for standard errors, confidence intervals, and other measures of statistical accuracy', *Stat. Sci.*, pp. 54–75, 1986.

[135] F.-H. Lin, A. R. McIntosh, J. A. Agnew, G. F. Eden, T. A. Zeffiro, and J. W. Belliveau, 'Multivariate analysis of neuronal interactions in the generalized partial least squares framework: simulations and empirical studies', *NeuroImage*, vol. 20, no. 2, pp. 625–642, 2003.

[136] D. Zöller *et al.*, 'Large-Scale Brain Network Dynamics Provide a Measure of Psychosis and Anxiety in 22q11.2 Deletion Syndrome', *Biol. Psychiatry Cogn. Neurosci. Neuroimaging*, vol. 4, no. 10, pp. 881–892, Oct. 2019, doi: 10.1016/j.bpsc.2019.04.004.

[137] V. Kebets *et al.*, 'Somatosensory-Motor Dysconnectivity Spans Multiple Transdiagnostic Dimensions of Psychopathology', *Biol. Psychiatry*, vol. 86, no. 10, pp. 779–791, Nov. 2019, doi: 10.1016/j.biopsych.2019.06.013.

[138] D. Zöller, M. Schaer, E. Scariati, M. C. Padula, S. Eliez, and D. Van De Ville, 'Disentangling resting-state BOLD variability and PCC functional connectivity in 22q11.2 deletion syndrome', *NeuroImage*, vol. 149, pp. 85–97, Apr. 2017, doi: 10.1016/j.neuroimage.2017.01.064.

[139] D. Zöller *et al.*, 'Psychotic symptoms influence the development of anterior cingulate BOLD variability in 22q11.2 deletion syndrome', *Schizophr. Res.*, vol. 193, pp. 319–328, Mar. 2018, doi: 10.1016/j.schres.2017.08.003.

[140] M. S. Goyal *et al.*, 'Brain aerobic glycolysis and resilience in Alzheimer disease', *Proc. Natl. Acad. Sci.*, vol. 120, no. 7, p. e2212256120, 2023.

[141] S. N. Vaishnavi, A. G. Vlassenko, M. M. Rundle, A. Z. Snyder, M. A. Mintun, and M. E. Raichle, 'Regional aerobic glycolysis in the human brain', *Proc. Natl. Acad. Sci.*, vol. 107, no. 41, pp. 17757–17762, 2010.

[142] N. J. Tustison *et al.*, 'N4ITK: Improved N3 Bias Correction', *IEEE Trans. Med. Imaging*, vol. 29, no. 6, pp. 1310–1320, Jun. 2010, doi: 10.1109/TMI.2010.2046908.

[143] J. Ashburner and K. J. Friston, ‘Unified segmentation’, *NeuroImage*, vol. 26, no. 3, pp. 839–851, Jul. 2005, doi: 10.1016/j.neuroimage.2005.02.018.

[144] B. B. Avants, N. J. Tustison, G. Song, P. A. Cook, A. Klein, and J. C. Gee, ‘A reproducible evaluation of ANTs similarity metric performance in brain image registration’, *NeuroImage*, vol. 54, no. 3, pp. 2033–2044, Feb. 2011, doi: 10.1016/j.neuroimage.2010.09.025.

[145] ‘ITK-SNAP Home’. Accessed: Apr. 07, 2024. [Online]. Available: http://www.itksnap.org/pmwiki/pmwiki.php

[146] M. F. Glasser *et al.*, ‘The minimal preprocessing pipelines for the Human Connectome Project’, *NeuroImage*, vol. 80, pp. 105–124, Oct. 2013, doi: 10.1016/j.neuroimage.2013.04.127.

[147] S. M. Smith *et al.*, ‘Advances in functional and structural MR image analysis and implementation as FSL’, *NeuroImage*, vol. 23, pp. S208–S219, Jan. 2004, doi: 10.1016/j.neuroimage.2004.07.051.

[148] J. L. R. Andersson, S. Skare, and J. Ashburner, ‘How to correct susceptibility distortions in spin-echo echo-planar images: application to diffusion tensor imaging’, *NeuroImage*, vol. 20, no. 2, pp. 870–888, Oct. 2003, doi: 10.1016/S1053-8119(03)00336-7.

[149] M. Jenkinson, C. F. Beckmann, T. E. J. Behrens, M. W. Woolrich, and S. M. Smith, ‘FSL’, *NeuroImage*, vol. 62, no. 2, pp. 782–790, Aug. 2012, doi: 10.1016/j.neuroimage.2011.09.015.

[150] Y. Behzadi, K. Restom, J. Liau, and T. T. Liu, ‘A component based noise correction method (CompCor) for BOLD and perfusion based fMRI’, *NeuroImage*, vol. 37, no. 1, pp. 90–101, Aug. 2007, doi: 10.1016/j.neuroimage.2007.04.042.

[151] D. N. Greve and B. Fischl, ‘Accurate and robust brain image alignment using boundary-based registration’, *NeuroImage*, vol. 48, no. 1, pp. 63–72, Oct. 2009, doi: 10.1016/j.neuroimage.2009.06.060.

[152] R. H. Pruim, M. Mennes, D. van Rooij, A. Llera, J. K. Buitelaar, and C. F. Beckmann, ‘ICA-AROMA: A robust ICA-based strategy for removing motion artifacts from fMRI data’, *Neuroimage*, vol. 112, pp. 267–277, 2015.

[153] E. Silvestri *et al.*, ‘Widespread cortical functional disconnection in gliomas: an individual network mapping approach’, *Brain Commun.*, vol. 4, no. 2, p. fcac082, Mar. 2022, doi: 10.1093/braincomms/fcac082.

[154] G. Vallini, E. Silvestri, A. Panciera, M. Aiello, and A. Bertoldo, ‘Assessment of the effects of parcellation and frequency band on the definition of functional hubs in rsfMRI’, 2023.

[155] X. Yan *et al.*, ‘Homotopic local-global parcellation of the human cerebral cortex from resting-state functional connectivity’, *NeuroImage*, vol. 273, p. 120010, Jun. 2023, doi: 10.1016/j.neuroimage.2023.120010.

[156] B. T. Yeo *et al.*, 'The organization of the human cerebral cortex estimated by intrinsic functional connectivity', *J. Neurophysiol.*, 2011.

[157] A. G. S. Daniel *et al.*, 'Homotopic functional connectivity disruptions in glioma patients are associated with tumor malignancy and overall survival', *Neuro-Oncol. Adv.*, vol. 3, no. 1, p. vdab176, Jan. 2021, doi: 10.1093/noajnl/vdab176.

[158] K.-H. Nenning *et al.*, 'Distributed changes of the functional connectome in patients with glioblastoma', *Sci. Rep.*, vol. 10, no. 1, p. 18312, Oct. 2020, doi: 10.1038/s41598-020-74726-1.

[159] J. Derks *et al.*, 'Connectomic profile and clinical phenotype in newly diagnosed glioma patients', *NeuroImage Clin.*, vol. 14, pp. 87–96, 2017.

[160] S. Lehericy *et al.*, 'Functional MR evaluation of temporal and frontal language dominance compared with the Wada test', *Neurology*, vol. 54, no. 8, pp. 1625–1633, 2000.

[161] V. Hesselmann *et al.*, 'Intraoperative functional MRI as a new approach to monitor deep brain stimulation in Parkinson's disease', *Eur. Radiol.*, vol. 14, no. 4, pp. 686–690, Apr. 2004, doi: 10.1007/s00330-003-2051-0.

[162] M. Wengenroth, M. Blatow, J. Guenther, M. Akbar, V. M. Tronnier, and C. Stippich, 'Diagnostic benefits of presurgical fMRI in patients with brain tumours in the primary sensorimotor cortex', *Eur. Radiol.*, vol. 21, pp. 1517–1525, 2011.

[163] M. Mossa-Basha, J. Chen, and D. Gandhi, 'Imaging of cerebral arteriovenous malformations and dural arteriovenous fistulas', *Neurosurg. Clin.*, vol. 23, no. 1, pp. 27–42, 2012.

[164] M. K. Montgomery *et al.*, 'Glioma-Induced Alterations in Neuronal Activity and Neurovascular Coupling during Disease Progression', *Cell Rep.*, vol. 31, no. 2, p. 107500, Apr. 2020, doi: 10.1016/j.celrep.2020.03.064.

[165] J. D. Power, A. Mitra, T. O. Laumann, A. Z. Snyder, B. L. Schlaggar, and S. E. Petersen, 'Methods to detect, characterize, and remove motion artifact in resting state fMRI', *Neuroimage*, vol. 84, pp. 320–341, 2014.

[166] M. Jenkinson, P. Bannister, M. Brady, and S. Smith, 'Improved optimization for the robust and accurate linear registration and motion correction of brain images', *Neuroimage*, vol. 17, no. 2, pp. 825–841, 2002.

[167] C. Leiva-Salinas, D. Schiff, L. Flors, J. T. Patrie, and P. K. Rehm, 'FDG PET/MR imaging coregistration helps predict survival in patients with glioblastoma and radiologic progression after standard of care treatment', *Radiology*, vol. 283, no. 2, pp. 508–514, 2017.

[168] K. R. Byrnes *et al.*, 'FDG-PET imaging in mild traumatic brain injury: a critical review', *Front. Neuroenergetics*, vol. 5, 2014, doi: 10.3389/fnene.2013.00013.

[169] B. C. M. Van Wijk, C. J. Stam, and A. Daffertshofer, 'Comparing Brain Networks of Different Size and Connectivity Density Using Graph Theory', *PLoS ONE*, vol. 5, no. 10, p. e13701, Oct. 2010, doi: 10.1371/journal.pone.0013701.

[170] M. P. Van Den Heuvel, S. C. De Lange, A. Zalesky, C. Seguin, B. T. T. Yeo, and R. Schmidt, 'Proportional thresholding in resting-state fMRI functional connectivity networks and consequences for patient-control connectome studies: Issues and recommendations', *NeuroImage*, vol. 152, pp. 437–449, May 2017, doi: 10.1016/j.neuroimage.2017.02.005.

[171] F. H. Duffy, G. B. Mcanulty, and M. S. Albert, 'Effects of age upon interhemispheric EEG coherence in normal adults', *Neurobiol. Aging*, vol. 17, no. 4, pp. 587–599, 1996.

[172] X.-N. Zuo *et al.*, 'Growing Together and Growing Apart: Regional and Sex Differences in the Lifespan Developmental Trajectories of Functional Homotopy', *J. Neurosci.*, vol. 30, no. 45, pp. 15034–15043, Nov. 2010, doi: 10.1523/JNEUROSCI.2612-10.2010.

[173] A. Griffa, E. Amico, R. Liégeois, D. Van De Ville, and M. G. Preti, 'Brain structure-function coupling provides signatures for task decoding and individual fingerprinting', *NeuroImage*, vol. 250, p. 118970, Apr. 2022, doi: 10.1016/j.neuroimage.2022.118970.

[174] S. Loukas *et al.*, 'Musical memories in newborns: A resting-state functional connectivity study', *Hum. Brain Mapp.*, vol. 43, no. 2, pp. 647–664, Feb. 2022, doi: 10.1002/hbm.25677.

[175] A. Mihalik *et al.*, 'Canonical correlation analysis and partial least squares for identifying brain–behavior associations: A tutorial and a comparative study', *Biol. Psychiatry Cogn. Neurosci. Neuroimaging*, vol. 7, no. 11, pp. 1055–1067, 2022.

[176] D. Tomasi and N. D. Volkow, 'Association between Functional Connectivity Hubs and Brain Networks', *Cereb. Cortex*, vol. 21, no. 9, pp. 2003–2013, Sep. 2011, doi: 10.1093/cercor/bhq268.

[177] A. Hahn *et al.*, 'Reconfiguration of functional brain networks and metabolic cost converge during task performance', *eLife*, vol. 9, p. e52443, Apr. 2020, doi: 10.7554/eLife.52443.

[178] K. Lv *et al.*, 'Neuroplasticity of Glioma Patients: Brain Structure and Topological Network', *Front. Neurol.*, vol. 13, p. 871613, May 2022, doi: 10.3389/fneur.2022.871613.

[179] M. E. Raichle, 'Two views of brain function', *Trends Cogn. Sci.*, vol. 14, no. 4, pp. 180–190, 2010.

[180] D. Attwell and C. Iadecola, 'The neural basis of functional brain imaging signals', *Trends Neurosci.*, vol. 25, no. 12, pp. 621–625, 2002.

[181] C. Iadecola, 'Neurovascular regulation in the normal brain and in Alzheimer's disease', *Nat. Rev. Neurosci.*, vol. 5, no. 5, pp. 347–360, 2004.

[182] A. W. Toga and P. M. Thompson, 'Mapping brain asymmetry', *Nat. Rev. Neurosci.*, vol. 4, no. 1, pp. 37–48, Jan. 2003, doi: 10.1038/nrn1009.

[183] *The Two Halves of the Brain: Information Processing in the Cerebral Hemispheres*. The MIT Press, 2010. doi: 10.7551/mitpress/9780262014137.001.0001.

[184] D. S. Margulies *et al.*, 'Resting developments: a review of fMRI post-processing methodologies for spontaneous brain activity', *Magn. Reson. Mater. Phys. Biol. Med.*, vol. 23, pp. 289–307, 2010.

[185] P. T. Fox, M. E. Raichle, M. A. Mintun, and C. Dence, 'Nonoxidative glucose consumption during focal physiologic neural activity', *Science*, vol. 241, no. 4864, pp. 462–464, 1988.

[186] M. Amend, T. M. Ionescu, X. Di, B. J. Pichler, B. B. Biswal, and H. F. Wehrl, 'Functional resting-state brain connectivity is accompanied by dynamic correlations of application-dependent [^{18}F]FDG PET-tracer fluctuations', *NeuroImage*, vol. 196, pp. 161–172, Aug. 2019, doi: 10.1016/j.neuroimage.2019.04.034.

[187] S. F. Storti, I. Boscolo Galazzo, S. Montemezzi, G. Menegaz, and F. B. Pizzini, 'Dual-echo ASL contributes to decrypting the link between functional connectivity and cerebral blow flow', *Hum. Brain Mapp.*, vol. 38, no. 12, pp. 5831–5844, 2017, doi: 10.1002/hbm.23804.

[188] X. Liang, Q. Zou, Y. He, and Y. Yang, 'Coupling of functional connectivity and regional cerebral blood flow reveals a physiological basis for network hubs of the human brain', *Proc. Natl. Acad. Sci.*, vol. 110, no. 5, pp. 1929–1934, Jan. 2013, doi: 10.1073/pnas.1214900110.

[189] M. E. Raichle, 'The brain's default mode network', *Annu. Rev. Neurosci.*, vol. 38, pp. 433–447, 2015.

[190] L. Sokoloff, 'Energetics of functional activation in neural tissues', *Neurochem. Res.*, vol. 24, pp. 321–329, 1999.

[191] D. Attwell and S. B. Laughlin, 'An Energy Budget for Signaling in the Grey Matter of the Brain', *J. Cereb. Blood Flow Metab.*, vol. 21, no. 10, pp. 1133–1145, Oct. 2001, doi: 10.1097/00004647-200110000-00001.

[192] P. Lennie, 'The Cost of Cortical Computation', *Curr. Biol.*, vol. 13, no. 6, pp. 493–497, Mar. 2003, doi: 10.1016/S0960-9822(03)00135-0.

[193] S. Palva and J. M. Palva, 'Roles of Brain Criticality and Multiscale Oscillations in Temporal Predictions for Sensorimotor Processing', *Trends Neurosci.*, vol. 41, no. 10, pp. 729–743, Oct. 2018, doi: 10.1016/j.tins.2018.08.008.

[194] F. Siebenhühner *et al.*, 'Genuine cross-frequency coupling networks in human resting-state electrophysiological recordings', *PLOS Biol.*, vol. 18, no. 5, p. e3000685, May 2020, doi: 10.1371/journal.pbio.3000685.

[195] D. Mantini, M. G. Perrucci, C. Del Gratta, G. L. Romani, and M. Corbetta, 'Electrophysiological signatures of resting state networks in the human brain', *Proc. Natl. Acad. Sci.*, vol. 104, no. 32, pp. 13170–13175, Aug. 2007, doi: 10.1073/pnas.0700668104.

[196] F. De Pasquale *et al.*, 'Temporal dynamics of spontaneous MEG activity in brain networks', *Proc. Natl. Acad. Sci.*, vol. 107, no. 13, pp. 6040–6045, Mar. 2010, doi: 10.1073/pnas.0913863107.

[197] J. L. Brooks and S. E. Palmer, 'Cue Competition Affects Temporal Dynamics of Edge-assignment in Human Visual Cortex', *J. Cogn. Neurosci.*, vol. 23, no. 3, pp. 631–644, Mar. 2011, doi: 10.1162/jocn.2010.21433.

[198] L. K. Shiyam Sundar *et al.*, 'Fully Integrated PET/MR Imaging for the Assessment of the Relationship Between Functional Connectivity and Glucose Metabolic Rate', *Front. Neurosci.*, vol. 14, p. 252, Mar. 2020, doi: 10.3389/fnins.2020.00252.

[199] T. Volpi, E. Silvestri, M. Aiello, M. Corbetta, and A. Bertoldo, 'The complexity of the relationship between spontaneous brain activity and glucose metabolism'. Aug. 04, 2021. doi: 10.21203/rs.3.rs-728300/v1.

[200] T. Volpi *et al.*, 'The brain's "dark energy" puzzle: How strongly is glucose metabolism linked to resting-state brain activity?', *J. Cereb. Blood Flow Metab.*, p. 0271678X241237974, Mar. 2024, doi: 10.1177/0271678X241237974.

[201] W. Li *et al.*, 'Topographic metabolism-function relationships in Alzheimer's disease: A simultaneous PET / MRI study', *Hum. Brain Mapp.*, vol. 45, no. 2, p. e26604, Feb. 2024, doi: 10.1002/hbm.26604.

[202] S. Deng *et al.*, 'Hemodynamic and metabolic correspondence of resting-state voxel-based physiological metrics in healthy adults', *Neuroimage*, vol. 250, p. 118923, 2022.

[203] V. Riedl *et al.*, 'Local Activity Determines Functional Connectivity in the Resting Human Brain: A Simultaneous FDG-PET/fMRI Study', *J. Neurosci.*, vol. 34, no. 18, pp. 6260–6266, Apr. 2014, doi: 10.1523/JNEUROSCI.0492-14.2014.

[204] R. Marchitelli *et al.*, 'Simultaneous resting-state FDG-PET/fMRI in Alzheimer Disease: Relationship between glucose metabolism and intrinsic activity', *NeuroImage*, vol. 176, pp. 246–258, Aug. 2018, doi: 10.1016/j.neuroimage.2018.04.048.

[205] J. E. LeDoux, 'Emotion Circuits in the Brain', *Annu. Rev. Neurosci.*, vol. 23, no. 1, pp. 155–184, Mar. 2000, doi: 10.1146/annurev.neuro.23.1.155.

[206] E. A. Phelps, 'Emotion and Cognition: Insights from Studies of the Human Amygdala', *Annu. Rev. Psychol.*, vol. 57, no. 1, pp. 27–53, Jan. 2006, doi: 10.1146/annurev.psych.56.091103.070234.

[207] S. L. Bressler and V. Menon, 'Large-scale brain networks in cognition: emerging methods and principles', *Trends Cogn. Sci.*, vol. 14, no. 6, pp. 277–290, Jun. 2010, doi: 10.1016/j.tics.2010.04.004.

[208] M. Corbetta and G. L. Shulman, ‘Control of goal-directed and stimulus-driven attention in the brain’, *Nat. Rev. Neurosci.*, vol. 3, no. 3, pp. 201–215, Mar. 2002, doi: 10.1038/nrn755.

[209] S. K. A. L. G. Ungerleider, ‘Mechanisms of Visual Attention in the Human Cortex’, *Annu. Rev. Neurosci.*, vol. 23, no. 1, pp. 315–341, Mar. 2000, doi: 10.1146/annurev.neuro.23.1.315.

[210] A. Gazzaley and A. C. Nobre, ‘Top-down modulation: bridging selective attention and working memory’, *Trends Cogn. Sci.*, vol. 16, no. 2, pp. 129–135, Feb. 2012, doi: 10.1016/j.tics.2011.11.014.

[211] D. T. Stuss and M. P. Alexander, ‘Is there a dysexecutive syndrome?’, *Philos. Trans. R. Soc. B Biol. Sci.*, vol. 362, no. 1481, pp. 901–915, 2007.

[212] B. A. Wandell and S. M. Smirnakis, ‘Plasticity and stability of visual field maps in adult primary visual cortex’, *Nat. Rev. Neurosci.*, vol. 10, no. 12, pp. 873–884, 2009.

[213] J. D. Schmahmann and D. Caplan, ‘Cognition, emotion and the cerebellum’, *Brain*, vol. 129, no. 2, pp. 290–292, 2006.

[214] A. D. Craig, ‘How do you feel—now? The anterior insula and human awareness’, *Nat. Rev. Neurosci.*, vol. 10, no. 1, pp. 59–70, 2009.

[215] R. Mancusi and M. Monje, ‘The neuroscience of cancer’, *Nature*, vol. 618, no. 7965, pp. 467–479, Jun. 2023, doi: 10.1038/s41586-023-05968-y.

[216] I. E. Orukari *et al.*, ‘Altered hemodynamics contribute to local but not remote functional connectivity disruption due to glioma growth’, *J. Cereb. Blood Flow Metab.*, vol. 40, no. 1, pp. 100–115, Jan. 2020, doi: 10.1177/0271678X18803948.

[217] L. Pasquini, M. Jenabi, O. Yildirim, P. Silveira, K. K. Peck, and A. I. Holodny, ‘Brain Functional Connectivity in Low- and High-Grade Gliomas: Differences in Network Dynamics Associated with Tumor Grade and Location’, *Cancers*, vol. 14, no. 14, p. 3327, Jul. 2022, doi: 10.3390/cancers14143327.

[218] O. Warburg, ‘On the Origin of Cancer Cells’, *Science*, vol. 123, no. 3191, pp. 309–314, Feb. 1956, doi: 10.1126/science.123.3191.309.

[219] M. G. Vander Heiden, L. C. Cantley, and C. B. Thompson, ‘Understanding the Warburg Effect: The Metabolic Requirements of Cell Proliferation’, *Science*, vol. 324, no. 5930, pp. 1029–1033, May 2009, doi: 10.1126/science.1160809.

[220] F. Hirschhaeuser, U. G. A. Sattler, and W. Mueller-Klieser, ‘Lactate: A Metabolic Key Player in Cancer’, *Cancer Res.*, vol. 71, no. 22, pp. 6921–6925, Nov. 2011, doi: 10.1158/0008-5472.CAN-11-1457.

[221] P. S. Ward and C. B. Thompson, ‘Metabolic Reprogramming: A Cancer Hallmark Even Warburg Did Not Anticipate’, *Cancer Cell*, vol. 21, no. 3, pp. 297–308, Mar. 2012, doi: 10.1016/j.ccr.2012.02.014.

[222] M. L. M. Zimmermann *et al.*, ‘The relationship between pathological brain activity and functional network connectivity in glioma patients’, *J. Neurooncol.*, vol. 166, no. 3, pp. 523–533, Feb. 2024, doi: 10.1007/s11060-024-04577-7.

[223] A. G. Vlassenko *et al.*, ‘Aerobic Glycolysis as a Marker of Tumor Aggressiveness: Preliminary Data in High Grade Human Brain Tumors’, *Dis. Markers*, vol. 2015, pp. 1–11, 2015, doi: 10.1155/2015/874904.